technische universität
dortmund

Arbeit zur Erlangung des akademischen Grades
Dr. rer. nat.

Towards Real Time Neutron Flux Measurement in the Thermal Column of a Research Reactor

Alina Johanna Landmann

geboren in Frankfurt am Main

2025

Experimentelle Physik - AG Kröninger
Fakultät Physik
Technische Universität Dortmund

Erstgutachter: Prof. Dr. K. Kröninger
Zweitgutachter: Prof. Dr. A. Lühr
Abgabedatum: 14 March 2025

Abstract

Active neutron flux measurements are crucial in many different applications, such as non-destructive material testing, soilwater content determination or in radiation therapy. Another field of application is active neutron flux monitoring in (research) reactors during experiments. Many commercially available neutron detectors use ^{3}He as a neutron converter to detect indirectly ionizing neutrons, as it exhibits a high neutron interaction cross-section. However, the increasing scarcity and cost of ^{3}He have motivated the search for alternative neutron detection technologies. In this thesis, a novel silicon-based detector prototype with interchangeable neutron converter carrier plates is developed, characterized, and tested in laboratory conditions with a low flux neutron source at TU Dortmund University. Finally, an improved prototype detector is tested in the thermal column of a *Training Research Isotopes General Atomics* (TRIGA) reactor. A pulse shape discrimination algorithm in the signal processing is applied to distinguish between neutron and background radiation. The results obtained demonstrate the potential of silicon-based neutron detectors for reactor monitoring.

Aktive Neutronenflussmessungen spielen in unterschiedlichen Anwendungen eine wichtige Rolle, zum Beispiel bei der zerstörungsfreien Materialprüfung, der Bestimmung des Wassergehalts in Erdproben oder in der radiologischen Überwachung in der Strahlentherapie. Ein weiteres Anwendungsgebiet ist die aktive Neutronenflussüberwachung in (Forschungs-)Reaktoren bei Experimenten. Viele kommerziell erhältliche Neutronendetektoren verwenden ^{3}He aufgrund seines hohen Neutronenwechselwirkungsquerschnitts, als Konverter zum Nachweis der indirekt ionisierenden Neutronen. Die zunehmende Verknappung und die steigenden Kosten von ^{3}He motivieren jedoch die Suche nach alternativen Neutronennachweistechnologien. In dieser Arbeit wird ein neuartiger siliziumbasierter Detektorprototyp mit austauschbaren Neutronenkonverter-Trägerplatten entwickelt, charakterisiert und unter Laborbedingungen in einer Neutronenquelle mit niedrigen Flussraten an der TU Dortmund getestet. Abschließend wird ein verbesserter Detektorprototyp in der thermischen Säule eines TRIGA-Reaktors (Training Research Isotopes General Atomics) getestet. Zur Unterscheidung zwischen Neutronen- und Hintergrundstrahlung wird ein Algorithmus zur Pulsformanalyse in der Signalverarbeitung eingesetzt. Die erzielten Ergebnisse zeigen das Potenzial von siliziumbasierten Neutronendetektoren für die Reaktorüberwachung.

Contents

1 Introduction

The active measurement of neutron flux is of significant interest across various applications, including non-destructive testing of materials and determination of water content [1] through the measurement of scattered neutrons, as well as neutron flux assessment in research reactors during experiments and its application in radiation therapy [2].

Since neutrons do not ionize atoms directly, their detection relies on indirect methods that identify secondary radiation produced by neutron interactions. Consequently, neutron detection necessitates the use of neutron converters to generate secondary radiation upon interaction with neutrons. A commonly utilized converter in neutron detection is ^{3}He due to its large interaction cross section for thermal neutrons. However, in recent years, this material has become increasingly scarce [3, 4], leading to rising costs that may render neutron detection a high-cost endeavor. Additionally, gaseous detectors based on ^{3}He are challenging to operate, particularly in spatially confined environments.

Alternative neutron detectors, based on semiconductor technology, have been explored over the past few decades [5–8]. Semiconductors have demonstrated promising results; silicon-based neutron detectors are employed in electronic personal dosimeters [9, 10]. One area that has received less attention regarding silicon-based neutron detectors is nuclear (research) reactors. This thesis investigates the thermal neutron flux within the thermal column of a Training Research Isotopes General Atomics (TRIGA) reactor. To achieve this objective, a novel silicon detector prototype has been developed, integrating a silicon detector with a boron carbide neutron converter that is highly enriched with ^{10}B due to its superior neutron capture cross section compared to natural boron carbide.

Neutron fields typically consist of mixed radiation environments containing various background radiation. It is physically unfeasible to completely shield the detector from this radiation without adversely affecting the efficiency of neutron detection. In this work, a flexible detector system based on a silicon diode featuring interchangeable neutron converter plates is developed. An initial prototype was characterized under laboratory conditions and subsequently improved for testing within the thermal column of a research reactor.

The thesis outline covers the basic physical principles of neutron production and interaction in chapter 2. The following chapters 3 and 4 give an overview of neutron detection and dosimetry systems and deliver the theoretical background for neutron detection with silicon detectors. The detector characterization and description of the used amplifiers can be found in chapter 5. The test of the first prototype developed in this work at the neutron source at the TU Dortmund University is presented in chapter 6. Finally, chapter 7 discusses tests conducted with the prototype detector equipped with a converter at a Training Research Isotopes General Atomics (TRIGA) reactor. Results indicate enhanced noise reduction attributable to both design modifications in the readout board and implementation of a pulse shape discrimination algorithm designed to distinguish between neutron signals and background radiation.

2 Neutrons - Creation and Interaction

When discussing neutron detection, it is important to understand fundamental neutron production and interaction processes. Free neutrons are unstable particles and decay within a mean lifetime of $(878.6 \pm 0.6)\,\mathrm{s}$ [11]. The initial kinetic energy of a free neutron depends on the neutron production process. In this chapter, a typical neutron fluence energy spectrum taken at a proton therapy centre is presented, and it is utilized to explain the fundamental processes underlying neutron production processes and subsequent interaction processes.

2.1 Interaction Probabilities - Cross Sections

The probability of a particle undergoing a specific reaction process with a given isotope strongly depends on the particle's energy and the isotope's nuclear composition. This interaction probability is expressed in terms of the cross section σ. The unit of the cross section is "*barn*(b)" which is defined as $1\,\mathrm{b} = 10^{-24}\,\mathrm{cm}^2$. This indicates that a larger cross section corresponds to an increased effective area for particle interactions, resulting in a higher interaction probability. For example, in neutron capture, the cross section increases as the neutron's kinetic energy decreases, since slower-moving particles obtain a longer interaction time with the nucleus. Each reaction type is characterized by its unique energy-dependent cross section. The *total cross section* describes the sum of all individual cross sections for a given process:

$$\sigma_{\text{total}} = \sigma_{\text{elastic}} + \sigma_{\text{inelastic}} + \sigma_{\text{capture}} + \sigma_{\text{fission}} + \ldots$$

2.2 Neutron Production and Reaction Processes

Neutron production is triggered by a variety of proton-nuclear reactions. The ICRU [12] classifies three types of proton-nuclear interactions: *elastic*, *nonelastic* and *inelastic*. *Elastic* interaction processes describe proton scattering with a low kinetic energy transfer to the nucleus with a total kinetic energy conservation, leaving the internal state of the nucleus stable. Nonelastic interaction processes describe processes that are not elastic, such as target nucleus break-ups or the excitation of the target nucleus. Characteristically, the kinetic energy is not conserved in these reactions. The third group with the *inelastic* proton nuclear reactions describes a specific type of *nonelastic* interactions without kinetic energy conservation, but where the target nucleus is in the same state as before the interaction [13]. The kinetic energy loss is often accompanied by photon emission. While the exact probability and frequency of these reactions depend on both energy and material properties, understanding the primary mechanisms of neutron production processes is essential for characterizing neutron behavior in different environments.

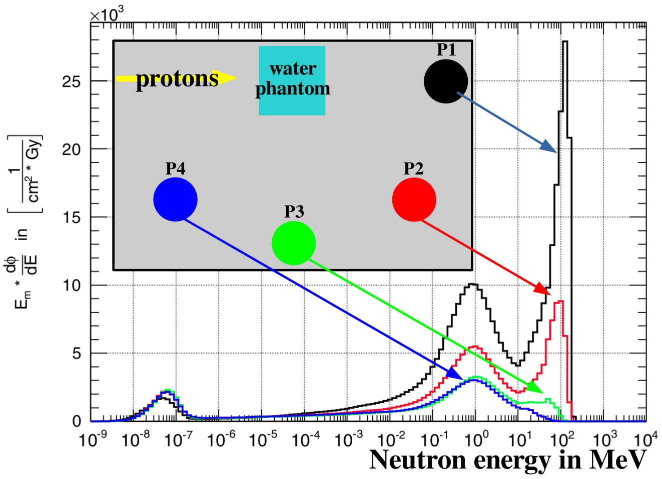

Figure 2.1: Neutron energy spectrum with measurement spots placed around a water phantom that is irradiated by protons. Spectrum plot with position information created after [14].

Figure 2.1 shows neutron energy spectra obtained at a proton therapy centre by [14]. The research group irradiated a water phantom with a proton field shaped by double scattering and measured the neutron fluences at different positions around the phantom, which are also displayed in figure 2.1.

The highest peak in the spectrum on display shows entries at maximum proton energies, in this case, 200 MeV. The origin of neutrons with this energy is most likely explained by protons undergoing spallation reactions with the beam-guiding materials. Once these so-called high-energy neutrons escape the nuclei, they start interacting with the surrounding atoms mainly through elastic and inelastic scattering. However, since their energies exceed binding energies in atomic nuclei so the high-energy neutrons can transfer enough energy to induce neutron evaporation.

This explains the second peak from the right in the histogram. It is consequently positioned around a few MeV up to 8 MeV.
The neutrons with these energies are called *fast neutrons*. Neutrons with energies below the nuclear binding energy primarily interact with their surroundings through elastic and inelastic scattering.
With each collision, they lose energy and gradually slow down. Once their energy falls below the thermal energy of the surrounding atoms, they begin to gain thermal equilibrium upon collision, forming the *thermal peak* (*thermalneutrons*), which appears on the far left side of the energy spectrum on display. As the thermal energy of the surrounding atoms depends on the room temperature, its position shifts towards lower energies with lower temperature. The neutrons with energies between 1 MeV and ≈ 25 meV are called *intermediate* neutrons.
The neutron interaction processes are described in more detail in the following sections. Understanding the neutron interaction processes the model of the compound nucleus introduced by Niels Bohr in 1936 [15] can help. This model describes nuclear reactions in two stages: The formation of an unstable compound nucleus with its subsequent decay. The different physical processes occurring inside the compound nucleus due to neutron interaction are explained in the following sections.
Penetrating neutrons have an influence on the sometimes fragile stability of atomic nuclei by changing the binding energy inside the target nucleus. The binding energy of a nucleus can be described by the *Bethe Weizsäcker* formula 2.1 for most of the heavier nuclei:

$$B(\mathrm{A},\mathrm{Z}) = a_v\mathrm{A} - a_s\mathrm{A}^{2/3} - a_c\frac{\mathrm{Z}(\mathrm{Z}-1)}{\mathrm{A}^{1/3}} - a_a\frac{(\mathrm{A}-2\mathrm{Z})^2}{\mathrm{A}} + \delta(\mathrm{A},\mathrm{Z}) \tag{2.1}$$

$$\delta(\mathrm{A},\mathrm{Z}) = \begin{cases} +a_p A^{-3/4}, & \text{for even Z, even N (even-even nucleus)} \\ 0, & \text{for odd Z, odd N (odd-odd nucleus)} \\ -a_p A^{-3/4}, & \text{for even Z, odd N (odd-even nucleus)} \end{cases}$$

It accounts for various characteristic features impacting binding energies $B(\mathrm{A},\mathrm{Z})$, where A represents mass number while Z denotes atomic number:

- a_v → Volume term: Accounts for strong nuclear force binding nucleons together. Each nucleon interacts with a constant number of neighbouring nucleons. Energy contribution $\propto \mathrm{A}$
- a_s → Surface term: Correction for surface nucleons that experience fewer attractive nuclear forces than in the bulk. Binding energy reduction $\propto \mathrm{A}^{2/3}$
- a_c → Coulomb term: Represents electrostatic repulsion of protons inside the nucleus. Binding energy reduction $\propto \frac{\mathrm{Z}(\mathrm{Z}-1)}{\mathrm{A}^{1/3}}$

- $a_a \rightarrow$ Asymmetry term: Accounts for the energy reduction due to an unequal number of protons and neutrons due to the Pauli exclusion principle's effect on nuclear stability.
- $a_p \rightarrow$ Pairing term: Additional binding energy from nucleon pairing correction. Even-even nuclei are more tightly bound than odd-odd or odd-even nuclei as a result of spin pairing effects.

The dependence of binding energies per nucleon as function A is depicted in figure 2.2. It shows that binding energies reach maxima for ^{56}Fe, saturating at $\approx 8\,\mathrm{MeV}$.

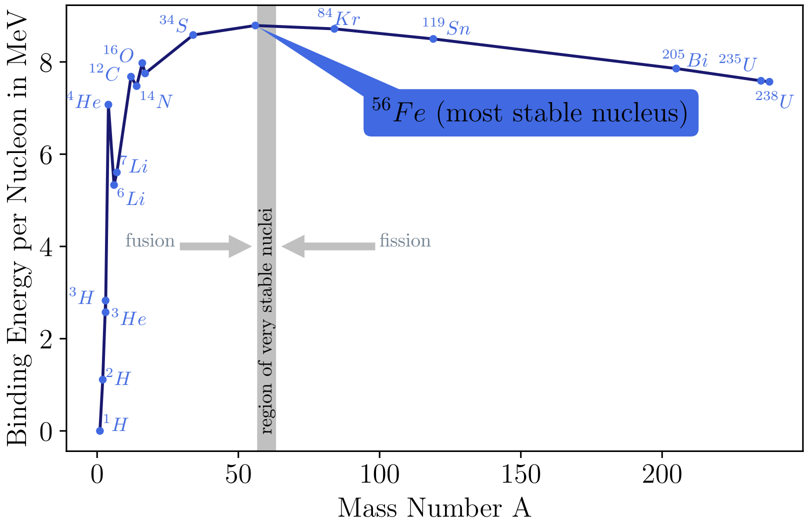

Figure 2.2: Binding energy per nucleon as a function of the mass number A.

2.2.1 Spallation

High energetic neutrons can cause spallation themselves. If neutrons at energies above 100 MeV collide non-elastically with a single nucleon when passing the Coulomb barrier of an atomic nucleus, they can transfer their kinetic energy to individual nucleons, which then excite nearby nucleons in a chain reaction known as a nuclear cascade. Characteristic of spallation processes is the fact that the kinetic energy transfer leads to a fragmentation of the initial atomic nucleus with spallation product emission into the direction of the initial, in the described case, proton beam. The energy of the emitted nucleons can reach up to the initial proton energy. In the spectrum on display in figure 2.1 this is an energy of 200 MeV. The remaining nucleus is typically in a highly excited state that causes the second stage of

spallation: neutron evaporation. In contrast to the neutrons produced in the first stage of spallation, these neutrons have significantly lower energies in the range of the binding energy within a nucleus ranging from a few MeV up to 10 MeV in the maximum. These evaporation neutrons are emitted isotropically from the nucleus. If the energy inside the compound nucleus is smaller than the binding energy of the nucleus, it de-excites by photon emission ([*16*]).
The schematic drawing in figure 2.3 shows the spallation process induced by high-energy neutrons.

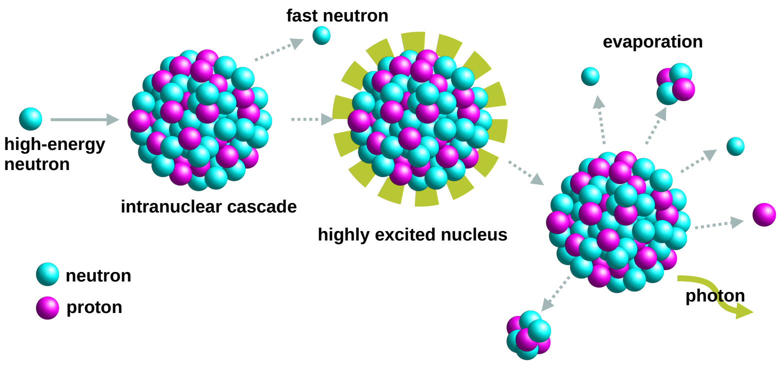

Figure 2.3: Schematic drawing of a spallation process. The highly excited compound nucleus de-excites by evaporation of nucleus fragments, heavy particles, and photons.

2.2.2 Inelastic and Elastic Scattering

Elastic and inelastic scattering are the main processes by which high-energy neutrons transfer energy to their surrounding atoms. The compound nucleus model helps understanding the inelastic scattering process very well. It describes the brief capture of a neutron forming a compound nucleus from which a single neutron is released almost instantaneously. A schematic drawing of that process can be found in figure 2.4. The neutron deposits parts of its energy inside the nucleus, leaving it in an excited state which de-excites by photon emission. De-excitation photons are, therefore, always present in neutron fields, being one part of the so-called mixed fields that characteristically are present in neutron fields.
Inelastic scattering is the main process due to which high energetic neutrons lose energy [*13*]. For neutron energies above 10 MeV inelastic scattering is the dominant process responsible for energy loss because for inelastic scattering to happen, the energy of the incident neutron has to exceed the energy of the lowest excited state

of the collision partner. For lead, which is commonly used for high-energy neutron energy moderation, this value is 0.57 MeV [13].

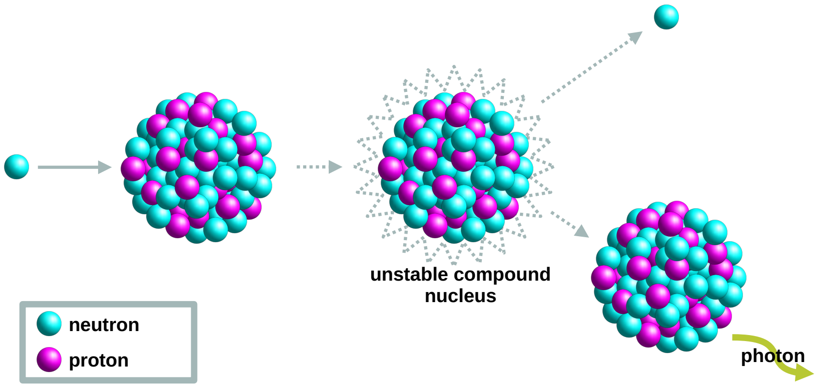

Figure 2.4: Schematic drawing of the inelastic scattering process, with the compound nucleus, that de-excited by gamma and neutron emmission.

The other scattering process is elastic scattering, in which the kinetic energies of the neutron and target are conserved. Figure 2.5 shows a schematic drawing of the elastic scattering process.

Neutrons with energies above the binding energy of the target nucleus collide with single nucleons, which can subsequently be released if the energy transferred in the collision exceeds the binding energy. For smaller energy transfers, the kinetic energy transferred from the neutron to the nucleus changes the direction of the collision partners. The neutron's maximum kinetic energy loss occurs in collisions with hydrogen because its nucleus is formed by a quasi-free proton. Since protons and neutrons have nearly identical masses ([11, 17]), a neutron can lose up to half of its kinetic energy due to elastic scattering. This explains why hydrogenous materials are frequently used for neutron moderation.

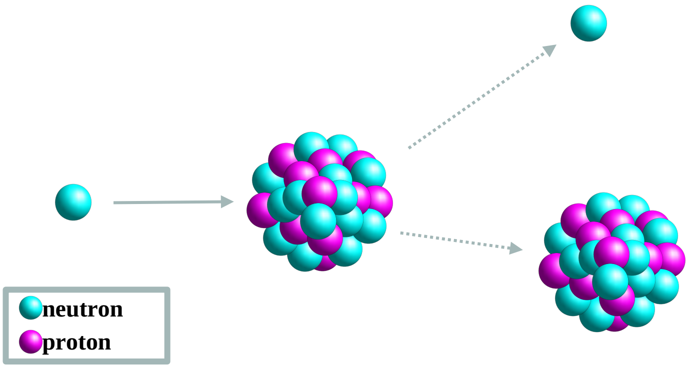

Figure 2.5: Schematic sketch of the elastic scattering process.

2.2.3 Capture

Similar to inelastic scattering, neutron capture describes a process in which a neutron is absorbed by a target nucleus. In this process, however, the compound nucleus breaks up by releasing other nucleus fragments, such as α-particles . An example of this is the ^{10}B neutron capture reaction depicted in figure 2.6. After α-emission, the remaining nucleus loses two neutrons and two protons. Additionally, in six percent of the cases, the nucleus remains in an excited state that de-excites by photon emission.

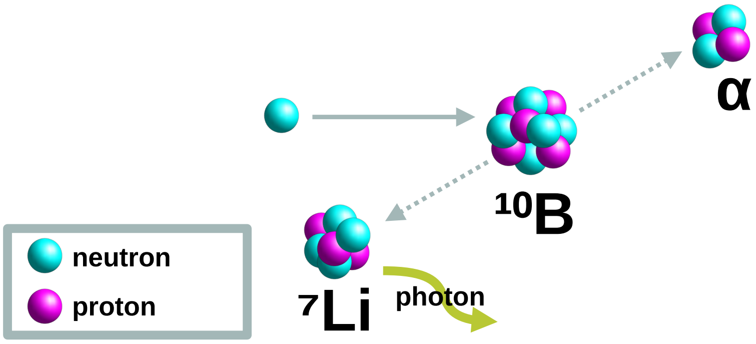

Figure 2.6: Schematic drawing of the ^{10}B neutron capture reaction.

2.2.4 Fission

The stability of an atomic nucleus depends heavily on the configuration of its protons (Z = atomic number) and neutrons (A = mass number). If there are too many protons in a nucleus and not enough neutrons to overcome their mutual repulsion, the nucleus becomes unstable.

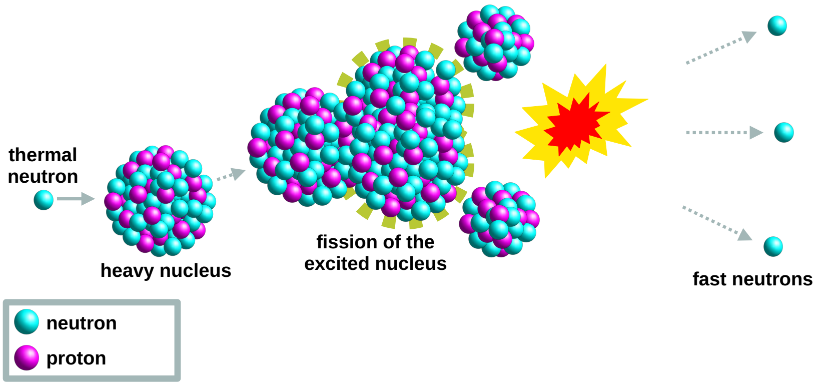

Figure 2.7: Schematic drawing of a neutron induced fission reaction.

If the proton-neutron balance inside a stable nucleus is disturbed by the capture of low-energy neutrons, the nucleus can emit nucleons or α-particles to regain stability. However, the nucleus may also split into two or more daughter nuclei. This process is called nuclear fission. An exemplary schematic drawing of the process is shown in figure 7.2. The daughter nuclei may be either stable or unstable and may undergo further splitting, photon emission, or emission of single nucleons. Although fission and spallation result in similar outcomes regarding nucleon emissions, it is important to understand that spallation is caused by high-energy particles interacting with nucleons, resulting in a nuclear cascade. The term ”fission” is used for nuclear reactions involving low-energy neutrons and heavy unstable nuclei.

3 From Neutron Detection to Neutron Dosimetry

The processes explained in the previous chapter must be considered when discussing neutron detection methods. Due to their lack of electric charge, neutrons are not directly ionizing; that is, their interaction processes do not lead to ionization. However, charged particles created in neutron interaction processes can ionize, so neutrons are considered indirectly ionizing particles [18]. Consequently, in neutron detection, signals are produced in particle detectors by the secondary particles created in neutron interactions. This is common practice in gaseous detectors, which often use ^{3}He for thermal neutron detection [19], but also for scintillator based neutron detectors [20, 21], and semiconductor detectors [6].
Therefore, to achieve high detection efficiencies, it is important to choose materials with large cross sections for neutron interaction processes that create particles capable of producing significant signal responses in a detector. Closer examination of the cross sections of detection materials frequently used for neutron detection, namely ^{3}He , ^{10}B , and ^{6}Li , depicted in figure 3.1, shows significantly higher cross sections for reaction channels relevant to detection at lower neutron energies than at higher energies.

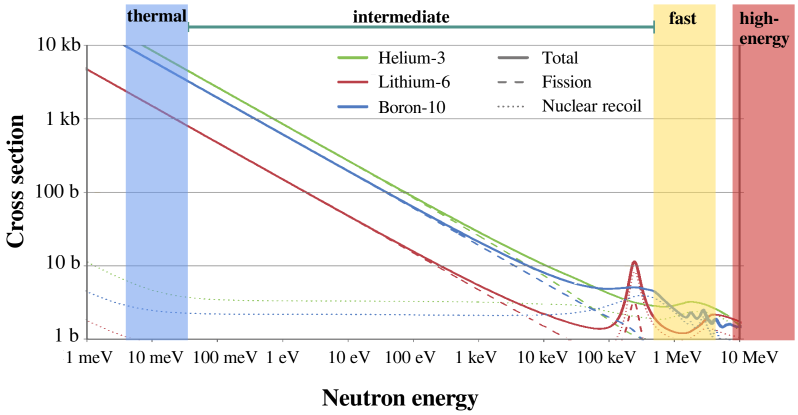

Figure 3.1: Cross sections of different materials for neutron detection. Figure after [22]

As a result, it is common practice to reduce the energy levels of neutrons to the thermal level, due to their significantly higher interaction and, therefore, higher detection probabilities. However, this introduces a limitation: neutron energies cannot be measured directly. Instead, specialised techniques are used to reconstruct neutron energy spectra. The following section discusses the radiation weighting factors used to quantify the biological impact of neutron radiation. This is followed by an explanation of neutron energy spectrum measurement techniques using Bonner Sphere Spectrometer (BSS).

3.1 Neutrons and the Human Body

The neutron interaction processes described in section 2.2 can also occur in the human body. Since water is the main component of human cells, scattering processes dominate and primarily lead to the production of secondary ionizing radiation, namely protons. Depending on the energy of the incident neutron, the resulting secondary protons can reach energies of up to the MeV levels. When assessing the threat to human health, it is important to understand the concept of dose. The term *absorbed dose* is defined as ”[...] the energy absorbed from any type of radiation per unit mass of the absorber” [23] ($D = \mathrm{d}E/\mathrm{d}m$), where D represents the absorbed dose, dE is the energy deposited, and dm is the mass of the absorbing medium. The unit of measurement for absorbed dose is Gy, with $1\,\text{Gy} \mathrel{\hat{=}} 1\,\text{J/kg}$. Since different types of radiation exhibit varying ionization properties, radiation weighting factors (w_R) are introduced to account for their biological effectiveness. Photons have a small Linear Energy Transfer (LET). This means that photons of the same energy will cause fewer ionizations over a certain distance than protons, which have a high LET. To quantify the biological harmfulness of different radiation types, the *equivalent dose* ($H_\text{T,R}$), which is the *absorbed dose* multiplied by the radiation specific weighting factor (w_R):

$$H_\text{T,R} = D \cdot w_\text{R} \quad . \tag{3.1}$$

Unlike other particles, which have a radiation weighting factor that is independent of energy and constant, neutrons have an energy-dependent radiation weighting factor, as shown in figure 3.2. This factor was introduced in ICRP Report 103 [24]. The peak around 1 MeV results from elastic scattering with hydrogen inside the human body and represents the dominant interaction process at these energies [13]. The free protons created in this interaction consequently cause significant harm because their energy is relatively high. The radiation factor decreases with higher neutron energies because neutron interaction cross sections generally decrease with energy.

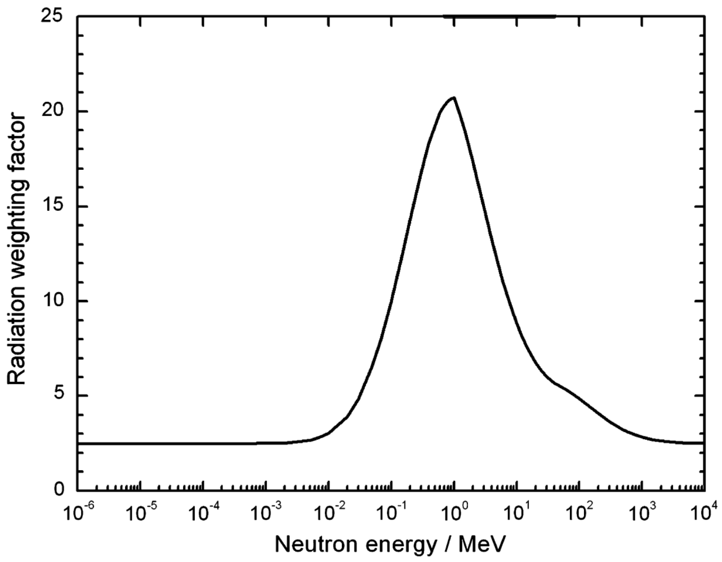

Figure 3.2: Continuous neutron radiation factor as introduced by the ICRP report number 103 [24].

3.2 Bonner Spheres

As mentioned in the introduction to this chapter, neutron energies cannot be measured directly. Therefore, neutrons must be detected through the secondary particles created in neutron interaction processes.

In general, neutron cross sections decrease with increasing neutron energies. Therefore, it is common to reduce the energy level of neutrons to increase the probability of interaction. One example of a detection system that applies this moderation technique is the BSS [25, 26], which was first developed by Bramblett, Ewing and Bonner in the late 1960s. The detector system consists of ^{3}He thermal neutron proportional counters with polyethylene (PE) spheres of varying sizes in which the ^{3}He proportional counters are placed. The PE spheres present a volume in which neutrons undergo multiple scattering processes until they are moderated down to thermal energy levels. The larger the radius, the larger the moderator volume, and the higher the initial neutron energy that can be moderated inside the sphere. For energies above 10 MeV, additional spheres with additional lead inserts are used, as shown in figure 3.3. The dominant interaction process for fast neutrons is inelastic scattering, as discussed in section2.2.2 of chapter 2. The energy loss due to inelastic scattering cannot be quantified. However, it can be estimated to be at least equal to the energy of the lowest excited state of the moderating material. In this case, the lowest excited state of lead is 0.58 MeV. Therefore, lead becomes almost transparent to neutrons with energies below that. These neutrons are further moderated by the PE surrounding the ^{3}He proportional counter. Extended-range BSS were developed by [27], allowing the detection of neutrons with energies in the GeV range by adding additional lead layers. However, these energies do not play a role in a clinical environment, as the maximum neutron energies are equal to the initial proton energy that sparked their production process, as described in chapter 2.

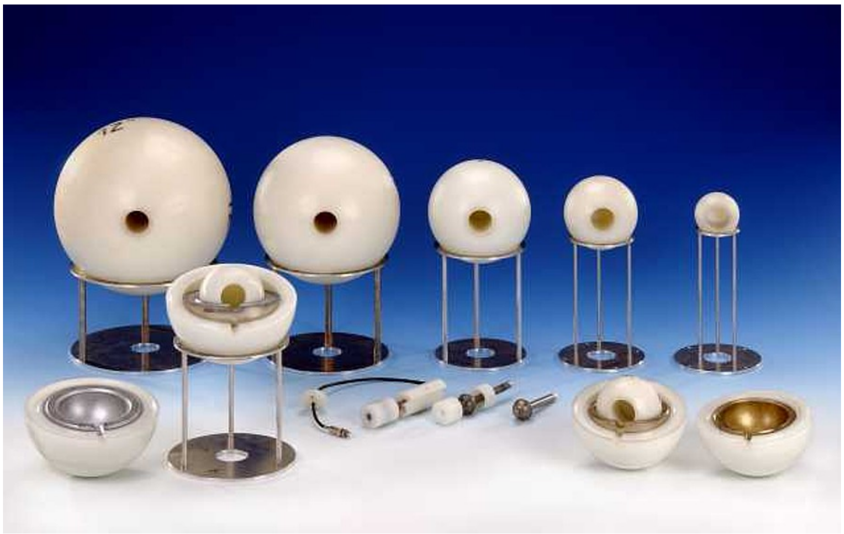

Figure 3.3: Bonner Sphere Spectrometer. Picture taken from [26].

A BSS detector system can contain up to 13 spheres. To derive the continuous energy spectrum of neutrons over several orders of magnitude, as shown in figure 2.1, complex mathematical unfolding algorithms must be applied to the data taken with a limited number of Bonner spheres, as discussed in [28, 29].

3.3 Neutron Dosimetry

Considering that neutron radiation weighting factors are highly energy dependent, it would be desirable to measure neutron energies directly in order to accurately determine the health hazard to humans. However, this is not possible due to neutrons' indirect ionizing properties and the energy-dependent cross sections of the neutron converters that must be used to convert neutrons into detectable charged particles. Using neutron converters also creates a signal inside a particle detector that is not dependent on neutron energy. Nevertheless, monitoring neutron exposure is important for assessing the health risk to exposed humans. Official German dosimetry regulations use a complex system to determine the neutron dose for exposed individuals, which will be explained in the following subsection.

3.3.1 Albedo

In German personal neutron dosimetry, the Albedo principle is used [30]. The detector itself consists of four detector kernels, which are thermo luminescence detectors (TLDs) in the case described here. However, according to the European Radiation Dosimetry Group e.V. (EURADOS) intercomparison study [31], one Albedo detector system that took part in the study contained Optically Stimulated Luminescence (OSL) detectors.

These two passive dosimetry systems use the same particle detection principle: when energy is deposited in certain crystalline materials, electrons from the valence band can move to the conduction band. Between the two bands lies a band gap where electrons can become trapped when crossing it. When these detector systems are then heated (for the thermo luminescence detector (TLD) systems) or optically stimulated (for the OSL systems), these traps can be emptied [32]. This process is accompanied by photon emission. These detector types are used not only for neutron detection but also for directly ionizing particle detection. They are passive dosimeters, meaning they are read after a predefined time span and only then provide information about the collected dose.

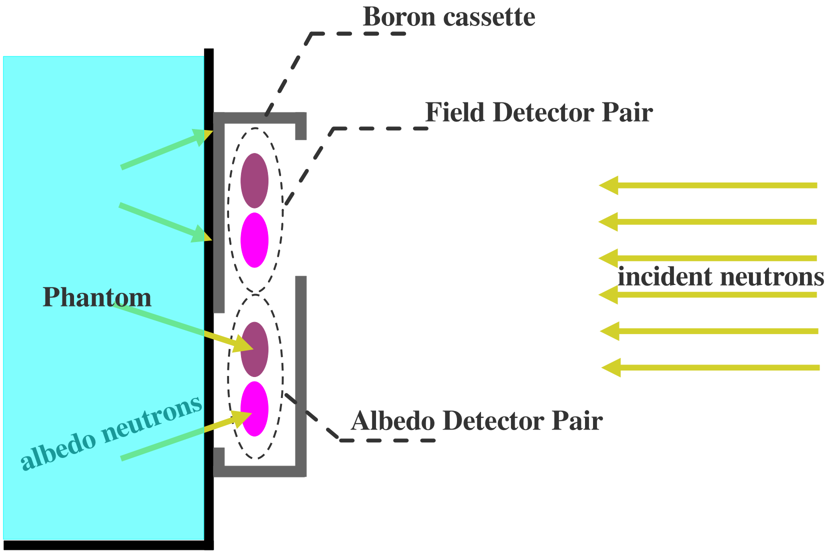

Figure 3.4: Albedo detection principle.

Figure 3.4 displays the detection principle for an Albedo system based on a Thermo Luminescence Dosimeter (TL-DOS) detector [33]. The system consists of two detector pairs, one being sensitive to photons only and the other one being sensitive to photons and neutrons. The Harshaw TLD-based detector system uses ^{6}Li and ^{7}Li . Only the ^{6}Li detector is sensitive for neutrons and photons. The neutron signal is determined by subtracting the ^{7}Li signal from the ^{6}Li signal.

One detector pair is used to detect field neutrons, and one pair detects so-called albedo neutrons that are backscattered into the detector volume from the phantom

/ the client. The neutron dose is determined by multiplying the albedo neutron signal by a *relative neutron calibration factor*. This factor depends on the field of application of the albedo detector and represents the ratio of field to albedo neutrons.

3.3.2 Etched Track Detectors

Etched track detectors are a popular alternative to TLDs in the field of passive personal dosimeters [34, 35]. These detectors record the tracks of charged particles with high LET, produced by neutron interactions within a solid-state material. The deposited energy from secondaries originating from neutron interactions changes the material's local chemical composition. Track length is determined by the kinetic energy of secondary particles created in neutron interactions. Therefore, the length of the tracks of secondary particles in the material provides information about the initial energy of the colliding neutron.

After being exposed to a chemical etching process, the tracks on the detector become visible under a microscope. They can then be counted to determine the neutron dose. The lowest energy resolvable with etched track detectors is determined by the minimum track length of a secondary particle resolvable in further analysis of the etched tracks. Electrochemical etching processes allow one to resolve track lengths of neutrons with kinetic energies around 100 kiloeV [36].

A notable benefit of etched track detectors is their capacity to provide a permanent record of neutron exposure, which can be re-evaluated as needed.Moreover, they are relatively simple and cost-effective to produce and use. However, as with TLDs,they do not offer real-time dose information, a deficiency that can be a limitation in environments where neutron flux can rise rapidly. In addition, the implementation of a real-time warning system capable of detecting rapid increases in neutron flux would contribute to the enhancement of safety conditions in such environments. This is where active neutron dosimeters come into play.

3.3.3 Active Personal Neutron Dosimeters

According to Gomez-Ros et al [37], electronic neutron personal dosimeters are experiencing a surge in popularity due to their capacity for real-time dose measurement. The detection principle generally entails the utilization of an active solid-state particle detector, namely a silicon detector, in conjunction with a converter layer that facilitates the conversion of neutrons into charged particles through the process of neutron capture reactions, as described in chapter 2.2. The signal created by the secondary particles that are charged and result from the neutron interaction process inside the converter is read out electronically and converted into a dose value inside the device. Presently, electronic personal dosimeters have not received official approval for personal dosimetry in Germany. Nevertheless, electronic personal dosimeters represent a recent technological development, as evidenced by a recent initiative undertaken by the Istituto Nazionale di Fisica Nucleare (INFN) [10].

4 Neutron detection with Si

As discussed in chapter 2, neutrons are indirectly ionizing particles.This implies that solely the secondaries resulting from neutron interaction processes will generate a signal in particle detectors due to ionization processes. The neutron detector developed in the scope of this thesis is based on silicon sensors. The selection was determined by the availability of the sensor and the extensive experience within the working group to which I belong. The working principle of silicon detectors, as well as the specific silicon sensors utilized in this study, are described in section 4.3. Section 4.1 describes the converters used for the neutron detector. Further, signal creation in silicon, as well as the detector readout chain is discussed and explained in detail within the following chapter.

4.1 Converter

When considering the application of neutron detection with a particular particle detector, it is imperative to be aware of the specific reaction processes that contribute to signal generation in the designated particle detector, along with the associated cross sections for these interaction processes. The total neutron cross section for Si is depicted in figure 4.1a. The figure displays the total neutron cross section for ^{28}Si as it is the Si isotope with the highest abundance (92.23 % [*38*]) in natural silicon.

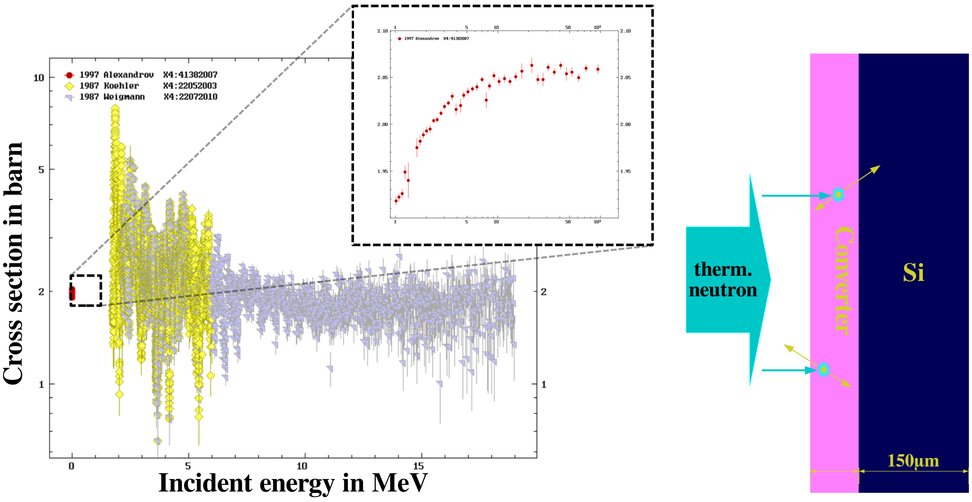

(a) Total neutron cross section for Si. Data taken from [39].

(b) Signal creation in silicon detectors.

It becomes clear that the cross section ranging between $\approx 1\,\mathrm{b}$ and $\approx 10\,\mathrm{b}$, depending on the neutron energy, is inadequate to achieve sufficiently high neutron conversion rates.

Consequently, alternative converters must be considered, with these converters being introduced externally to the detector layout. In figure 4.1b , the process of signal creation through indirect neutron detection using silicon is demonstrated. The most prevalent converters, in conjunction with semiconductor detectors, are ^{3}He , ^{10}B or ^{6}Li [5, 6, 22, 37].

The cross section for thermal neutron capture in ^{10}B is 3835 b [40] as it can be seen in figure 4.2. In the event of a neutron being captured by a ^{10}B nucleus, two distinct processes may ensue, each exhibiting a disparate relative incidence. These processes both culminate in the emission of an α-particle and a ^{7}Li particle:

$$\begin{aligned} {}^{10}\mathrm{B} + \mathrm{n} &\xrightarrow{94\,\%} {}^{7}\mathrm{Li}\,(0.84\,\mathrm{MeV}) + \alpha(1.47\,\mathrm{MeV}) + \gamma\,(0.48\,\mathrm{MeV}) \\ &\xrightarrow{6\,\%} {}^{7}\mathrm{Li}(1.01\,\mathrm{MeV}) + \alpha(1.78\,\mathrm{MeV}\,) \quad . \end{aligned}$$

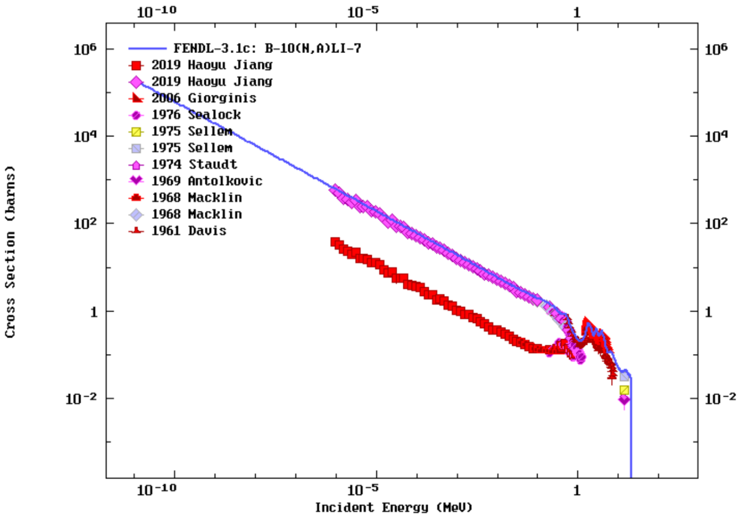

Figure 4.2: Experimental data for neutron capture cross-section for ^{10}B (n, α) ^{7}Li + (γ) extracted from the EXFOR data base [39] , along with the "Fusion Evaluated Nuclear Data Library" (FENDL)[41] values plotted in blue.

The maximum range for α-particles in boron is 3.2 µm (at 1.47 MeV), respectively 3.9 µm (at 1.78 MeV) [42]. The small ranges in boron require rather small converter thicknesses to allow the reaction products to escape from the volume. At the same time, thicker converter layers result in a higher neutron conversion rate. As part of my master's thesis [43] I performed several Geant4 [44] simulations to identify an ideal converter thickness. The simulated material was ^{10}B enriched B_4C because free boron is toxic and difficult to deposit on surfaces.However, in its bonded state with carbide, it is also used in tool manufacturing to harden the surfaces of special drills, making them more durable. The simulation results show that at a thickness of $\approx$ 2 µm a maximum of α-particle escapes from the converter. This is also in good agreement with publications investigating B_4C thin film coatings for thermal neutron detection [6, 42]. The simulation of different converter positions with respect to the silicon sensor performed within our working group [45] shows that the neutron detection efficiency can be increased when a converter is facing the front and the back side of a silicon sensor.

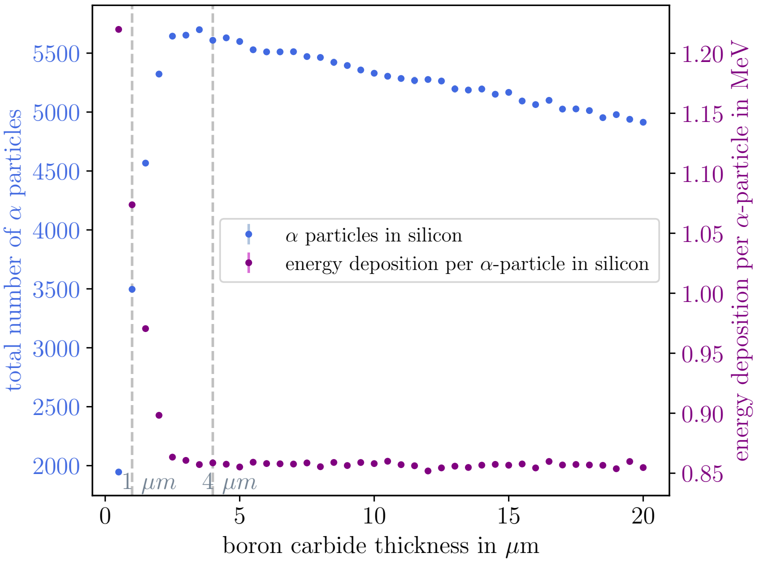

Figure 4.3: Total number of secondary α-particles and the energy deposition per α-particle as a function of B_4C thickness. [43]

4.2 Physical Vapor Deposition - Sputtering

The coating process of Physical Vapor Deposition (PVD) is a thin film coating technique that is used to achieve coating layer thicknesses in the order of µm. In this process Argon atoms are accelerated by an electrical field onto a target (coating) material inside a vacuum chamber. The accelerated argon particles strike the target material so that these target particles distribute ideal gas like inside the chamber so that everything inside the vacuum chamber is coated by the target particles which are in the case of this work ^{10}B enriched B_4C particles. Figure 4.4 shows a drawing of the sputtering process. A target material of ^{10}B enriched boron carbide was used as only ^{10}B has the high neutron capture cross section due to its odd-odd nucleus with five protons and five neutrons.

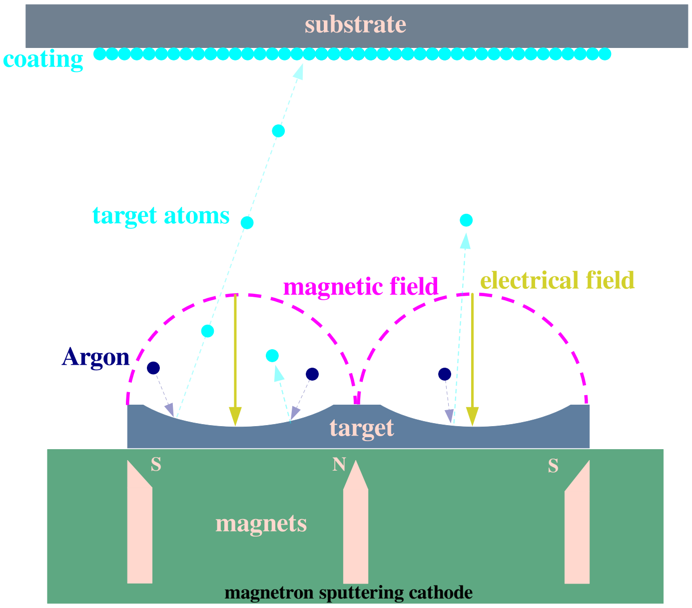

Figure 4.4: Schematic drawing of the sputtering process. Drawing after [*46*]

4.2.1 ^{10}B enriched B_4C Converter Production

The PVD of the B_4C was carried out by the European Spallation Source (ESS) in Lund, Sweden. At the coating workshop, it is possible to order the coating of a target material with a desired thickness. For this work, we ordered two aluminum sheets each with a thickness of 300 µm, and a size of $65 \times 120\,\text{mm}^2$. The thickness of the thin film coating is contingent upon its position within the chamber. Figure 4.5 illustrates the thickness variation of the boron carbide layer on the aluminum carrier sheet.

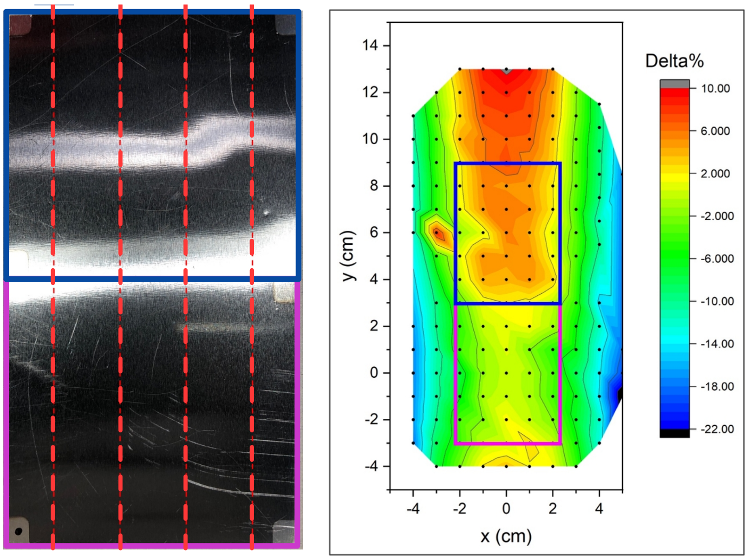

Figure 4.5: Converter on aluminum sheet with cutting edges marked in red, and the visualization of the thickness variation on the right. Pictures and graph taken from internal communication with ESS [47].

We ordered two sheets: one with a boron carbide reference thickness of 2 µm and one with 4 µm. As illustrated in 4.5, a coated carrier sheet is presented, which is subsequently divided according to the red dashed lines. These plates are available in increments of either 2 µm and 4 µm, depending on the position along the aluminum sheet. The result of this process is the creation of the thickest converter available, with a thickness of 4 µm plus 6 %, resulting in a total thickness of 4.24 µm for the converter cut out in the middle of the upper half of the aluminum sheet shown in figure 4.5. The cut out taken from the lower part of the sheet in the middle, both have exactly 2 and respectively 4 µm.

4.3 Silicon Detectors

Once the secondary particles produced in the reaction processes described in chapter 4.1 reach the silicon sensor, they will deposit energy and consequently generate a signal close to the sensors surface. To explain the signal generation in the detector developed in this thesis, it is important to understand the functionality of semiconductors, and the circumstances under which they can be used as particle detectors.

In solid state detectors, the energy levels of certain level atom groups lie so closely together that they form an energy band. Atom groups with different distances in energy form separate energy bands. The energy distance between the energy bands is called band gap. The two bands with the highest energy levels are called valence band and conduction band. In a conductor, the two bands overlap, allowing the positive (holes) and negative (electrons) charge carriers to move freely from the valence to the conduction band.

In an insulator, the band gap can bes as large as 9 eV, which carriers cannot cross. In a semiconductor, the band gap between the valence and the conduction band is in the order of a few eV.

In some semiconductors, an energy gain due to thermal excitation can be sufficient to excite carriers from the valence band into the conduction band. The sensor material used in this work is silicon, which has a band gap of 1.12 eV [48]. However, an average energy of 3.65 eV [48] is required at room temperature to create an electron-hole (e/h) pair inside a silicon sensor. Figure 4.6a provides the explanation for that: The band structures are shifted in k-space so that the two extrema of the energy levels are not at a minimum distance. This distance can be overcome by lattice excitation. Semiconductors with these characteristic band structures are called indirect semiconductors.

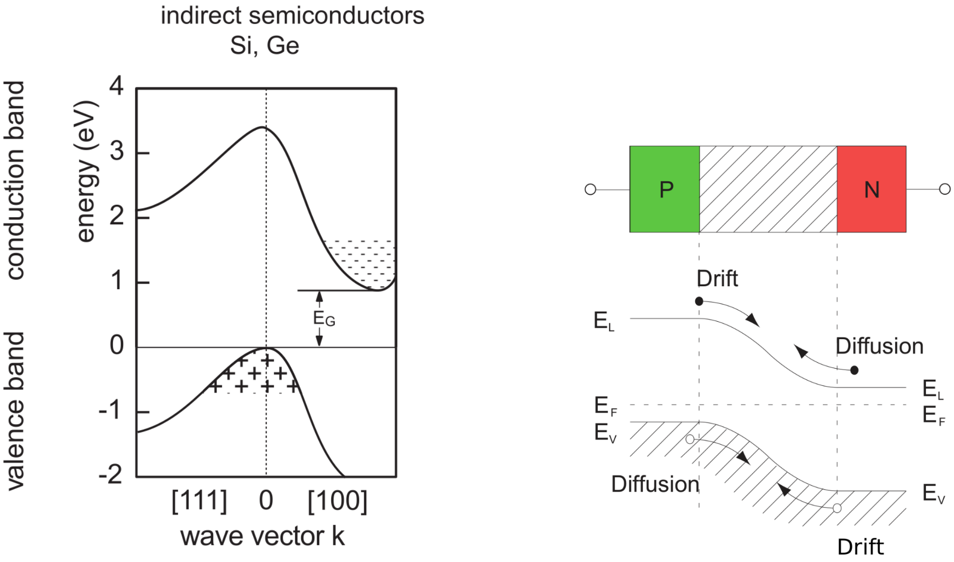

(a) Schematic drawing of the band structures inside indirect semiconductors. [48]

(b) Schematic display of a PN-junction in a semiconductor with it's band structure. Figure after [48].

The band gap of silicon itself is not enough to turn a silicon sensor into a particle detector. A characteristic feature of silicon particle detectors is doping to increase its conductivity. Doping describes the introduction of an atom from the third or fifth column of the periodic table (trivalent or pentavalent elements respectively). When introducing an element from the third column, such as boron, it creates a free hole in the lattice (p-doping). Similarly, when doping silicon with an element from the fifth column, such as phosphorus or arsenic, it introduces a free electron in the lattice (n-doping). Figure 4.7 displays a schematic drawing of the differences between n-doped and p-doped silicon.

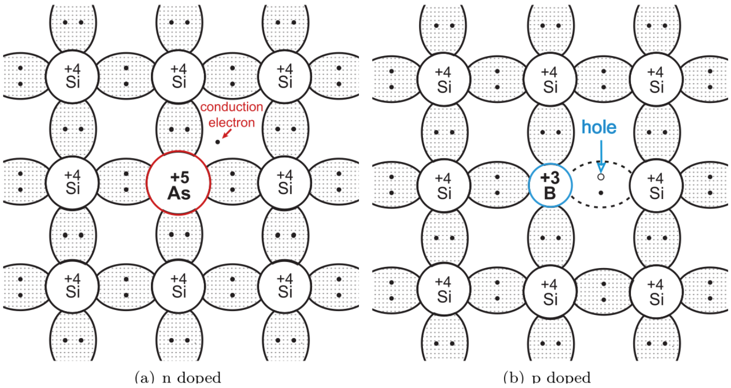

(a) n doped (b) p doped

Figure 4.7: Schematic drawing of n- and p-doped silicon [48].

The free charge carriers within the doped silicon layers undergo a temperature-driven random walk. When a p-doped and a n-doped layer come into contact, the difference in charge carrier densities induces a net movement from regions of high concentration to regions of low concentration, a process known as diffusion current. As electrons and holes migrate freely, they eventually recombine, forming a depletion zone with (almost) no free charge carriers.

However, the remaining ionized donors or acceptors from the dopant atoms are stationary and now lack either an electron or a hole. These stationary ions create an electric field inside the silicon sensor that causes charge carrier motion in the opposite direction to the diffusion current. The opposing charge carrier motion due to drift and diffusion results in a limited depletion zone.

Applying a positive potential to the n-doped silicon electrode, and a negative to the p-doped electrode results in the expansion of the depletion zone. Since the depletion zone represents the active detector volume, it is desired to extend it through the entire sensor without causing a break down which is the expansion beyond the opposing electrodes causing an uncontrolled current flow. The voltage required to fully deplete a sensor depends on its thickness and its effective doping, and can be determined experimentally.

4.4 Signal Creation in Silicon

When charged particles, such as secondary α-particles , enter the active volume of a fully depleted semiconductor detector, they interact with the lattice atoms and generate e/h pairs through ionization. The energy loss of heavy charged particles in matter is well described by the *Bethe-Bloch* formula. The number of generated e/h pairs depends on the particle's kinetic energy, its LET, and the average energy required for pair creation in the detector material.

In this work, a silicon sensor is used. As discussed in the previous section, the average energy required to create an e/h pair in silicon at room temperature is 3.65 eV [48].

The neutron detector developed in this thesis is used together with a neutron converter in which α-particles are created upon neutron interaction. These α-particles with 1.47 MeV and 1.78 MeV have a high LET and thus deposit their energy locally within a few µm of the silicon sensor. Once the charge carriers are created in the silicon sensor, they are separated by the external electric field and drift toward the opposing electrodes: electrons move toward the positively biased electrode, while holes move toward the negatively biased electrode. As they travel, their motion induces an image charge on the collecting electrodes.

Figure 4.8a shows the signal evolution of a signal generated by an α-particle , while figure 4.8b shows the signal development of a signal generated by an electron.

The signal created by an α-particle shows the characteristics of a step function with two steep declines: The first decline after the electrons reach the electrode, and the second when the holes reach the opposing electrode. The steep declines can be explained by the local energy deposition of α-particles , resulting in almost identical arrival times at the electrodes for electrons and holes.

The electron signal in contrary, shows a less steep decline of the current as the charge carriers are created throughout the whole sensor, resulting in equally distributed paths, and an almost immediate signal decay as soon as the first charge carriers reach the electrodes.

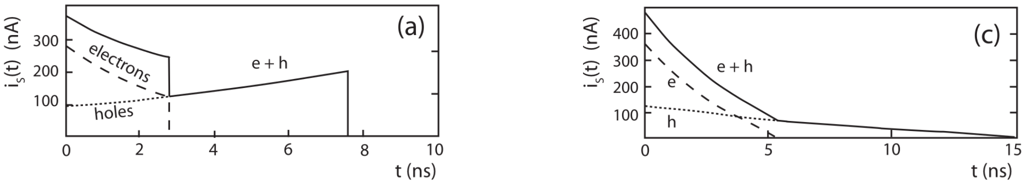

(a)

(b)

Figure 4.8: Signal evolution in silicon due to an α-particle (a) and an electron (b). [48]

4.5 Signal Processing

The charges generated inside the sensor that is used in this work are in the order of fC. This requires for amplification suitable to the use case and further processing of the data. In this work two different types of amplifiers are used: A ”CX Spectroscopic Shaping Amplifier” [49], and a ”C2 TCT Amplifier” [50]. The two model names indicate their different functionalities, which are explained as follows.

4.5.1 CX Spectroscopic Shaping Amplifier

The ”CX Spectroscopic Shaping Amplifier” is a charge sensitive shaping amplifier with a capacitive feedback in the preamplification stage as depicted in figure 4.9. The preamplification stage with the Operational Amplifier (OpAmp) inverts the signal. In addition, the signal is shaped inside the amplifier which is typically realized by a high pass filter followed by a low pass filter.

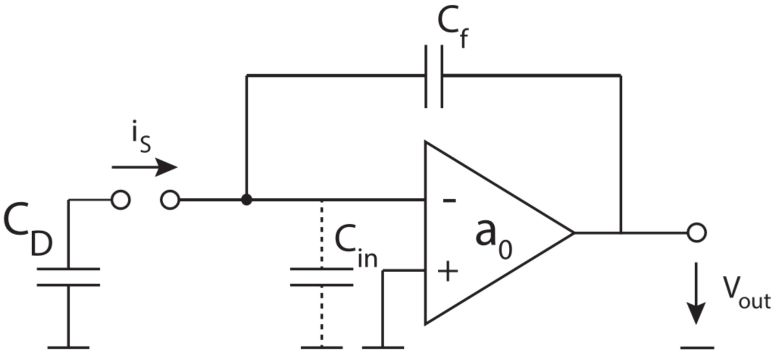

Figure 4.9: First amplification stage for a charge sensitive amplifier with a capacitive feedback loop onto the inverting entrance of the operational amplifier [48].

Within an integrating amplifier as the ”CX Spectroscopic Shaping Amplifier” the integral over the output current is proportional to the input current. Figure 4.10 shows a signal amplified by the ”CX Spectroscopic Shaping Amplifier”. It has a gaussian shaped output signal that is coupled with the characteristic capacitor discharge on the trailing edge of the signal. With this amplifier, only the peak height provides an information about the particle that created the signal, since the pulse shape is determined by the amplifier characteristic. The ”CX Spectroscopic Shaping Amplifier” has a characteristic pulse width at full width half max of 180 ns according to the data sheet.

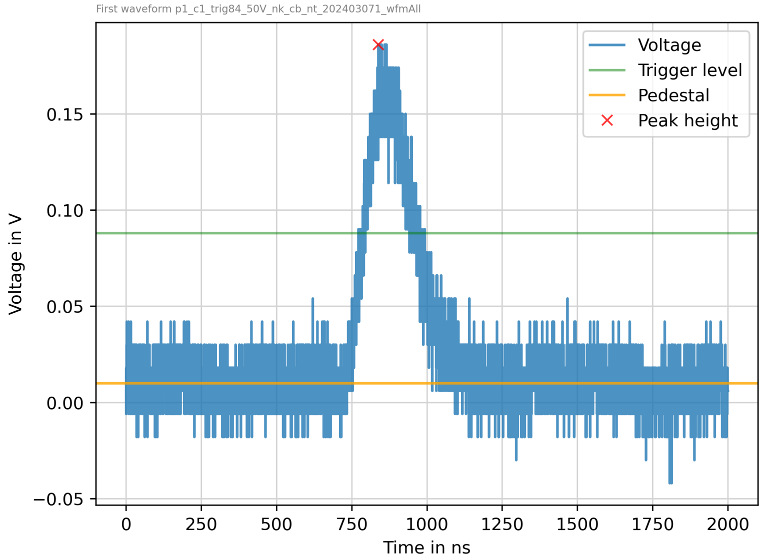

Figure 4.10: Example waveform taken with a silicon detector and the ”CX Spectroscopic Shaping Amplifier”.

The data points outside the peak area show a certain dispersion. This is due to electronic noise coming from the detector and readout system. It is important to determine the noise for each detector and amplifier individually, as they can differ tremendously. It is also visible that the data points forming the non-signal part of the data set do not scatter around zero, but display a particular offset that is not zero. This offset, sometimes referred to as pedestal, has to be determined for each data set individually if it changes significantly. Another value marked in the example plot is the so called trigger level which is the threshold level that determines whether a signal is recorded or not. As soon as the leading edge of the approximately Gaussian-shaped signal rises above this level, the readout system is triggered to save the time and voltage data of that particular signal. Lastly, the peak value, which is defined as the maximum value of the data set in this case, is marked as a first approximation. The whole data post-processing and filtering is described in section6.4.

4.5.2 Cividec C2 TCT Amplifier

The second amplifier used in this work, the Cividec "C2 TCT Amplifier", is a transimpedance amplifier that can be realized by an emitter circuit with fast transistors. The amplification of an emitter circuit is well discussed in [51]. Its basic functionality can be reduced to the fact that a small change in current at the base results in a large amplification of the signal at the collector output of the transistor. A characteristic feature is the fast amplification of signals. This is extremely valuable when retrieving time-critical signal evolution information, allowing the measurement of the time-dependent shape of a signal.

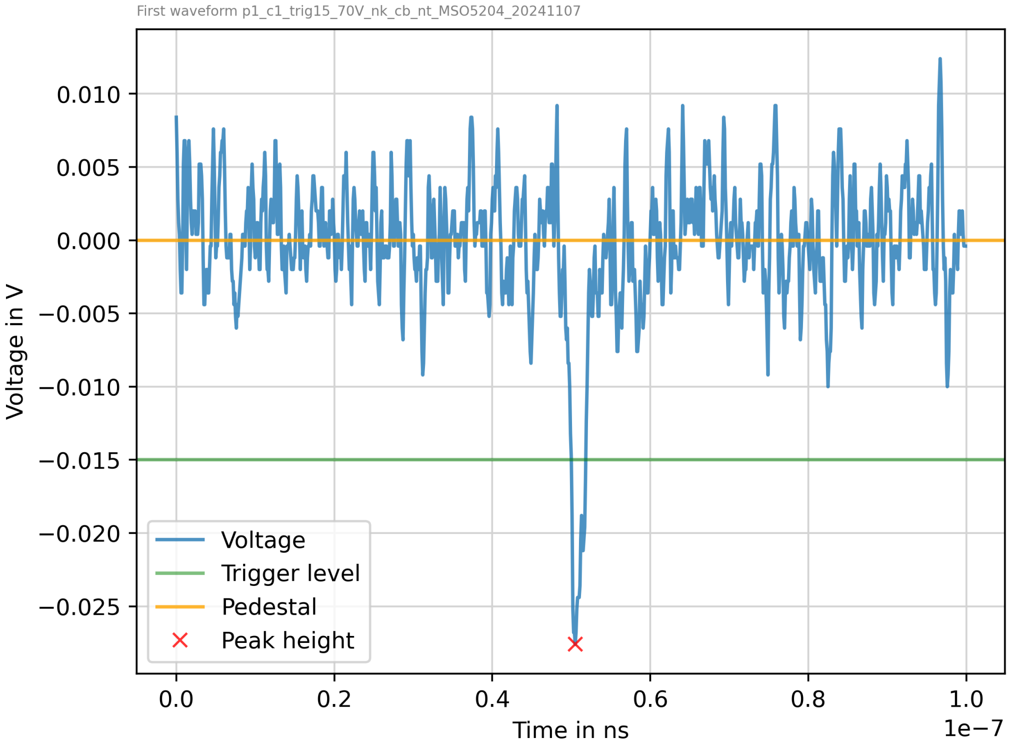

Figure 4.11: Example waveform taken with a silicon detector and a TCT amplifier.

Figure 4.11 shows a signal that was amplified by the Cividec "C2 TCT Amplifier". In contrast to figure 4.10, the signal is not inverted, resulting in a negative voltage pulse in our case. In addition, the pulse displays a smaller pulse height and width with significantly steeper leading and trailing edges. The shape is highly individual and depends on the interaction processes the particle that created the signal has undergone in the sensor as discussed in section4.4. The smaller amplification results also in a significantly smaller noise i.e. scattering of data points around the pedestal. The two waveforms on display in figure 4.10 and 4.11 are chosen randomly from the first measurement campaigns and are used at this point to demonstrate the different working principles of the amplifiers used in this work. The following chapters will dive deeper into the detector and readout set up characterization that was developed in the scope of this work.

5 Prototype Development and Characterization

While chapter 4 provides the theoretical background to semiconductor detectors and their readout, the following chapter explains how a first prototype neutron detector was developed. First steps include sensor descriptions, investigations of the sensor characteristics, and noise investigations of the detector system. At the end of this chapter, the post-processing of the data acquired with the first prototype together with the ”CX Spectroscopic Shaping Amplifier” is explained.

5.1 Sensor Investigations

The silicon sensors are diodes with a size of $(3.20 \pm 0.05) \times (3.20 \pm 0.05)\,\mathrm{mm}^2$ and a thickness of 150 µm. They stem from wafers on which prototypes for novel silicon pixel and strip sensors were produced ([52, 53]). Figure 5.1 shows an image of one of the wafers together with a display of a layer of the wafer's gsd file. The diodes that are reasonably smaller than the strip sensors are so called test structures. They are produced in the free space between the individual strip sensors.

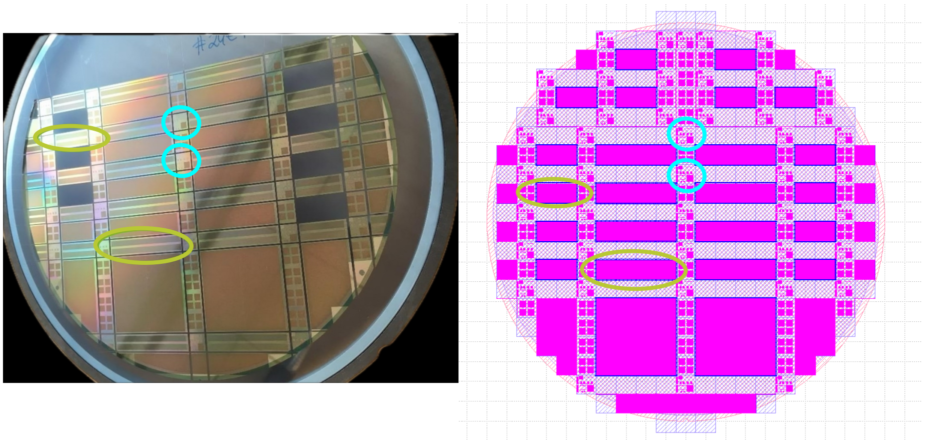

Figure 5.1: CMOS Wafer with technical drawing (gsd file). Strip sensors marked in green and diodes used in this work marked in blue.

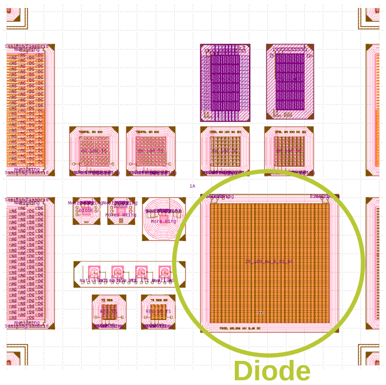

Figure 5.2: Exemplary layer of the gsd file of the diode used for the prototype.

The test structures can include small diodes in the sub mm range with multiple guard rings to test their functionality. On this wafer, the test structures contained multiple pixelated diodes with different implantations. Figure 5.2 shows the technical drawing of the diode that is used for the neutron detector. The pixelated structure, and the conducting connections between the individual pixels are also shown. The image also contains the technical drawings of the aforementioned smaller test structures that are not used in this work.

Even though the diode is pixelized, the technical drawing data shows that the individual pixels are connected to each other, making the pixelized diode work as one electrode with a homogeneous surface. The pixel size is 25 × 100 µm, and the front and backside of the sensor have a few µm thin metallization layer consisting of 96.5 % Al, and 5 % Si. The metallization layers are needed to provide a conductive contact to the sensor.

5.2 IV CV characterization

As described in section 4.4, each silicon sensor has an individual depletion voltage that depends on the charge carrier density in the bulk and the sensor thickness (150 µm). As a first investigation a so-called current-voltage characteristic (IV curve) was taken which records the characteristic curing of the diode in reverse bias. The IV characteristic for the sensor used for the first prototype is displayed in figure 5.3. It shows the breakthrough behavior with almost no increase across the smaller voltages applied, followed by a sudden increase in current flow through the sensor. The voltage at which this happens is called breakthrough voltage (U_{bd}). For this particular measurement the voltage applied to the sensor is ramped up from 0 to 200 V in steps of 10 V. The breakthrough voltage is defined as the voltage value that is at 120 % of the previous current value. For this sensor U_{bd} is found to be around 170 V. Figure 5.3 displays the small current through the sensor (leakage current) in the plateau region between 0 and 125 V where the leakage current is below 1 nA. For the later defined depletion voltage of 50 V the leakage current is (0.420 ± 0.002) nA.

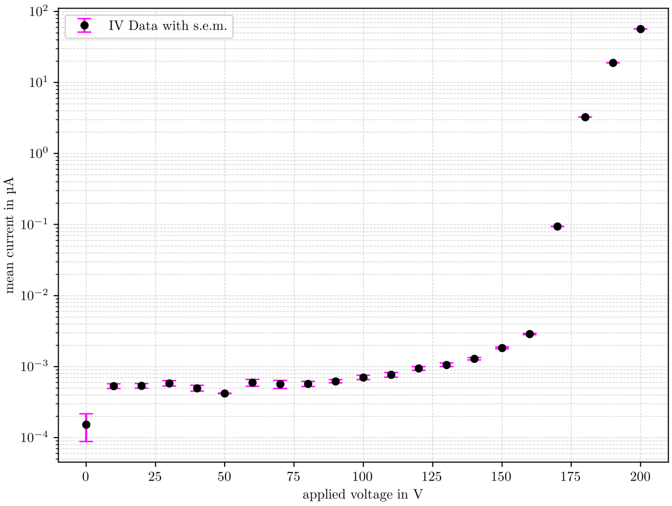

Figure 5.3: Current-Voltage characteristic for the sensor used for the first prototpye.

The IV measurement serves as a first estimate of the voltage that can be applied to the sensor without damaging it by passing too high currents through it. This has two main reasons: First, an increase in leakage current consequently causes an increase of the noise signal. Second, high currents inside the sensor will cause local heating and eventually physical damage to the sensor.

To determine the voltage required for full depletion of a sensor, a capacitance-voltage (CV) measurement is performed. In this method, an increasing DC bias voltage is applied to the sensor while a small AC signal is superimposed. The bias voltage expands the space charge region, while the AC signal allows for capacitance measurement at the corresponding depletion width.

Capacitance is defined as the change in charge per unit change in voltage. As the applied DC bias increases, charge carriers are progressively removed from the expanding space charge region. Due to the resulting depletion of free charge carriers, the capacitance gradually decreases.

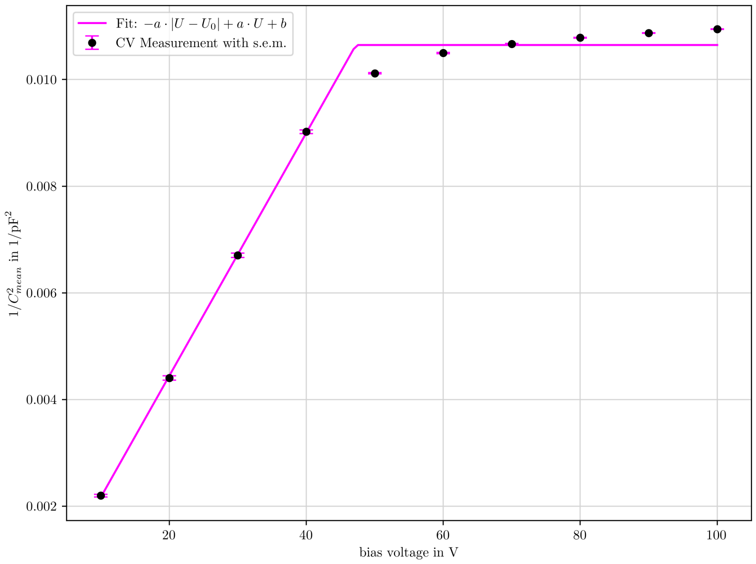

Figure 5.4: Capacitance-Voltage characteristic of the diode used for the first prototype. The

The capacitance of a diode is proportional to $\frac{1}{U_{\text{bias}}}$, so in figure 5.4 $\frac{1}{\mathrm{C}^2}$ is plotted. The capacitance drops almost linearly for increasing bias voltage values up to an applied voltage of around 50 V. After that the values form a plateau. The conclusion of this measurement is that the sensor is fully depleted from 50 V and above. The depletion voltage is determined at (47.7 ± 1.1) V by using the following fit function that describes the $\frac{1}{c^2}$ measured data points:

$$\frac{1}{c^2} = -a|U - \mathrm{U}_0| + aU + b \quad . \tag{5.1}$$

5.3 Read Out Board

To be able to read out the signal generated in a silicon sensor, and to apply the depletion voltage, the sensor has to be mounted on a structure, a readout board, which is designed to fit individual needs. The main features of a readout board are depicted and labeled in figure 5.5. It contains a ground pad which is a metallized contact that is connected to the outer contacts of the SubMiniature version A (SMA) connector on the board. The sensor is glued on that contact pad with conductive glue which connects the back side of the sensor, specifically the n-implant, to ground.

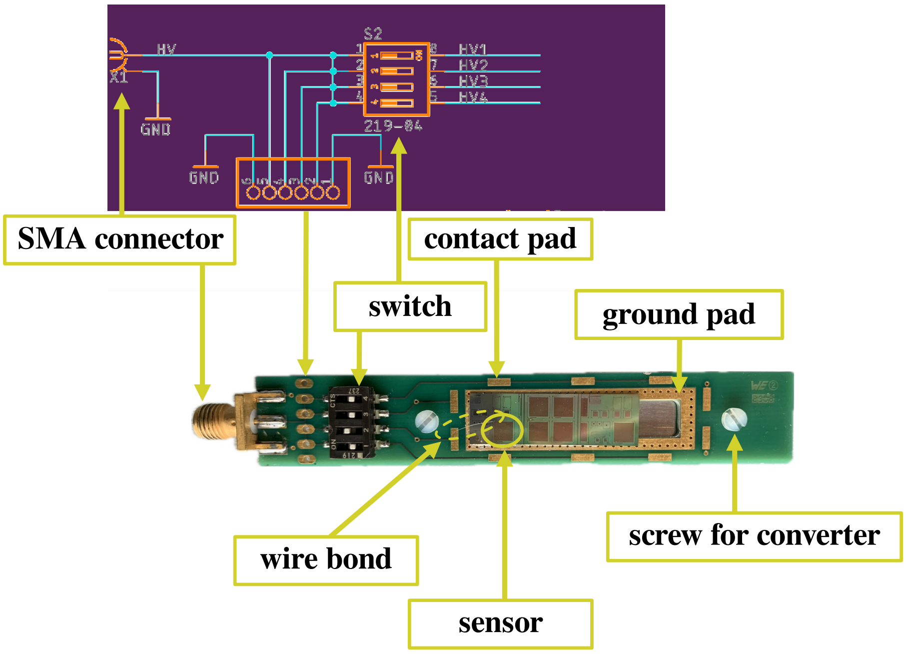

Figure 5.5: Read out board with circuit diagram (with a purple background).

Furthermore, the board contains a contact pad to establish the connection between the p-implant, namely the upper side of the diode, and the inner conductor of the SMA connector. This connection is realized by a so called wire bond.

The first readout board was designed for simultaneous readout of multiple diodes. Therefore, the board included a larger ground surface area to be able to mount multiple sensors onto the board. The ground area has a cutout which is needed for a neutron converter to be mounted in a way that the charged secondaries can impinge the backside of the sensor. To read out multiple diodes individually or all together, the board contains multiple contact pads with individual traces leading to the switch to turn individual traces on or off. The screw holes marked in the figure are designed to mount interchangeable neutron converters on carrier plates. Additionally, the board comes with contacts that allow for multiple readout boards to be mounted on top of each other (named JP1 in the sketch) to potentially investigate detection efficiency enhancing setups.

As mentioned in section 4.5, the detector signal is amplified by either a spectroscopic or a fast transimpedance amplifier, depending on the use case. The amplifier output is connected to an oscilloscope that displays the signal delivered by the detector system.

5.4 Noise Investigations

To investigate the noise contribution due to the capacitance of the readout board at the amplifier input, a systematic assembly of the electronic components of the readout board as depicted in figure 5.6, is performed.

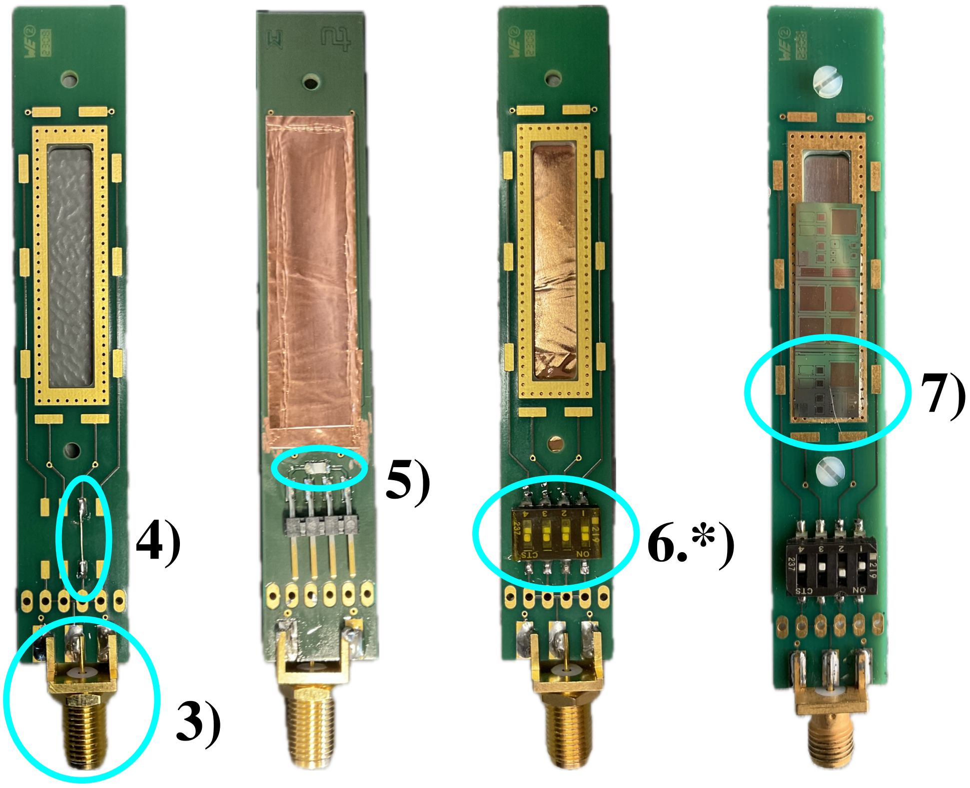

Figure 5.6: Visualization of the detector assembly with the numbering to match table 5.1. Assembly steps 1) and 2) are investigations of the amplifier connected to the oscilloscpe, and are therefore not on display.

For this purpose, the readout board is assembled step by step, and the Root Mean Square (RMS) of the output voltage is recorded. The RMS is the root of the mean of the squared voltage values displayed in the oscilloscope screen. If more than one waveform is taken for that measurement the oscilloscope also records the minimum and maximum value of the RMS of all waveforms taken. The mean RMS consequently is a measure of the offset of the signal. To determine a conservative estimate of the introduced noise of the individual assembly steps, the difference between the maximum and minimum RMS value is determined and shown in table 5.1.

The trigger level for the first measurement is set to 0 mV. The trigger mode for all measurements is set to normal which means that the oscilloscope only triggers when a signal crosses the trigger threshold.
The trigger level for later measurements is set to 14 mV. Each measurement contains between 500 and 1000 waveforms so that the RMS value in the ocilloscope screen was stable. Measurements that contained maximum RMS values that can be associated with electrical switching processes, as shown in figure 5.7, are discarded as they can clearly be associated with electrical switching of devices present in the laboratory environment. They differ significantly in shape and amplitude from the intrinsic noise of the detector system, which has a constant baseline.

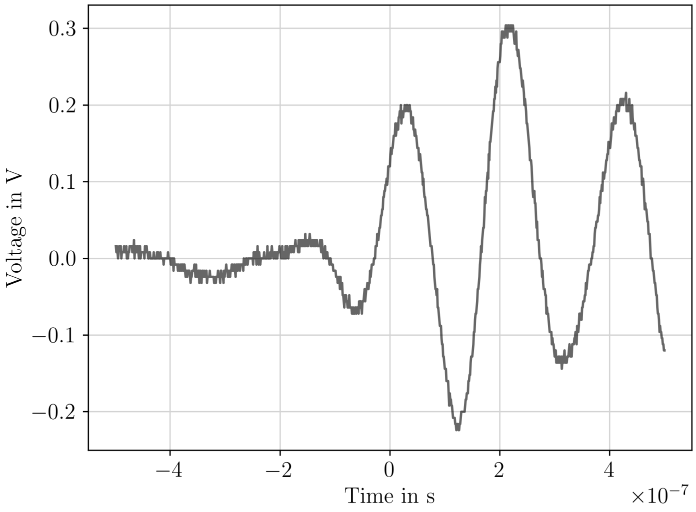

Figure 5.7: An exemplary electronic signal that was coupled in when the light switch inside the experimental room was flicked.

The assembly of the readout board and the subsequent noise measurement could show that each of the components mounted on the board increased the noise, because they increased the capacitance of the readout board. The results in table 5.1 show that the largest increase in noise is due to the connection to the bond pad connection, which represents a non-negotiable component without which the detector could not be used. The second largest noise contribution is observed with the introduction of the switch, especially when channels one and four are switched on. This indicates that the long traces on the edges of the board, marked in figure 5.6, act as antennas and most likely pick up more electromagnetic signals from the surrounding than the shorter traces connecting the channels two and three. Overall, the board assembly shows only a small noise contribution around approximately 20 mV at a maximum due to the components and the diode mounted on the board.

Table 5.1: Noise contributions of electronic components on the readout board.

	min in mV	**max** in mV	**Diff** in mV
1) amp only	1.16	1.77	0.61
2) amp plus cable	3.05	4.46	1.46
3) board + SMA connector	5.3	8.6	3.3
4) 3) plus cable to bond pad	5.5	19.7	14.2
5) 4) plus PT1000	5.7	17.0	11.3
6.1) 3) plus switch (all ch. off)	5.5	16.6	11.1
6.2) 3) plus switch (all ch. on)	7.7	27.4	19.7
6.3) 3) plus switch (1 and 4 on)	5.9	20.1	14.2
6.4) 3) plus switch (2 and 3 on)	5.5	14.8	9.3
7) 4) plus switch (ch2) plus diode	7.8	15.8	8

5.5 Noise Occupancy Measurement for Local Trigger Level Determination

Although the noise contributions of the individual components of the readout board are small, there are still significant other contributions to the noise of the detector system, such as other electronic devices coupling into the system or the shielding of visible light at the measurement spot. The goal of the measurement described in this section is to determine the lowest trigger level possible at which the noise occupancy becomes negligible. However, at the same time a trigger level that is set too high will reduce efficiency by cutting out a signal providing valuable information resulting in an optimization problem: A trigger level has to be determined that delivers as much information about true signals as possible while at the same time being high enough to not record excessive noise that would dominate the signal when recording a fixed number of waveforms for each measurement. For that purpose a preliminary qualitative analysis allowed to determine a trigger level of around 50 mV as a good first estimate. In a second step, the trigger was set just below that, namely at 40 mV while the number of waveform acquisitions was recorded over 30 s twice to determine the noise occupancy. The measurement was performed with and without biasing the sensor with 50 V. The noise occupancies for the two trigger levels under investigation, measured with and without high voltage, can be found in table 5.2.

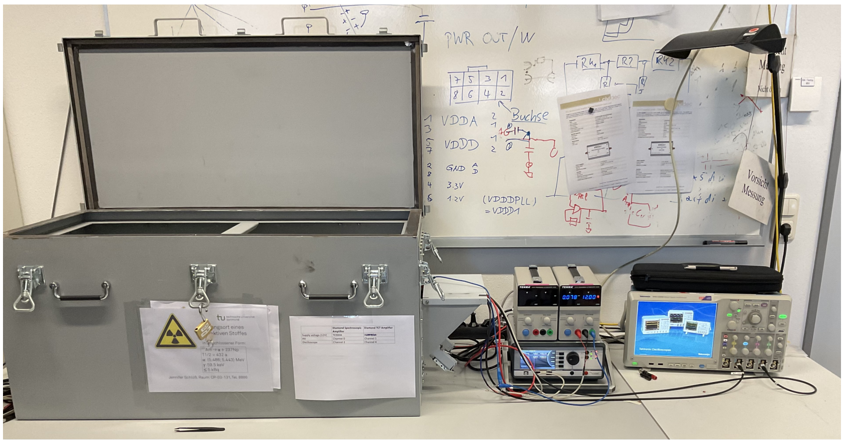

Figure 5.8: Laboratory environment for the preliminary detector characterization with the metal box that serves as a Faradays cage, power supplies, the amplifiers, and the oscolliscope for the readout.

The following noise occupancy measurement, as well as the first noise measurements, was conducted in a light tight metal box that is displayed in figure 5.8 with a cable outlet that is filled with copper beads forming a Faraday cage. The decrease in noise occupancy with the application of a bias voltage of 50 V, compared to the noise occupancy measurement without bias voltage, can be explained by the capacitance development under bias voltage application. Due to the electric field inside the sensor, the free charge carriers are removed from the space charge region, decreasing the capacitance. This results in a decrease of the noise signal. As a consequence of this measurement, the trigger level under ideal conditions has to be set to 50 mV, and has to be adapted accordingly if the noise increases at a local measurement environment.

Table 5.2: Noise occupancy determination with and without bias voltage.

trigger level	**n.o. without bias voltage**	**n.o. with 50 V bias voltage**
40 mV	$(10.5 \pm 1.5)/\mathrm{s}$	$(1.5 \pm 0.7)/\mathrm{s}$
45 mV	$(1.1 \pm 0.3)/\mathrm{s}$	$(0.17 \pm 0.03)/\mathrm{s}$

6 Neutron Keg Measurements - First Proof of Principle

The TU Dortmund University owns a neutron source that is explained in this chapter along with neutron activation measurements to investigate the neutron flux of the source. Finally, first neutron measurements with the first prototype developed for this work are described at the end of this chapter.

6.1 Neutron source at TU Dortmund University

Figure 6.1 shows a schematic drawing of the TU Dortmund's neutron source. It contains a RaBe source at it's centre with an activity of 100 kBq at the centre of the source. The Ra isotope used is ^{226}Ra , which undergoes an α decay with a half life of (1577 ± 9) yr [54]. The ^{226}Ra decay chain includes the following α and β^- decays:

$$\begin{aligned}
{}^{226}_{88}\mathrm{Ra} &\to {}^{222}_{86}\mathrm{Rn} + \alpha \quad (T_{1/2} \approx 1600\,\mathrm{year},\ E_\alpha = 4.87\,\mathrm{MeV}) \\
{}^{222}_{86}\mathrm{Rn} &\to {}^{218}_{84}\mathrm{Po} + \alpha \quad (T_{1/2} = 3.82\,\mathrm{d},\ E_\alpha = 5.59\,\mathrm{MeV}) \\
{}^{218}_{84}\mathrm{Po} &\to {}^{214}_{82}\mathrm{Pb} + \alpha \quad (T_{1/2} = 3.10\,\mathrm{min},\ E_\alpha = 6.12\,\mathrm{MeV}) \\
{}^{214}_{82}\mathrm{Pb} &\to {}^{214}_{83}\mathrm{Bi} + \beta^- \quad (T_{1/2} = 26.8\,\mathrm{minute},\ E_{\beta^-}^{\mathrm{max}} = 1.02\,\mathrm{MeV}) \\
{}^{214}_{83}\mathrm{Bi} &\to {}^{214}_{84}\mathrm{Po} + \beta^- \quad (T_{1/2} = 19.9\,\mathrm{min},\ E_{\beta^-}^{\mathrm{max}} = 3.27\,\mathrm{MeV}) \\
{}^{214}_{84}\mathrm{Po} &\to {}^{210}_{82}\mathrm{Pb} + \alpha \quad (T_{1/2} = 164\,\mu\mathrm{s},\ E_\alpha = 7.69\,\mathrm{MeV}) \\
{}^{210}_{82}\mathrm{Pb} &\to {}^{210}_{83}\mathrm{Bi} + \beta^- \quad (T_{1/2} = 22.3\,\mathrm{yr},\ E_{\beta^-}^{\mathrm{max}} = 0.064\,\mathrm{MeV}) \\
{}^{210}_{83}\mathrm{Bi} &\to {}^{210}_{84}\mathrm{Po} + \beta^- \quad (T_{1/2} = 5.01\,\mathrm{d},\ E_{\beta^-}^{\mathrm{max}} = 1.16\,\mathrm{MeV}) \\
{}^{210}_{84}\mathrm{Po} &\to {}^{206}_{82}\mathrm{Pb} + \alpha \quad (T_{1/2} = 138\,\mathrm{d},\ E_\alpha = 5.41\,\mathrm{MeV})
\end{aligned}$$

The neutron production reaction happening in the centre of the source is as follows:

$$^{9}\mathrm{Be} + \alpha \to {}^{12}\mathrm{C} + \mathrm{n} + \gamma(4.44\,\mathrm{MeV}) \quad .$$

The average neutron energy of the RaBe n,α reaction is 3.6 MeV with a maximum neutron energy of 13.6 MeV. To reduce the maximum neutron energies, the neutron source is shielded by a spherical lead shield with a 4 cm diameter. The underlying physical principle is described in section 3.2.

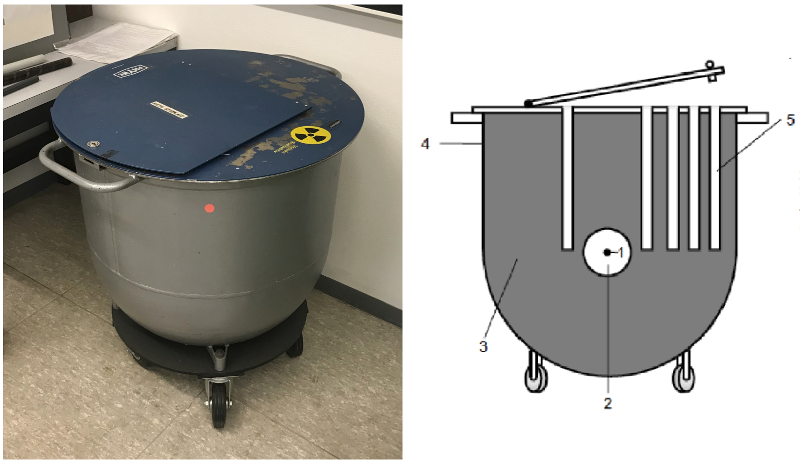

Figure 6.1: Neutron source with a graphical sketch of the cross-section of the source displaying the location of the source and the drill hole placement for experimentation.

The purpose of the neutron source in the university laboratory course is to perform activation measurements with thermal neutrons. Therefore, the neutrons are moderated to thermal energy levels by a paraffin filling in the keg-shaped structure. Therefore, several drill holes are located in the paraffin filling around the centre of the keg for experimentation. The drill holes are located at different distances to the centre of the keg where the neutron source is placed as it can be seen in figure 6.1.

6.2 Activation Measurements

The neutron flux, according to the data sheet of the source, should decrease with the distance to the centre, but the data sheet does not contain quantitative specification of the neutron flux decrease over distance. Therefore a first measurement was performed to get an estimate of the relative neutron flux development with the distance. For that purpose, the activation of a ^{51}Vn target placed at various positions relative to the neutron source centre was measured. When exposed to thermal neutrons ^{51}Vn is activated and subsequently undergoes a β^- decay shown in equation 6.1 with a half life of 3.75 min. As the neutron activation cross-section for the ^{51}Vn target is not known, the measurement results show the relative neutron flux decay in the keg with increasing distance to the neutron source.

$$^{51}\mathrm{Vn} + n \rightarrow \mathrm{V}^{52} \tag{6.1}$$

$$^{52}\mathrm{Vn} \rightarrow {}^{52}\mathrm{Cr} + e^{-} + \bar{\nu}_e \tag{6.2}$$

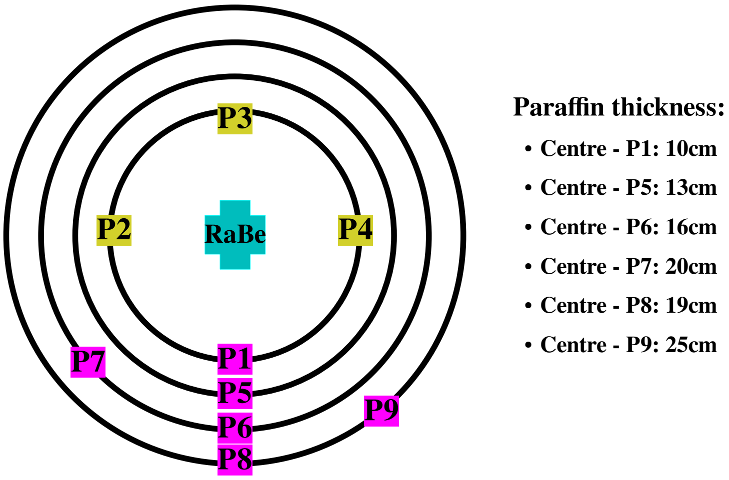

Figure 6.2: Graphical sketch of the measurement spot distribution inside the keg. The positions in pink mark the measurement locations for the activation measurement performed.

The target is subsequently irradiated in the measurement spots shown in figure 6.2 for 20 min. After each irradiation with thermal neutrons, the electrons emitted by the activated target are counted by a proportional counter for 40 min. The counts in the proportional counter were summed over 20 s, showing the typical exponential decay displayed in figure 6.3. The initial activation (A_0) for each measurement spot could be determined with the help of a decreasing exponential fit to the data. The schematic representation of the measurement spot locations in Figure 6.2 illustrates the paraffin thickness between the designated measurement spots and the centre of the keg containing the neutron source.

It is important that despite having the same distance to the neutron source, the amount of paraffin between position five and seven for example is different: In front of position five is the drill hole for position one that does not contain any moderating material.

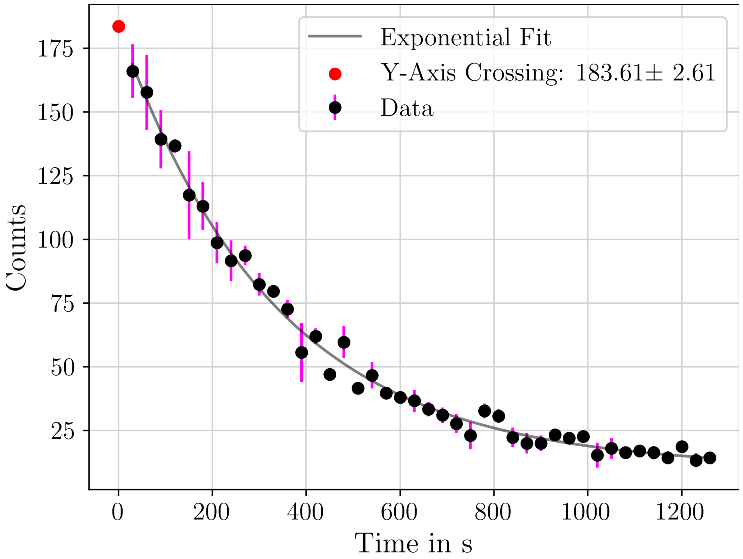

Figure 6.3: Exponential decay of the activation of V^{51} for 20 min at measurement position 2 in the neutron keg.

The plot of the initial activation (A_0), shown in figure 6.4, as a function of the paraffin thickness between the measurement spot, indicates an exponential decrease of the neutron flux with increasing distance to the source as expected from the data sheet descriptions. The neutron flux reaches a maximum for the measurement locations closest to the neutron source. Consequently, measurement spot one is chosen for the first neutron measurements with the detector prototype.

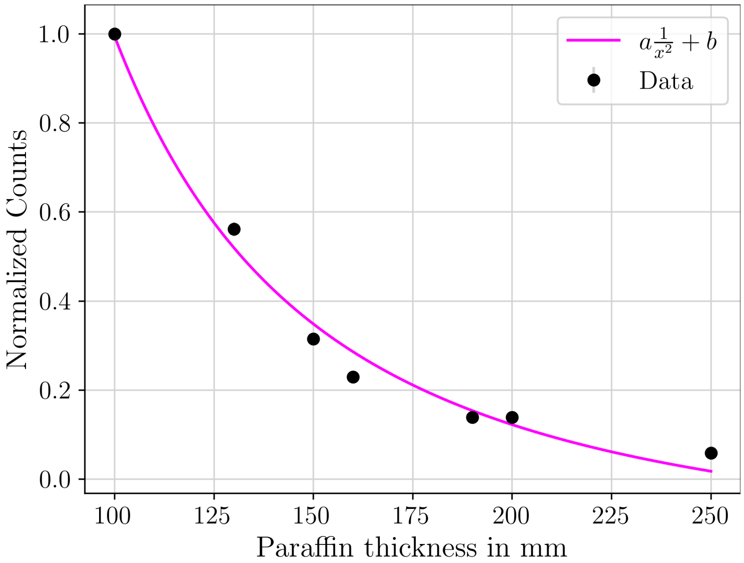

Figure 6.4: Initial activation as a function of paraffin thickness. A $\frac{1}{x^2}$ fit is used to describe the decay of the activation with increasing paraffin thickness between the centre and the measurement location.

6.3 Local Noise Investigation

Before operating the detector, a noise occupancy measurement was performed in the neutron keg environment. For that purpose, the detector was placed in a light-tight environment outside the keg, and the trigger level at the oscilloscope was set to 50 mV which is the same level as in the laboratory environment. However, the noise occupancy was too high due to the lack of the Faraday cage, which was used to perform the initial noise occupancy measurements in the laboratory. As a consequence, the trigger level was subsequently raised up to 84 mV so that the noise occupancy measured with the detector outside the keg was significantly lower.
After the noise occupancy measurement outside the keg, the undepleted sensor was lowered into the drill hole in position one, closest to the centre. An observation of the amplifier output on the oscilloscope showed that the amplifier received an input even when the sensor was not yet inside the measurement location, but the traces of the contact pads at the lowest end of the readout board were already inside the keg. Electrical grounding of the outer shielding of the neutron keg stopped this phenomenon, delivering the explanation at the same time that the neutron keg, with its metal shielding on the outside, functions as an antenna for electromagnetic waves inside the experimental room.

6.4 Signal Analysis - Shaping Amplifier”

The output signal from the shaping amplifier is fed into a Tektronix mixed-signal oscilloscope model MSO5204b [55]. The input resistance is set to 50 Ω to prevent signal reflection at the oscilloscope’s input. The incoming data is sampled with a preset sampling frequency of 5 GS/s. Over 2 µs, time and voltage data pairs are sampled and stored in a .csv file for each waveform. For an initial investigation of the signal structure, all waveforms of a measurement are illustrated in one plot. An exemplary plot for the first measurement can be found in figure 6.5. The characteristic Gaussian pulse shape, as described by CIVIDEC [49], is clearly recognizable for the majority of the sampled waveforms. The figure also displays waveforms that significantly deviate from the expected pulse shape. These waveforms are associated with electronic switching processes present in the experimental room, as described in section 5.4. The post-processing of the raw datasets includes two steps:

1. Electromagnetic noise reduction
2. Signal smoothing to reduce small noise fluctuations within the signal

6.4.1 1) Electromagnetic Noise Reduction

In the first post-processing step, the local electromagnetic noise signals are separated from the clean signals. For that purpose, several characteristics of the background signals are exploited: they characteristically display significant peaks outside the Region of Interest (ROI), which is defined for this dataset to be located at the centre of the time axis from zero to 15 µs. Waveforms with significant peaks outside of that region or with more than one peak that is identified by the $scipy.signal.find\_peaks$ [56] function, are discarded. Conversely, signal waveforms with one peak inside the ROI with a prominence larger than 0.1 are classified as good.

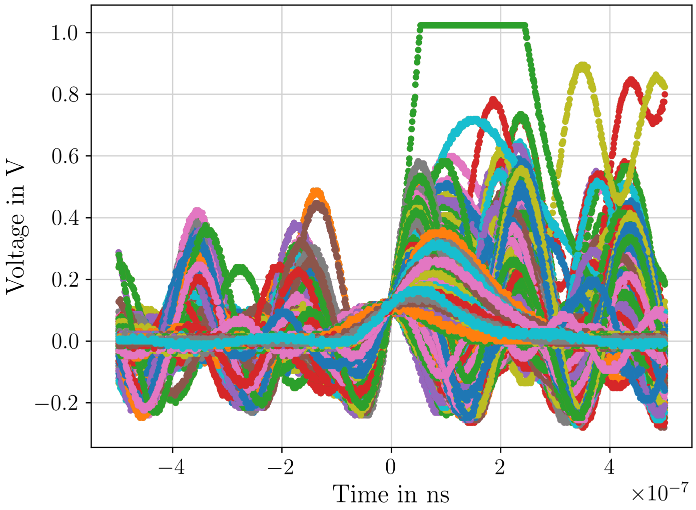

Figure 6.5: Unfiltered waveforms for a dataset taken at the TU Dortmund's neutron source.

6.4.2 2) Signal Smoothing

In the second step, a rolling mean averaging filter is used to process the data. This filter computes the local average of the signal using a sliding window. The window size for the averaging filter was chosen so that it would not significantly influence the peak height while at the same time smoothing smaller noise fluctuations. As a result of this adaptive process, the window size of 15 voltage values is determined. All filtered and smoothed waveforms of one exemplary dataset can be found in figure 6.6. After this filtering process, the maximum values of each waveform classified as "good" are stored in a separate dataset.

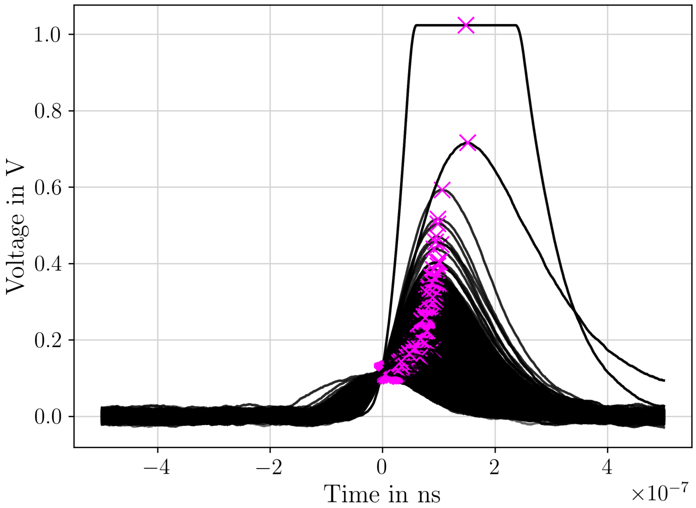

Figure 6.6: Smoothed and filtered waveforms same dataset as in 6.5. The crosses mark the maximum value of the smoothed voltage data that are stored after the processing.

6.5 Proof of Principle

The first measurement campaign is deducted after the local noise investigation and trigger threshold determination, as described in section6.3, are performed. Before each measurement, the noise occupancy is determined to establish the individual trigger level for that measurement day. This was necessary, as the electrical noise inside the laboratory is highly dependent on the amount of active electronic devices present in the circuit. This could vary from day to day. The trigger level was set to 110 mV for the first measurements.
The four different detector setups shown in figure 6.7 are used to measure signals inside the neutron keg. The setups include:

a) Designed to measure the background radiation signal that originates from particles unrelated to neutron converter interaction.

b) Delivers information on the influence of the aluminium carrier plate on the background radiation. The aluminium carrier plate has a thickness of 0.5 mm which sufficiently shields the secondary α-particles from the $^{10}\mathrm{B}(\mathrm{n}\alpha)^{7}\mathrm{Li}$ capture reaction from reaching the sensor and creating a signal.

c) Shows the setup, with the converter facing the backside of the sensor at a minimal distance between the sensor and the converter.

d) Similar to configuration c) with an additional converter facing the front side of the silicon sensor.

The CIVIDEC "CX: spectroscopic amplifier" is used for all measurements, and the following section serves to describe the data processing workflow.

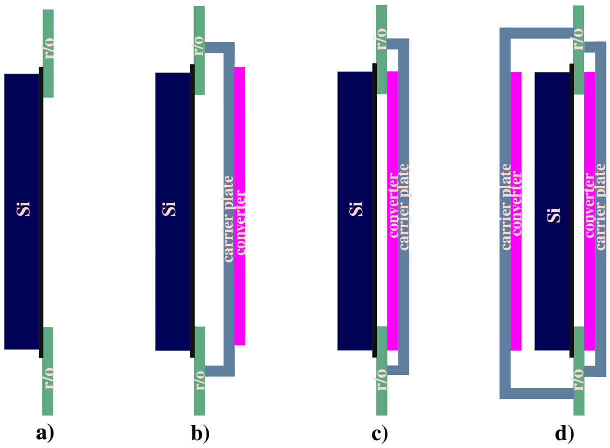

Figure 6.7: Sketches of detector configurations under investigation in the order of the presented measurements **a)** the plain detector, **b)** with the flipped converter, **c)** with the converter facing the sensor's backside, and **d)** with a double converter layout.

6.5.1 Proof of Principle - Influence of the Carrier Plate

In an initial analysis, the measurement results of signals recorded and processed according to section 6.4 are compared for two configurations: one without a converter and one with a converter plate mounted in an orientation where the converter does not face the sensor (flipped converter). The purpose of that measurement is the identification of potential background irradiation introduced by the activation of the aluminum carrier plate.

The histogram of the peak heights normalized to the total number of recorded signals of both measurements is displayed in the upper figure 6.8.

The lower plot shows the difference between the the two measurements, with the histogram without a converter is subtracted from the histogram with the flipped converter. The lower plot also includes an uncertainty band which is calculated bin-wise according to the following equation:

$$\begin{aligned}\sigma_{\text{subtracted}} &= \sqrt{\sigma_{\text{N1}}^2 + \sigma_{\text{N2}}^2} \\ &= \sqrt{\left(\frac{\sqrt{\text{N1}}}{N_1}\right)^2 + \left(\frac{\sqrt{\text{N2}}}{N_2}\right)^2} \quad ,\end{aligned}$$

where N_1 and N_2 are the normalized number of counts for the two measurements. The uncertainty band is calculated for each bin of the histogram, is placed symmetrically around zero, and spans the range of $\pm\sigma_{\text{subtracted}}$.

The histogram plot and the difference plot show that the two histograms cannot be distinguished within the uncertainties. This is due to the aluminum of the carrier plate mounted to the back of the sensor is shielding the α-particles created in the converter that is not facing the sensor. It also shows, that there is no significant shielding of heavy particles that would deposit larger energies inside the sensor. Therefore, it is concluded that the number of heavy charged particles that could stem from neutron interactions with the shielding materials in the measurement positions is negligible.

Additionally, it can be said that the aluminum carrier plate does not introduce a significant additional signal to the measurement.

6.5.2 Proof of Principle - Measurement with a Single Converter to the Back of the Sensor

For the following measurement, the converter carrier plate is mounted to the back of the detector that the converter material is facing the sensors backside at a distance of 3 mm. The converter chosen has a thickness of 2 µm, according to the details provided by the ESS that produced the converter, described in chapter 4, section 4.2.1. Subsequently, a measurement without a converter is performed, and the peak height histograms are compared as described in section6.5.1.

In this plot, the subtraction of the histogram values of the measurement without a converter are subtracted from the measurement with the converter as before. For this measurement, the subtracted values are renormalized to the counts of the measurement without a converter, resulting in the relative difference in normalized counts (RDN). This method highlights the differences between the two histograms with respect to the measurement without the converter.

The RDN is calculated for each histogram bin according to the following formula, where N_1^{norm} and N_2^{norm} are the normalized counts for the measurements with and

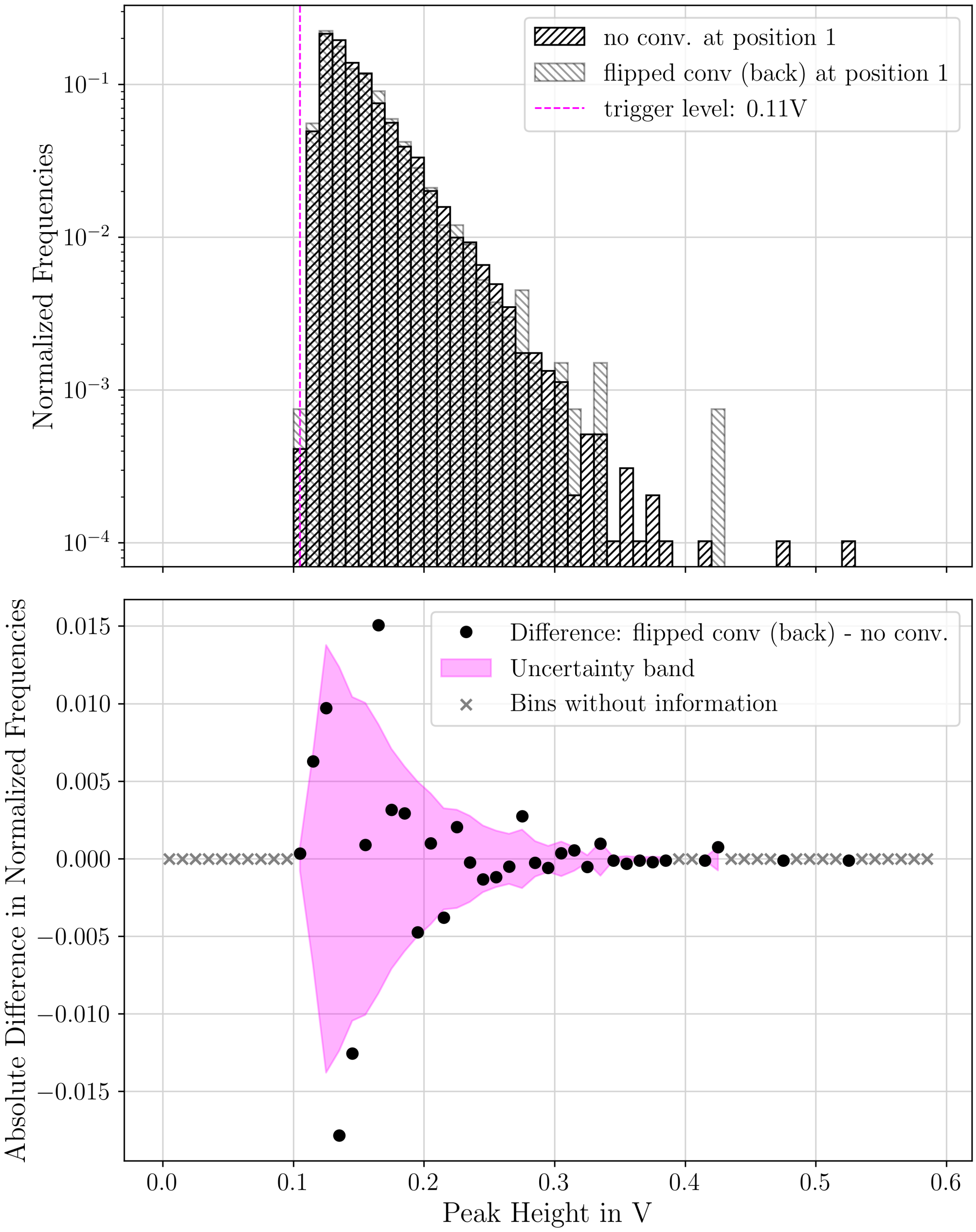

Figure 6.8: Peak height histogram and absolute difference for a measurement with no converter, and with a converter not facing the sensor ("flipped converter).

without the converter mounted from the back:

$$\mathrm{RDN} = \frac{N_2^{\mathrm{norm}} - N_1^{\mathrm{norm}}}{N_1^{\mathrm{norm}}} \tag{6.3}$$

$$= \frac{\frac{N_2}{\sum N_2} - \frac{N_1}{\sum N_1}}{\frac{N_1}{\sum N_1}} \quad . \tag{6.4}$$

The plot of the subtraction of the two histograms in the lower plot of figure 6.8 shows the RDN with an uncertainty band. The uncertainty for each bin is described by the Gaussian uncertainty propagation of the Poisson uncertainty of each bin:

$$\sigma_{\mathrm{subtracted}}(i) = \sqrt{\left(\frac{\sigma_{\mathrm{N2}}(i)}{\mathrm{N1}_{\mathrm{norm}}(i)}\right)^2 + \left(\frac{\mathrm{N2}_{\mathrm{norm}}(i) \cdot \sigma_{\mathrm{N1}}(i)}{\mathrm{N1}_{\mathrm{norm}}(i)^2}\right)^2} \tag{6.5}$$

The uncertainties (σ_{N1} and σ_{N2}) in equation 6.5 describe the relative Poisson uncertainty ($\frac{1}{\sqrt{\mathrm{N1}}}$, and $\frac{1}{\sqrt{\mathrm{N2}}}$ respectively). The uncertainty band in the plots of the RDN values is marked between $\pm\sigma_{\mathrm{subtracted}}(i)$ around zero. To avoid division by zero, only entries that contain at least one signal are recorded. The other bins are marked with grey crosses in the plot, as there is not enough information recorded to obtain physically relevant information.

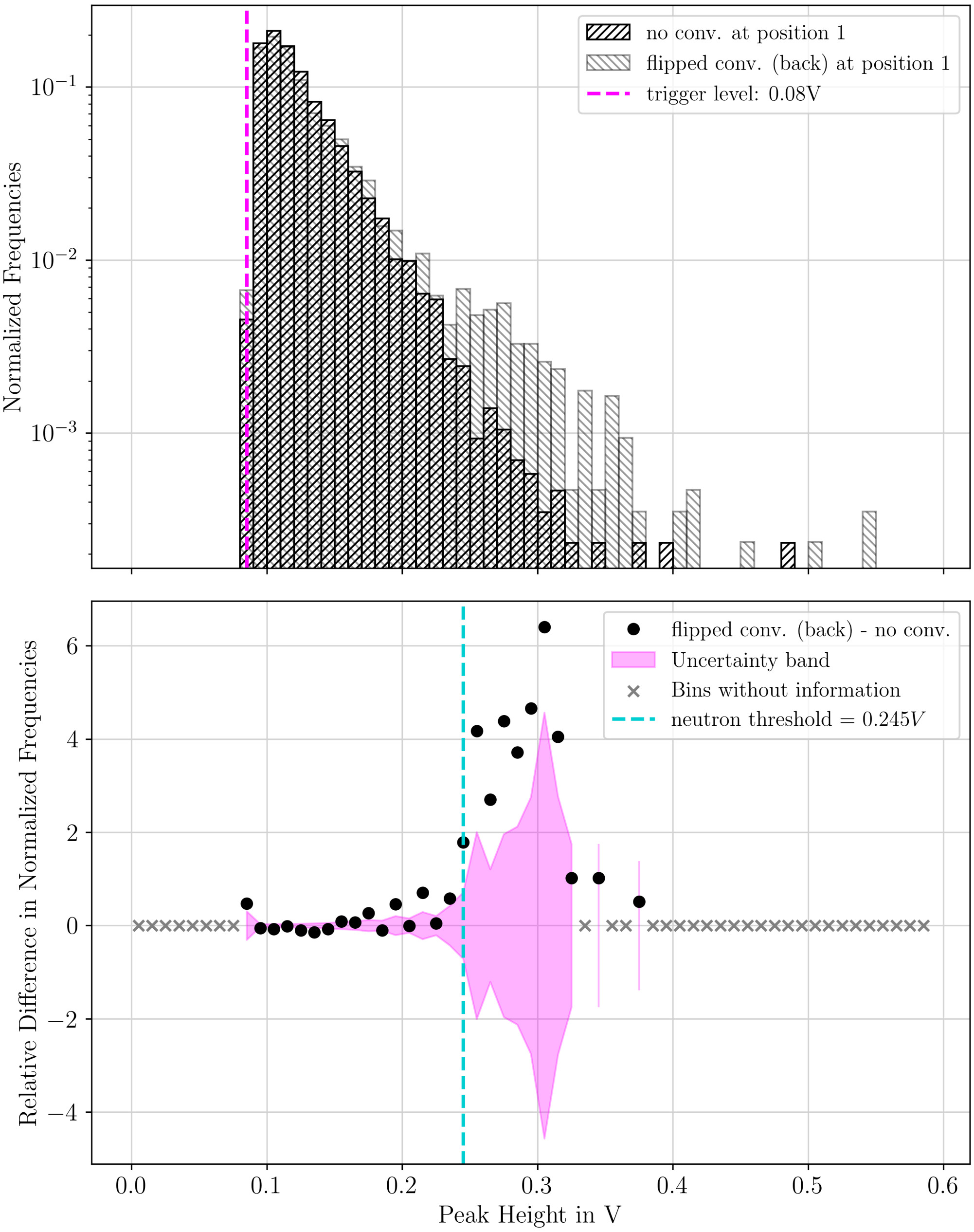

Figure 6.9: Peak height histogram for measurements without and with a 2 µm ^{10}B enriched B_4C neutron converter mounted from the back of the sensor.

The peak height histograms in figure 6.9 indicate that the dataset taken with the neutron converter contains more entries with peak heights above $\approx 200\,\mathrm{mV}$. This can be explained by the α-particles from the ^{10}B neutron capture reaction depositing larger amounts of energy inside the silicon due to their comparably high LET. Therefore, the first conclusion can be made, which is that the detector setup with the converter facing the back of the sensor detects neutrons.
The background radiation inside the neutron keg is estimated to be significant due to numerous possible nuclear reactions of the higher-energy neutrons from the source with the surrounding materials, even though the quantitative information about the spectrum is not available. As a first approximation, the entries above $\approx 200\,\mathrm{mV}$ are considered to predominantly originate from neutron interactions with the converter.

6.5.3 Neutron Threshold

To determine the threshold voltage above which neutron contributions to the signal dominate, the first bin centre with an RDN larger than one and a value larger than 200 mV is marked as the neutron threshold in Figure 6.9. Since the RDN represents the ratio of signal to background, an RDN greater than one indicates that the signal exceeds the background in this region. The threshold voltage of 200 mvolt is qualitatively chosen after comparison of the peak height histograms, and serves as a first estimate. The The trigger level dependency of this threshold is investigated in the following measurement.

6.6 Trigger Level dependency of the Neutron Threshold and Effect on Neutron Purity

For the following investigation, the RDN measurements for different trigger levels are compared. The respective neutron threshold is determined as described in 6.5.2. The uncertainty of that value is estimated as ± one bin width, which is 10 mV. Three datasets with ten thousand raw waveforms each were taken and processed as previously described for a trigger level of 80 mV, while the measurement duration for higher trigger levels increased significantly, only two datasets were taken for a trigger level of 110 mV, and only one dataset was taken for 200 and 240 mV. A background measurement without a converter is performed for each trigger level. For the measurements with multiple datasets, the mean neutron threshold is calculated, and is displayed in figure 6.10. The plot shows that the trigger level has an influence on the neutron threshold, and that the neutron threshold has to be adapted according to the trigger level.

In a next step, it is investigated whether a higher trigger threshold has an influence on the purity of the dataset. The purity describes the proportion of neutron-associated signals (N_{neutrons} in equation 6.6), in the total data set (N_{total} in equation 6.6), and is determined by the sum over the bins above the threshold voltage.
The computation of the purity, and its uncertainty, with the Poisson uncertainty propagation is performed after the following equation:

$$\text{purity} = \frac{N_{\text{neutrons}}}{N_{\text{total}}} \tag{6.6}$$

$$\begin{aligned}\sigma_p &= p \times \sqrt{\left(\frac{\sigma_{N_{\text{neutrons}}}}{N_{\text{neutrons}}}\right)^2 + \left(\frac{\sigma_{N_{\text{total}}}}{N_{\text{total}}}\right)^2} \\ &= \frac{N_{\text{neutrons}}}{N_{\text{total}}} \times \sqrt{\left(\frac{\sqrt{N_{\text{neutrons}}}}{N_{\text{neutrons}}}\right)^2 + \left(\frac{\sqrt{N_{\text{total}}}}{N_{\text{total}}}\right)^2} \;. \end{aligned} \tag{6.7}$$

The results of the purity investigations, shown in figure 6.10, demonstrate that with higher trigger levels, the proportion of neutron associated signals becomes bigger, and that the measurement time at lower trigger levels is driven by non neutron signals.

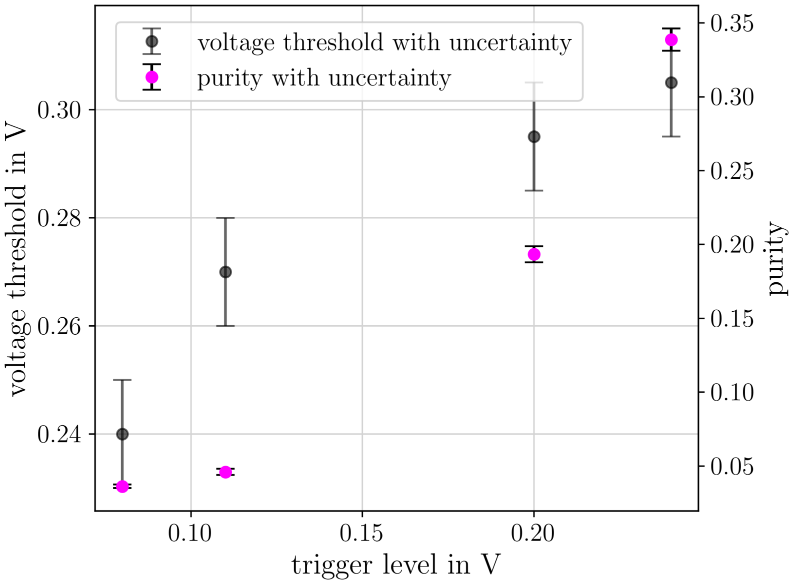

Figure 6.10: Trigger level dependency of the threshold voltage and the purity. The datasets are all taken with a single converter detector configuration.

6.7 Distance Measurement

The fact, that the neutron flux decreases with the increase of paraffin between the source and the measurement point is demonstrated by the activation measurement described in section 6.2. To verify that this trend can be detected by the first prototype, 4 consecutive measurements are conducted at positions 1, 5, 6, and 8 inside the neutron keg. Subsequently, the purity of each data set is calculated according to 6.6, together with the Poisson uncertainty propagation. The individual neutron threshold for each data set is determined with the help of the RDN calculation for each dataset described in section 6.5.3.

Additionally, the purity is divided by the relative measurement time. The relative measurement time is the individual measurement time divided by the measurement duration of a measurement performed closest to the neutron source with the same sampling frequency.

This relative measurement time index is applied, because the dataset for position six was recorded with an optimized sampling frequency, which ultimately led to a three times faster data acquisition. The measurements at the other positions were all performed with the maximum sampling frequency that had a negative influence on the data acquisition speed.

Figure 6.11 shows the normalized purity as a function of paraffin thickness between the measurement spot and the neutron source. The plot shows a trend in neutron count-rates decreasing over the distance, comparable to the relative decrease in neutron flux determined with the activation measurement in section 6.2. The measurement durations increases significantly with the distance to the source at the centre of the keg while a constant number of raw waveforms is recorded. For each measurement spot only one measurement is taken. This trend plot should not serve as a quantitative analysis of the relative neutron flux decrease, as there are multiple uncertainties not considered in this first estimate measurement. However, it could well describe the trend of decreasing neutron flux with increasing distance to the source.

In both measurements, only the statistical uncertainties are taken into account. The systematic uncertainties, such as the efficiency of the Geiger-Müller-Counter used in the activation measurement, as well as the detection efficiency of the silicon detector are not considered.

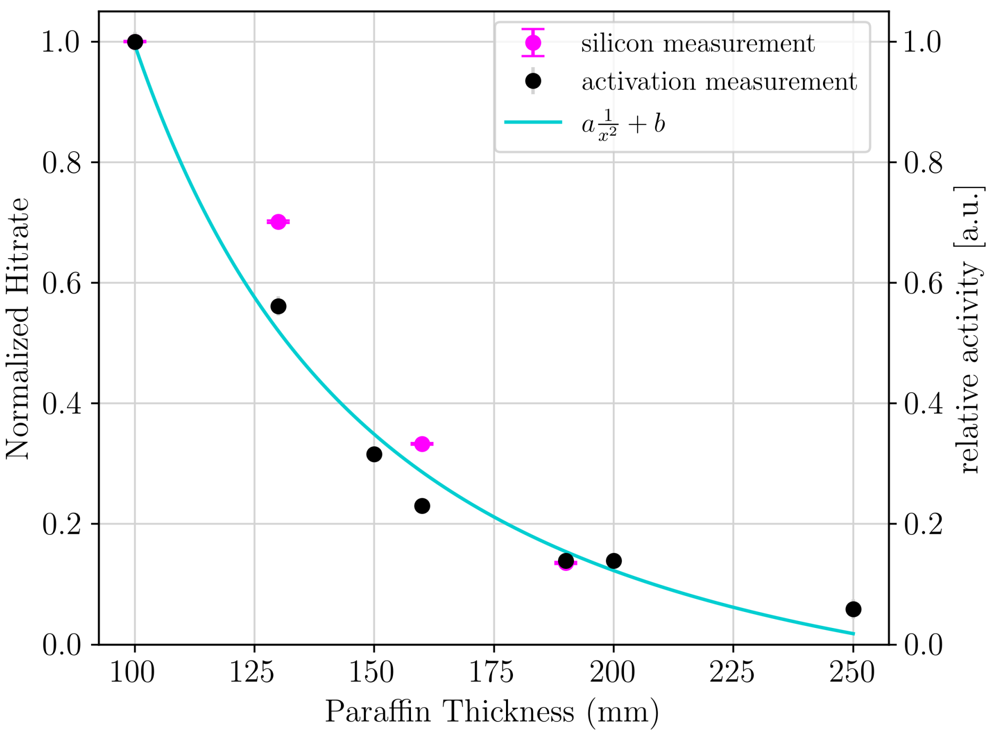

Figure 6.11: Relative purity normalized to the relative measurement time in pink, and the relative neutron flux determined by the activation measurement described in section 6.2 in black. The $\frac{1}{x^2}$ function is fitted to the activation measurement data.

6.8 Detection Efficiency Investigations

The design of the readout board allows the investigation of alternative detector layouts. In this section, firstly a thicker converter, and its influence on the detection efficiency, is investigated, followed by a detector setup with two converters facing the front and the back of the sensor.

6.8.1 Increased Converter Thickness

Simulations performed in theses in our working group ([45], [43]), and also by other groups ([7]), indicate that the conversion efficiency of a ^{10}B enriched B_4C neutron converter increases with the thickness of the absorber. However, the amount of α-particles escaping the converter is limited by their projected range in boron carbide due to their high LET. Logically, an optimal thickness can be defined at which the amount of α-particles with large enough energies leaving the converter is at a maximum. This thickness was determined by multiple working groups ([47], [45], [43]) to be around 2 µm.
Simulation results indicate that the detection efficiency decreases for thicker converter layers, as the secondary α-particles have to travel larger distances inside of the converter leading to an energy loss, and a subsequent decrease in signal strength. To investigate whether the detector can resolve that decrease in detection efficiency, the thickest converter with 4.24 µm is used for an additional measurement campaign. The trigger level for this measurement is 200 mV.
Figure 6.12 shows the difference between measurements using a 2 µm and a 4 µm thick converter plate. The neutron threshold, determined according to the procedure described in section 6.5.3, lies for both measurements at 295 mV. This is a first hint that the thicker converter does not have a significant influence on the energy spectrum of the α-particles leaving the sensor. If that was the case, the neutron threshold would have shifted towards smaller peak heights as α-particles with reduced energies would deposit less energy inside the silicon sensor.

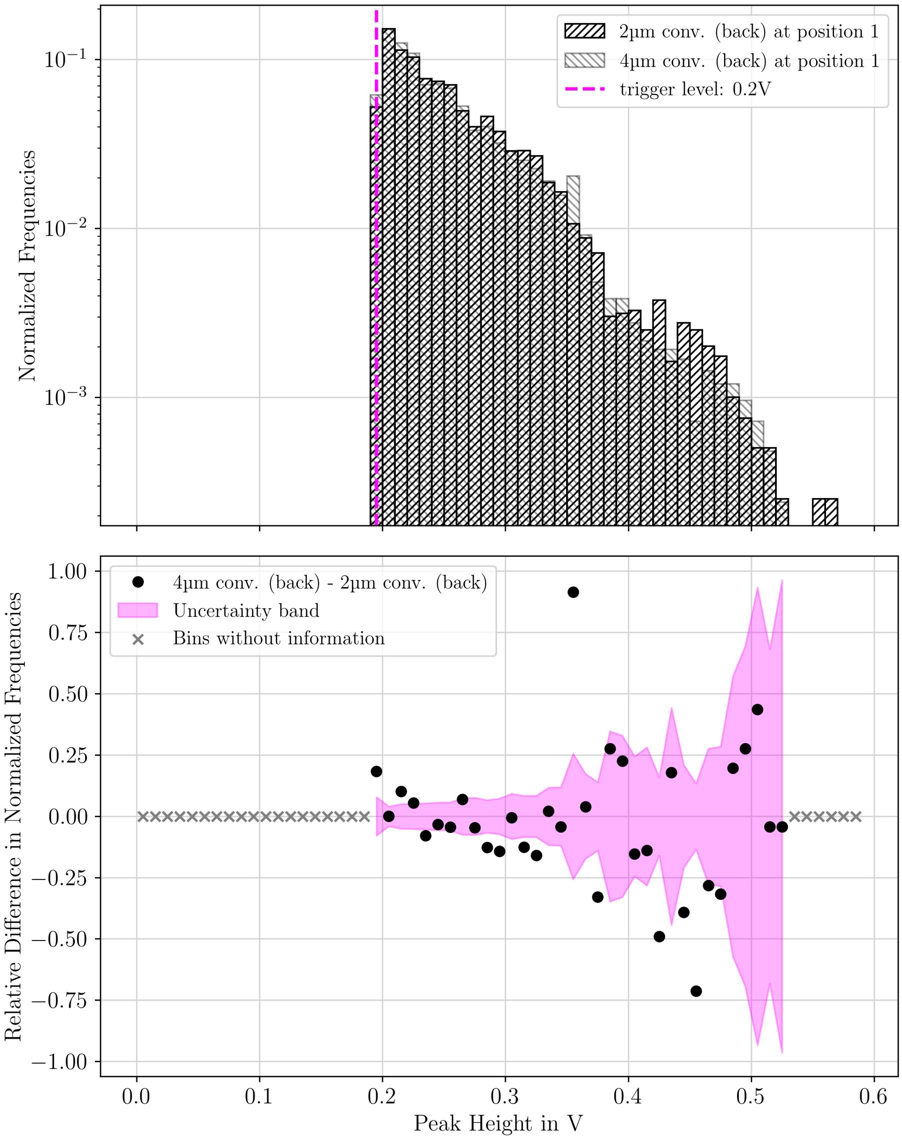

Figure 6.12: Peak height histogram and RDN values with neutron threshold for a converter thickness of 4 µm, and 2 µm, measured with a trigger level of 200 mV.

The plot of the RDN calculation for the two measurements in the lower plot of figure 6.12, shows only very small deviations that mostly lay within the uncertainty band, or very close to it. The purity value for this measurement, calculated according to equation 6.6, is 0.172 ± 0.005. It lies slightly below the purity of the measurement with the 2 µm converter which is at 0.193 ± 0.005. The difference in purity can be regarded as a hint that a thicker converter decreases the neutron detection efficiency of the detector. This trend goes well together with the obtained simulation results shown in chapter 4, section 4.1. At this point, it should be noted that there are a multiple uncertainties contributing to the measurement results. Unfortunately, the exact composition of the background irradiation inside the keg is undefined, which makes further quantitative analysis impossible.

In a recently started master's thesis, the neutron source is simulated with the aim to close that knowledge gap. Further, the local noise contributions can be significant at the measurement location, leading to a lot of signals that have to be discarded in the post-processing, which ultimately leads to a decrease in statistics. Paired with the comparably low activity of the radium beryllium neutron source of 100 kBq, and the low conversion efficiency, the overall neutron signal component of the recorded signals can be regarded as very low, which further increases the uncertainties in quantitative analyses.

6.8.2 Double Converter Configuration

The aforementioned mentioned detection efficiency simulations indicate that a double converter detector layout with two converters, one facing the front, and the other one facing the back of the sensor, can increase the neutron detection efficiency from $(1.4 \pm 0.1)\,\%$ up to $(4.1 \pm 0.1)\,\%$.

For that purpose, detector configuration d) shown in figure 6.7 is investigated, with the 2 µm converter mounted from the back and another one with also 2 µm was mounted from the front. Two measurements are performed: One with a trigger threshold of 80 mV, and another one with a trigger threshold of 200 mV. Both measurements are performed at position two.

For a later comparison, the two measurements are repeated in the same measurement position with a single converter configuration, mounted from the back. The neutron threshold determination for both measurements is performed analogue to the process described in section 6.5.3. The neutron threshold for 80 mV lies at 235 mV. For 200 mV, a neutron threshold of 305 mV is determined. Both lie within the uncertainties for the neutron thresholds calculated for single converter detector configurations, shown in section 6.6. Figure 6.13 shows the histogram of the measurements with the lower trigger threshold, for the double and single converter configuration, together with the RDN calculation. It becomes clear that there is no significant difference between the two data sets above the neutron threshold voltage.

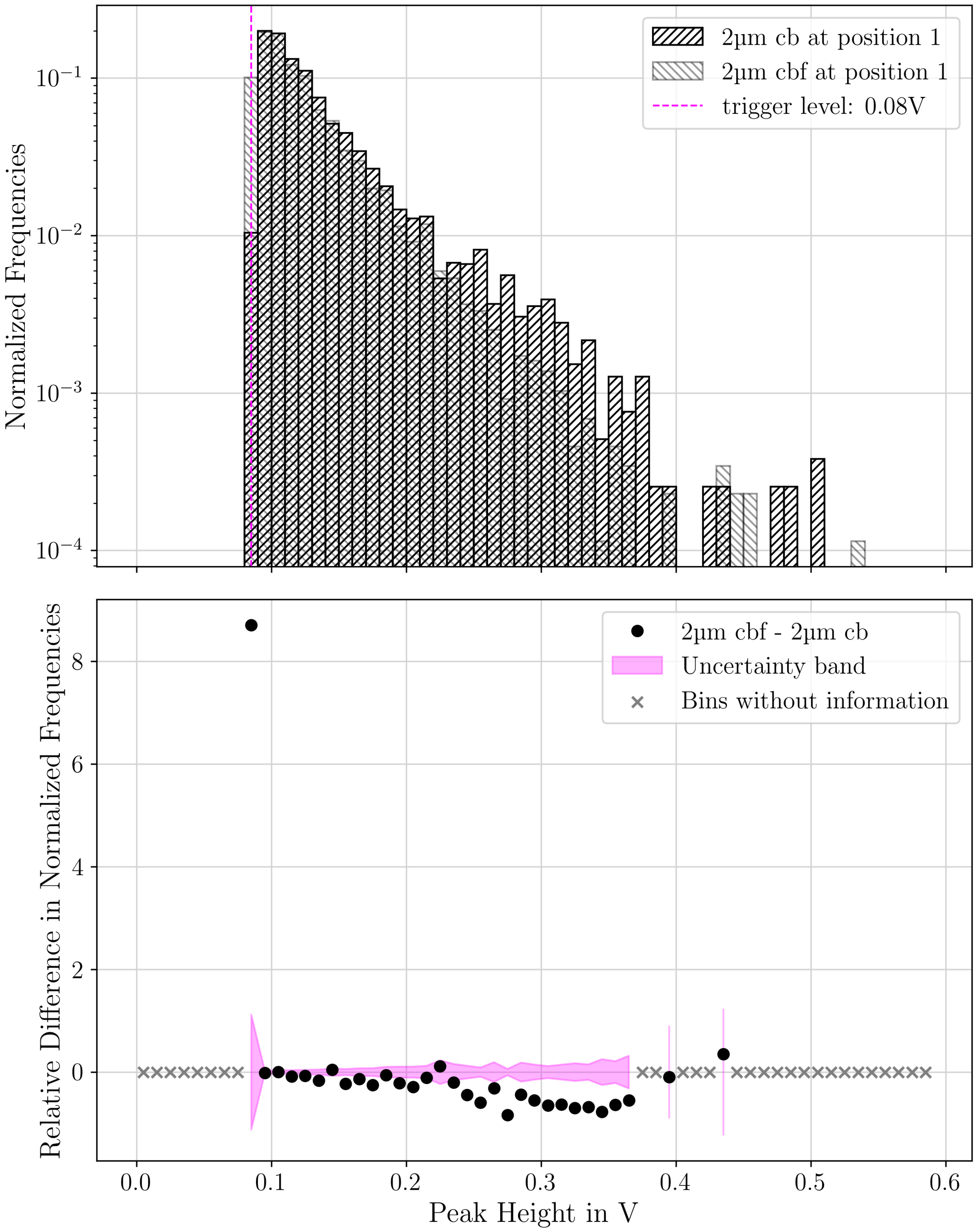

Figure 6.13: Peak height histogram and RDN for a single converter from the back (cb 2µm) and double converter configuration (cbf 2µm).

The determined neutron thresholds are used to calculate the measured purity according to equation 6.6.

The measured purity for the dataset taken with the lower threshold voltage, is 0.021 ± 0.001 for the double converter measurement. With that, it is smaller than the purity of the single converter measurement which is 0.047 ± 0.001. This trend is also observed for the higher trigger threshold: The purity values are 0.097 ± 0.006 for the double converter, and 0.205 ± 0.005 for the single converter configuration.

One possible explanation for this observation could be the decreased energy of the secondary α-particles originating from the converter from the front. The converter mounted onto the readout board from the front of the sensor has to have a distance of (5.00 ± 0.05) mm to the sensor due to the wire bond connection elevating from the surface of the readout board onto the contact pad. In comparison with the distance between the backside converter, which is only at a 3 mm distance to the sensor. This represents a significant increase in distance. Especially with respect to the projected range of the secondary α-particles . According to the Alpha Stopping Power And Range table (ASTAR) data base [57] by the National Institute of Standard and Technologies (NIST), the projected range for the two possible α-particle energies are $9.001 \times 10^{-4}\,\mathrm{g/cm^2}$ for 1.47 MeV and $1.099 \times 10^{-3}\,\mathrm{g/cm^2}$ respectively for the 1.78 MeV α-particles . Divided by the density of dry air at room temperature, this results into projected ranges of the α-particles of 0.75 cm, and 0.91 cm. The projected range of the secondary α-particles is the expected penetration depth along their initial flight direction, calculated without considering deviations due to scattering.

Additionally, the metallization described in chapter 5, adds another layer that reduces the energy of impinging α-particles further.

The combination of the limited range of the α-particles of the ^{10}B neutron capture reaction together with the metallization of the sensor reduces the energy of the α-particles reaching the sensor from the front converter, so that their signal cannot be distinguished from the signal created by background radiation inside the neutron keg. This ultimately causes a decrease in the purity of the sample, meaning a decreased neutron discrimination from background radiation.

The histogram comparison between a single and a double converter configuration for the higher trigger level of 200 mV, shown in figure 6.14 also supports that conclusion.

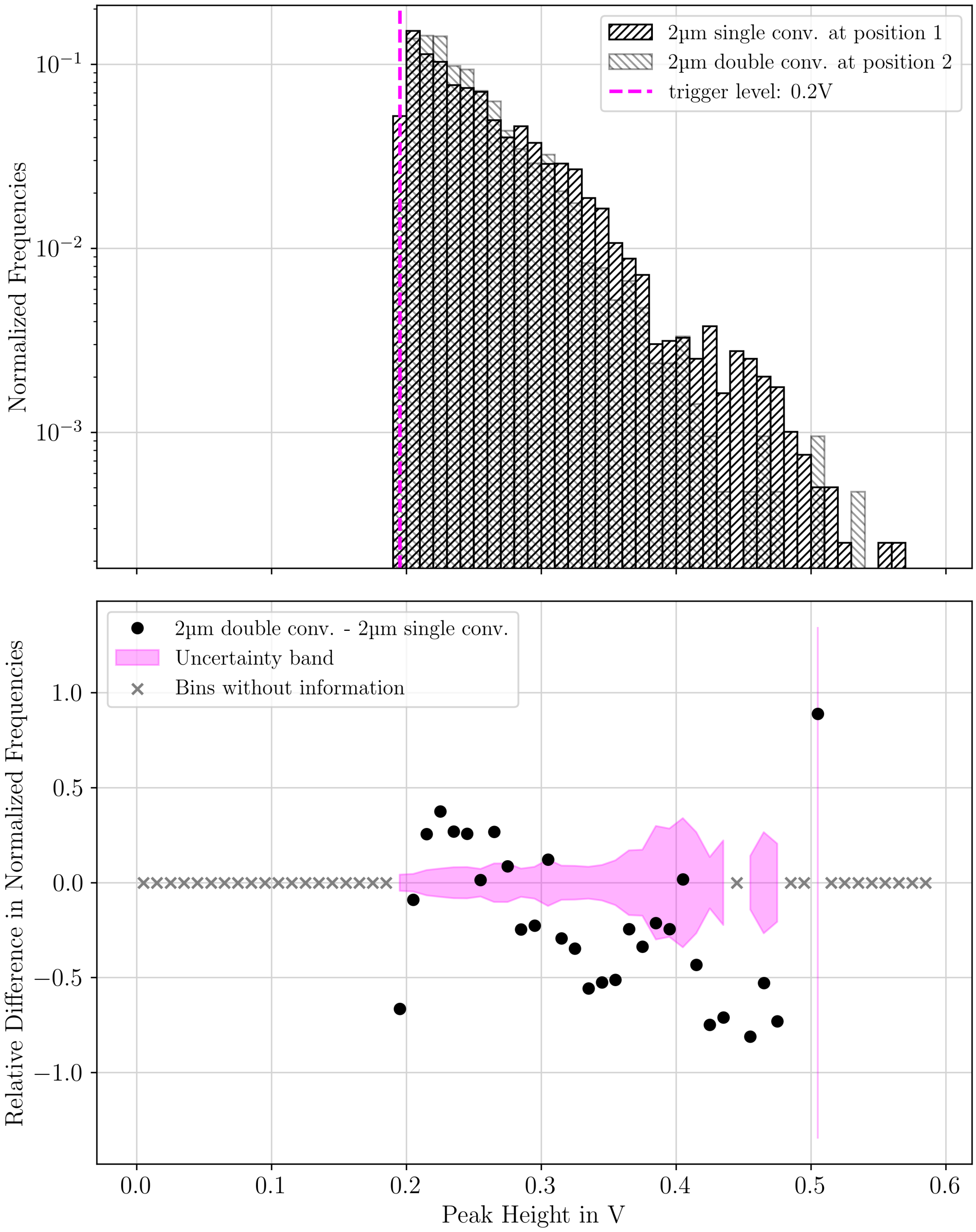

Figure 6.14: Peak height histogram and RDN for a single converter from the back (cb 2µm) and double converter configuration (cbf 2µm) with a higher trigger level of 200 mV.

In both measurements an identical number of 10000 raw waveforms was recorded. The deduction of the single converter measurement from the double converter measurement results shows more hits with peak heights below the determined neutron threshold of 305 mV for the double converter configuration. The single converter measurement shows more signals with peak heights above the threshold in comparison to the double converter layout. As discussed in section 6.5.1, this effect is not due to a shielding effect of the carrier plate, as a single converter plate did not display a shielding effect.

6.9 Conclusion of the Measurement Campaign

The results presented in this chapter prove that neutron detection with the developed detector and the developed read out system is possible. The histograms presented for the different detector configurations with neutron converters display a clear difference in comparison to the histograms taken without a converter.

The neutron component of the measured signals is very small. This can be once explained by the low detection efficiency of the detector, but also a theoretical neutron flux calculation for the measurement position one shows, that the estimated neutron flux through the detector is comparably low.

An estimation calculation of the neutron flux can be made with the help of a the following assumptions and approximations:

1. Activity (A) of the ^{226}Ra drives the neutron production of one neutron per α decay, resulting in a neutron activity of 100 kBq
2. The neutrons are emitted isotropically from the centre of the keg.
3. The same amount of neutrons is scattered out of the field of view of the detector as it is scattered back into the field of view.

The neutron flux ($\varPhi$) at a distance (r) of 10 cm from the centre, and the resulting flux through the detector ($\varPhi_{\text{det}}$) by multiplication of $\varPhi$ with the detector surface (A_{det}) can be calculated by the following equation:

$$\varPhi = \frac{\text{A}}{4\,\pi\,r^2} \tag{6.8}$$

$$\varPhi_{\text{det}} = \varPhi \times \text{A}_{\text{det}} \quad . \tag{6.9}$$

As a result of equation 6.9, a flux of approximately seven neutrons per second penetrating the detector is calculated for measurement position one. Together with the low detection efficiency, this delivers the explanation for the extensive measurement durations, of approximately two hours for the closest measurement

position with the lowest trigger level.
The measurements were all conducted with the "CX Spectroscopic Shaping Amplifier", which allows for an easy and quite intuitive post-processing of the signal pulses. However, the only information this amplifier provides, is the signal height, as the pulses are shaped. This does not allow for a discrimination between background signals, and secondary α-particles by their pulse shape which becomes impending, especially in the last measurement presented with the double converter configuration where the secondary α-particles energy deposition is shifted towards smaller values. Improvements to the readout board and the use of a non-shaping amplifier allowing pulse shape differentiation between neutrons and background, are logical consequences that can be drawn from this measurement campaign. An improved readout board together with a fast non-shaping amplifier is presented in the next chapter. Additionally, the following measurement campaign was performed at a research reactor with a significantly higher neutron to background ratio.

7 Neutron Flux Measurements at TRIGA Mainz

The first proof of principle measurements at the neutron source at TU Dortmund University, confirm that the developed prototype can be used to detect neutrons. However, the measurement setup does have its shortcomings: The readout board itself picks up electromagnetic noise due to long traces on the board that are not used, as well as the switch that allows the readout of multiple diodes. Further, the spectroscopic amplifier that was used allows for a rather fast and uncomplicated data analysis as only the peak height of the recorded waveforms provides information on the deposited energy. This demands the rather complex measurement procedure that requires two separate measurements: First, the measurement without the converter to determine the ambient noise and background level, and second, the measurement with the converter to then determine the neutron signal by comparison of the two measurements. The low activity of the neutron source in the centre of the keg of 100 kBq additionally results in long measurement durations. Therefore, a few minor and major adjustments to the measurement procedure are done: First, a new, simplified board is designed, second a fast transimpedance amplifier together with a more advanced post-processing of the data, allowing pulse shape discrimination, is used in the readout chain explained, and last, the measurements are performed at a research reactor TRIGA Mark II in Mainz with a significantly higher neutron flux.

7.1 Simplified Read Out Board

The revised readout board design is shown in figure 7.1. It is stripped down to the basic functionalities of the board. The board now only fits a small diode with its reduced length. Additionally, the switch with the long traces and additional contact pad is removed as well as the contacts allowing to stack multiple readout boards on top of each other for simultaneous readout. Lastly, the traces for the signal and the ground are are enlarged to reduce their impedance. The drill holes are designed to match with the converters produced for the longer board, but the converter aluminum sticks out on the end opposing the SMA connector.

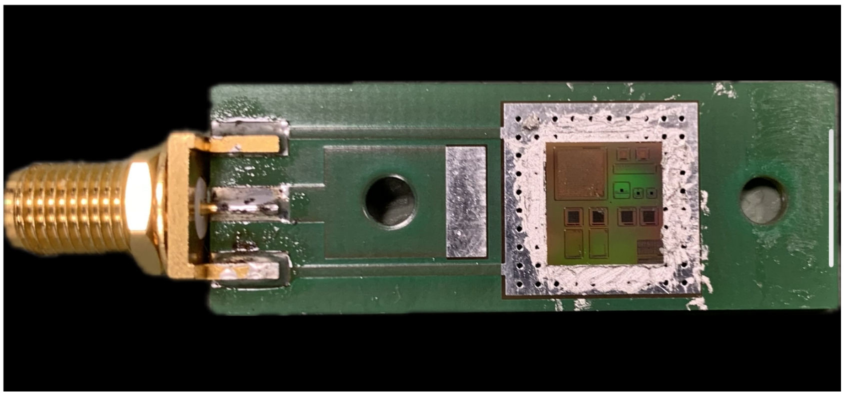

Figure 7.1: Simplified readout board with silicon diode mounted.

7.2 TRIGA Reactor and the Thermal Column

To test the neutron detector in higher neutron flux fields with less background radiation, the following measurement campaign was performed at the TRIGA Mark II reactor in Mainz. It is a nuclear reactor model [58] that cannot be used for power production, but for research purposes, isotope production, material testing, and for educational purposes. Figure 7.3 shows a schematic drawing of the reactor and the irradiation facilities.

TRIGA reactors are inherently safe. This means that a nuclear core meltdown is physically not possible due to the nuclear fuels used in the reactor core. The fuels contain uranium zirconium hydride (UZrH) which is the fuel and moderator in one material at the same time. This material has a negative "fuel temperature coefficient of reactivity". Which means that the higher the temperature of the fuel the smaller the reactivity becomes.

$$ {}^{1}_{0}n +^{235}_{92} U \rightarrow [^{236}_{92}U] \xrightarrow{85\%} fission\ (e.g.\ ^{139}_{56}Ba +^{94}_{36} Kr + 3\ ^{1}_{0}n) \tag{7.1} $$

$$ {}^{1}_{0}n +^{235}_{92} U \rightarrow [^{236}_{92}U] \xrightarrow{15\%}{}^{236}_{92}\ U + \gamma \tag{7.2} $$

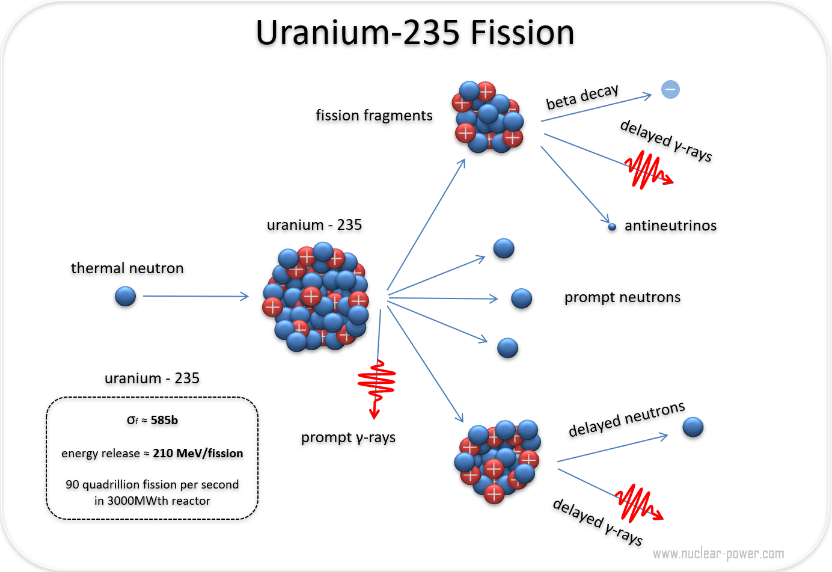

Figure 7.2: ^{235}U fission and radiative capture reaction induced by thermal neutrons [59].

The term reactivity is used to describe how quickly the reactors power level changes, meaning how many fission reactions are induced in the reactor core. The ^{235}U fission (see equation 7.1) cross section for thermal neutrons at room temperature is around 585 b [60], while the cross section for radiative capture (see equation 7.2) is around 99 b [60]. For fast neutrons the fission cross section is significantly smaller than for thermal neutrons. It lays in the order of barns. The kinetic energy of the prompt neutrons released in the fission reaction is $\approx$ 3 to 5 MeV. Therefore a moderator is used in nuclear reactors to moderate the fission neutrons to thermal energy levels so that they cause a subsequent fission reaction. When a reactor reaches its criticality, the number of neutrons released in each fission event sustain an ongoing chain reaction. In critical state the power output of the reactor is constant. If the fission neutron population increases a reactor can reach super criticality. This means that one fission neutron causes the production of more than one fission neutron in the next generation.

In nuclear power plants, this can lead to a nuclear melt-down. In the TRIGA reactors however, this is prevented by the negative "fuel temperature coefficient of reactivity" which can now be understood: Higher reactor core temperatures, due to energy deposition of nuclear fragments and neutrons, result in higher neutron energies which result in a smaller fission cross section, therefore, preventing super criticality. The water surrounding the nuclear fuels in the core of the reactor acts as a coolant for the fuels and as a shielding, so it is safe to stand on the reactor platform even when it is run critical.

The TRIGA reactor offers multiple possibilities for sample irradiation with neutrons of different energies. Close to the reactor core one finds the carousel and the pneumatic tubes allowing to send material samples close to the reactor core where mainly fast neutrons are present due to the above described fission reaction. A graphite reflector, also marked in figure 7.3, moderates the fast neutrons from the reactor cores inside down to thermal energy levels.

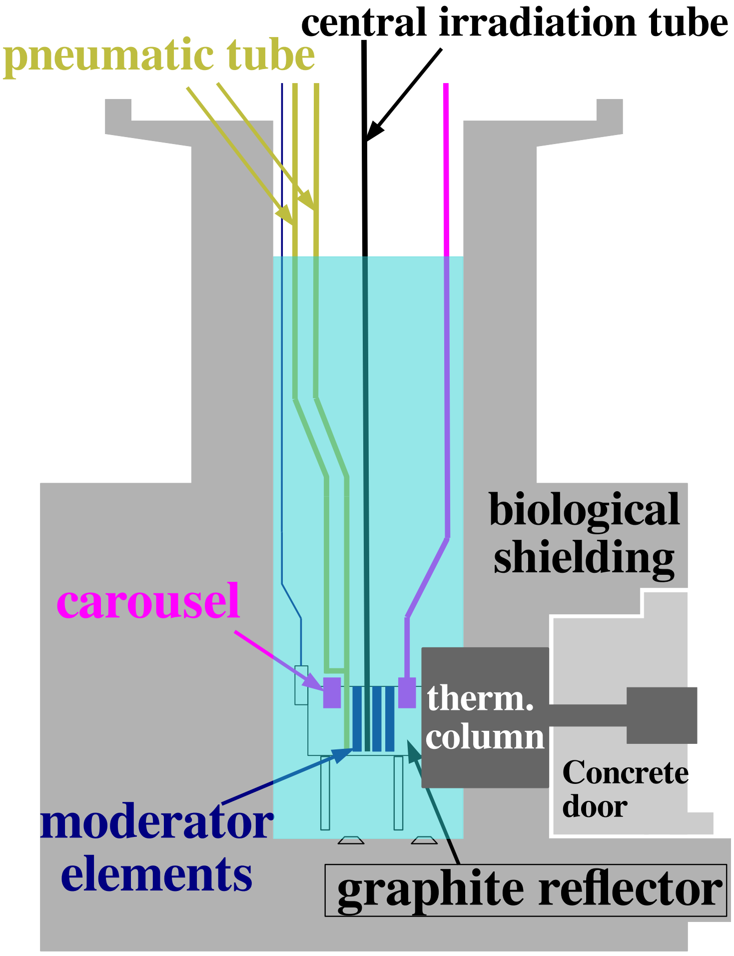

Figure 7.3: Schematic drawing of a TRIGA research reactor, and the location of the thermal column relative to the reactor core. Figure after [61].

Behind the graphite deflector is a cavity inside the reactors concrete allowing the irradiation with thermal neutrons, the ”thermal column”. It can be accessed by opening of a concrete door that is operated hydraulically. The maximum power output of the TRIGA reactor in Mainz is 100 kW. At that power the neutron flux inside the thermal column also reaches a maximum of 10^9 neutrons per cm^2 and s [61]. Additionally, the reactor can be operated in pulse mode where the reactivity is raised quickly causing an immediate rise of the reactor power output of 250 MW. This sudden rise of the reatcor power also causes a sudden increase in temperature of the fuel rods, ultimately causing the sudden decrease of reactivity. Therefore, the pulse length is limited to 30 ms [61].

7.3 Measurement campaign at TRIGA Mainz

For measurements with significantly higher neutron fluxes I had access to the thermal column at the research reactor TRIGA in Mainz. For the following measurement the detector with a single diode on the simplified readout board with a 2 µm thick ^{10}B enriched B_4C converter mounted to the back of the sensor is used. The detector is connected to the CIVIDEC C2 TCT amplifier described in 4.5.2. The amplifiers output is visualized and readout by a Tektronix MSO5204b mixed signal oscilloscope. The sampling rate is set to the 10 GS/s to prevent undersampling, as the amplified signals have a pulse width of a few ns. As the measurement time at the reactor is limited, only a qualitative noise occupancy determination is performed to determine the trigger level. For that purpose the detector is put into a light tight environment and the trigger level is adjusted so that no signals appear in the oscilloscope's screen over the time of 60 s. The trigger level is with −5 mV lower than in the laboratory setup at the TU Dortmund University where it was at −10 mV for the identical setup. This is most likely to a reduced electromagnetic background at the TRIGA.

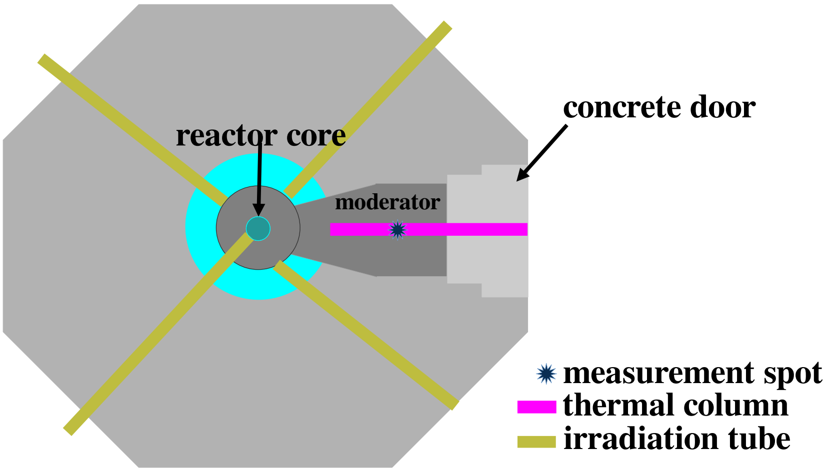

Figure 7.4: Schematic drawing of the top view of the reactor with the measurement spot marked with a blue star.

A plastic rod holds the detector that is fed into the thermal column of the reactor together with a number of TL-DOS detectors [33], from a dosimetry experiment that is performed at the same time. The measurement location is depicted in figure 7.4. Positioned at ≈ 56 cm from the end of the thermal column, closest to the reactor core. The detector is placed to balance measurement accuracy and equipment constraints. The limiting factor for the placement is the signal cable length which goes from the detector output to the amplifier.

To minimize activation risk, the amplifier and oscilloscope remain outside of the thermal column at the maximum possible distance to the reactor. An ethernet connection is used to connect a PC with the oscilloscope to control the measurement from behind a radiation shielding wall. This setup allows to run different readout scripts from the PC while the reactor is running, and therefore the direct access to the scope is impossible.

For the measurement campaign the reactor is operated at varying reactor powers and measurement durations shown in table 7.1. The table presents the measurements in the chronological order of their execution. The campaign stretched over two measurement days. measurements at lower reactor powers of 0.1 kW and 1 kW are performed on the first day, while the higher reactor powers (10 kW and 100 kW) and a reactor pulse were measured on the following day.

Table 7.1: Measurement campaign at the TRIGA reactor.

Measurement number	Reactor Power	Measurement Duration
1	0.1 kW	60 min
2	1 kW	60 min
3	0 W ramping down day one	16 h
4	10 kW	24 min
5	$\approx$ 220 MW	O(ms)
6	100 kW	4 min
7	0 W ramping down day two	16 h

7.3.1 Signal Analysis - TCT Amplifier

As discussed at the end of chapter 6, a significant improvement to the detector readout is the utilization of a fast transimpedance amplifier that allows to discriminate neutrons from background radiation. The analysis of the data taken is more complex than the analysis process for the spectroscopic amplifiers. Additionally, the limited experimentation time at the reactor did not allow for extensive noise investigations which hence have to be included in the data post-processing. The post-processing steps are as follows:

1. Read in of raw waveforms taken for each measurement.
2. Fast Fourier Transform (FFT) low pass filtering
3. Inverse FFT of the filtered signal.
4. Non-signal filtering
5. Offset calculation and subtraction
6. Full Width at Half Maximum (FWHM) calculation of the peaks in the waveforms.

Fast Fourier Transform (FFT)

During the measurements, we could observe that some of the recorded signals were overlayed by a high frequency signal. Therefore, the signals frequency components were analyzed with the help of a FFT. The FFT is a mathematical tool that allows the efficient calculation of the discrete fourier transform of a signal in the time domain into a frequency domain signal. The fourier transform of a signal $f(t)$ is defined as:

$$F(\nu) = \int_{-\infty}^{\infty} f(t) e^{-2\pi i \nu t} dt \quad . \tag{7.3}$$

The analysis of the signal waveforms are performed with python [62]. For the FFT and inverse Fast Fourier Transform (iFFT) calculation the $scipy.FFT$ is used [63]. First, a ROI between 45 and 60 nsecond is defined, as the position on the time-scale of the measured signal where the signal pulses would reach their minimum. The frequency power density spectrum of the ROI and the background signal components outside the ROI, between 0 and 45 nsecond, is shown in the upper plot in figure 7.5. The two power density spectra show that the main signal frequency components are below 300 MHz. Additionally, the power density spectra show a distinct peak around 0.8 GHz. A most likely source of that signal is a newly installed Global System for Mobile Communications (GSM) antenna in close proximity of the reactor. GSM signals can have signal frequencies around 900 MHz [64].

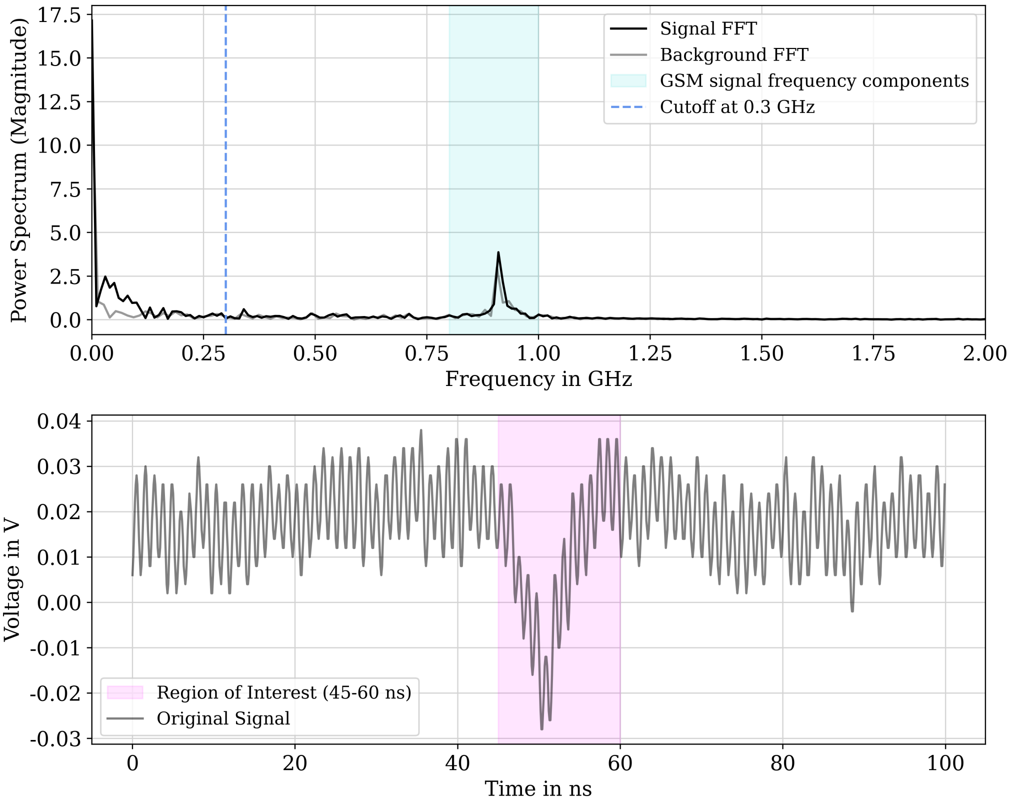

Figure 7.5: Power density spectrum of a signal recorded at GSM, together with a plot of its original, and filtered waveform in the lower plot. The frequency component is marked with a blue background in the power density spectrum.

Inverse Fast Fourier Transform (iFFT)

In step three, all frequencies above 300 MHz are set to zero, and an iFFT of the low pass filtered signal is performed, transferring the signal from the frequency, back into the time-domain. Figure 7.6 shows the original signal and the filtered and reconstructed signal. It also shows that the significant peak characteristics like the peak height, the pulse width and the slope of the leading and the trailing edge are maintained, while the GSM frequencies are filtered out.

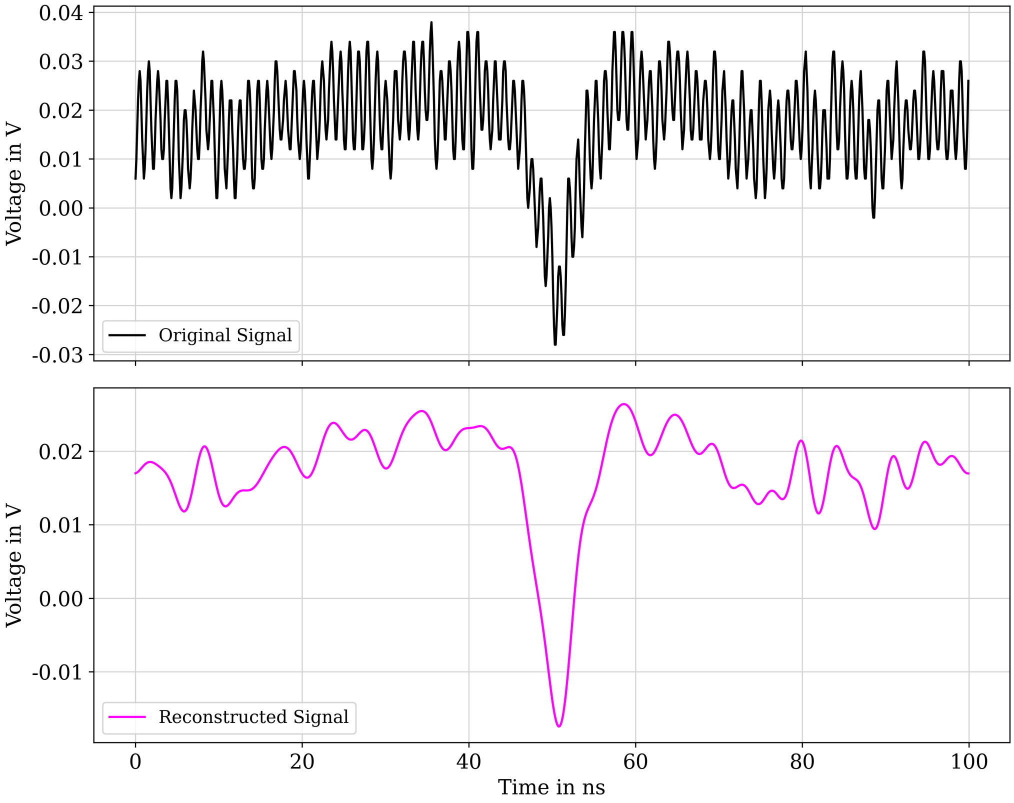

Figure 7.6: Original signal and reconstructed signal after low pass filtering.

Non-Signal FIltering

In step four of the processing, non signal hits as displayed in figure 7.7 are removed from the dataset. The qualitative analysis of the signal waveforms taken at TRIGA showed that the random noise signals typically had a sinusodial character as shown in figure 7.7.

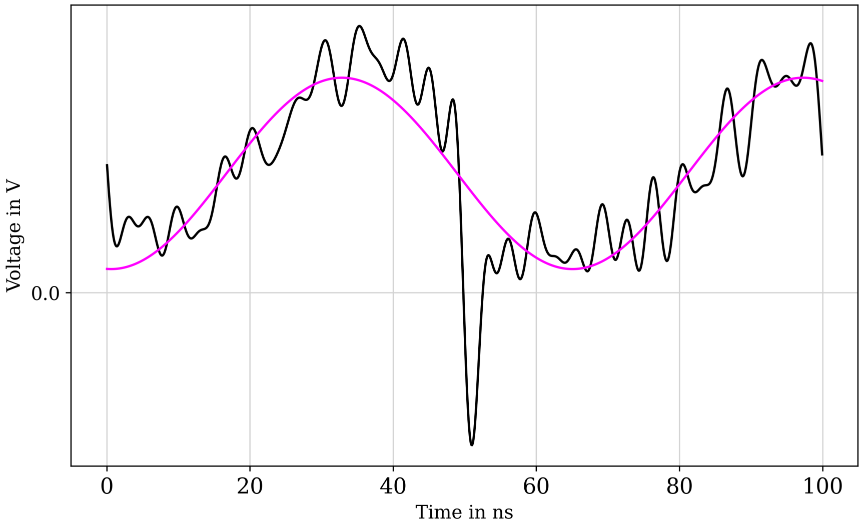

Figure 7.7: Low pass filtered characteristic local noise hit at TRIGA. The sine fit function describes the waveform very well so that it can be eliminated.

Therefore, a sine function is fitted to the filtered waveforms, and a goodness of fit test is performed in python. A high goodness of fit indicates that the waveform does not contain a signal pulse. Consequently, the waveform is rejected if its goodness of fit value is higher than 0.3. Figure 7.8 shows the histogram of the goodness of fit values ($\mathrm{R}^2 Value$) of a dataset.

The waveforms classified as noise with a goodness of fit below the determined threshold stem from additional filter criteria applied: Noise signals contain significant peaks outside the ROI, and can have additional significant positive peaks. Therefore, waveforms with these characteristics are eliminated. As a cross check validation, all waveforms classified as noise are visualized, as well as the waveforms classified as signal displayed in figure 7.9. The visual inspection shows a good discrimination between neutron associated signals and noise associated signals.

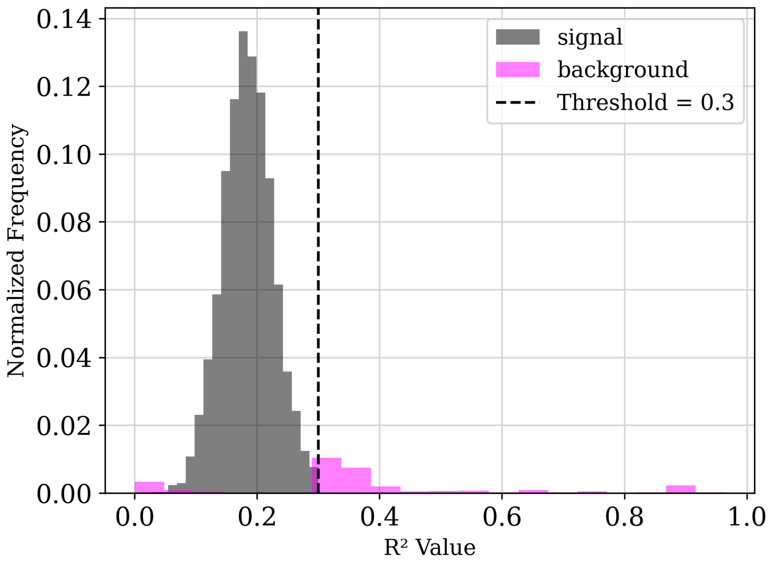

Figure 7.8: Goodness of fit histogram of the first measurement campaign with a reactor power of 100 W.

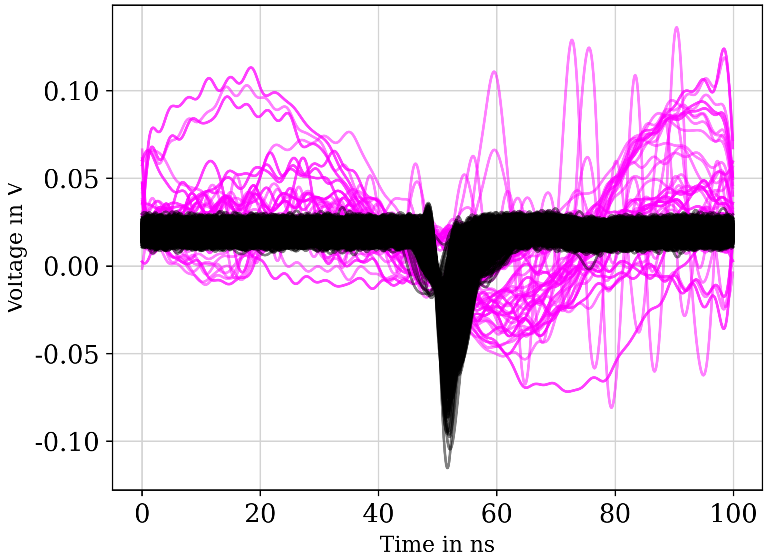

Figure 7.9: All waveforms for the first measurement campaign. With the waveforms classified as ”good” in black and the local noise signals plotted in pink.

Offset Subtraction and FWHM Determination

An offset calculation for each waveform classified as a signal hit, is performed in step five of the processing chain. The offset is calculated by determining the mean and the standard deviation before the ROI on the time axis, from 0 up to 40 ns. The individual offset of each waveform is then deducted from the peak height to determine the half maximum value of the peak: The intersections of a horizontal line at the half maximum peak height value, and the interpolated signal then determine the signals FWHM.

7.3.2 Pulse Shape Analysis - Neutron Discrimination

In order to discriminate between neutrons and background signals, I investigated the FWHM histograms of the long measurements after the reactor was ramped down on day one and day two. The histogram of the FWHM values of the measurement after day two, and the FWHM values of the measurement with the reactor running critical at 1 kW, can be found in figures 7.10 and 7.11. The two histograms show a significant difference, with an additional peak in figure 7.11. Further, the distribution of the FWHM values follow a Landau distribution for the measurement without neutrons, while the additional peak could be better described by a Gaussian distribution.
As described in chapter 2, neutron fields are always accompanied by background radiation dominated by de-excitation photons and electrons from ionization processes. The energy deposition of such particles in thin layers of silicon, characteristically follows a Landau [65] distribution. The Landau distribution can be approximated by the Moyal distribution which was also developed to describe energy deposition of Minimum Ionizing Particles (MIPs) in thin material layers [66]. In comparison to the Landau fit function, the Moyal function has a slightly broader peak description with a tail approaches zero faster than the Landau fit function. The Probability Density Function (PDF) of the Landau distribution is given by:

$$f_L(x;\mu,\sigma) = \frac{1}{\sigma}\Phi\left(\frac{x-\mu}{\sigma}\right), \tag{7.4}$$

where $\Phi(x)$ is defined as:

$$\Phi(x) = \frac{1}{\pi}\int_0^\infty e^{-t\log t - xt}\sin(\pi t)\,dt. \tag{7.5}$$

. The PDF of the Moyal distribution is given by:

$$f_M(x;\mu,\sigma) = \frac{1}{\sqrt{2\pi}\sigma}\exp\left(-\frac{1}{2}\left(\frac{x-\mu}{\sigma} + e^{-\frac{x-\mu}{\sigma}}\right)\right). \tag{7.6}$$

In both functions the parameter μ is the most probable value that controls the horizontal shift of the PDF, while σ describes the spread of the distribution. In comparison to the Moyal PDF the mean of the Landau PDF cannot be calculated, due to its asymptotic tail. The Moyal distribution is chosen for the following analysis, as the FWHM histograms display a finite maximum FWHM values determined.

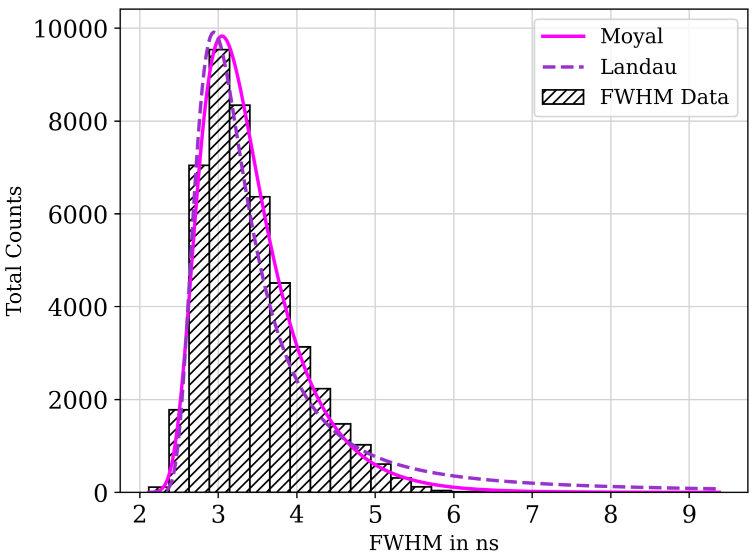

Figure 7.10: FWHM histogram of the a measurement conducted after the reactor was turned off.

The distribution of the FWHM values obtained while the reactor was running, is best described by a combination of the Moyal and a Gaussian function whose PDF is described as follows:

$$f_{\text{combined}}(x) = f_{\text{Moyal}}(x) + f_{\text{Gaussian}}(x), \tag{7.7}$$

where $f_{\text{Moyal}}(x)$ is given in equation 7.6, and $f_{\text{Gaussian}}(x)$ is:

$$f_{\text{Gaussian}}(x) = A_{\text{Gauss}} \cdot \frac{1}{\sqrt{2\pi}\sigma_{\text{Gauss}}} \exp\left(-\frac{(x-\mu_{\text{Gauss}})^2}{2\sigma_{\text{Gauss}}^2}\right). \tag{7.8}$$

Thus, the final combined expression is:

$$
\begin{aligned}
f_{\text{combined}}(x) = A_{\text{Moyal}} \cdot \frac{1}{\sqrt{2\pi}\sigma_{\text{Moyal}}} \exp\left(-\frac{1}{2}\left(\frac{x-\mu_{\text{Moyal}}}{\sigma_{\text{Moyal}}} + e^{-\frac{x-\mu_{\text{Moyal}}}{\sigma_{\text{Moyal}}}}\right)\right) \\
+ A_{\text{Gauss}} \cdot \frac{1}{\sqrt{2\pi}\sigma_{\text{Gauss}}} \exp\left(-\frac{(x-\mu_{\text{Gauss}})^2}{2\sigma_{\text{Gauss}}^2}\right) \quad . \qquad (7.9)
\end{aligned}
$$

The Gaussian fit model describes the FWHM distribution for α-particles very well, as they are heavy charged particles which deposit their whole energy inside the sensor. Therefore, their deposited energy should be described by a Poisson PDF which is here approximated with a Gaussian as the statistics are very high.

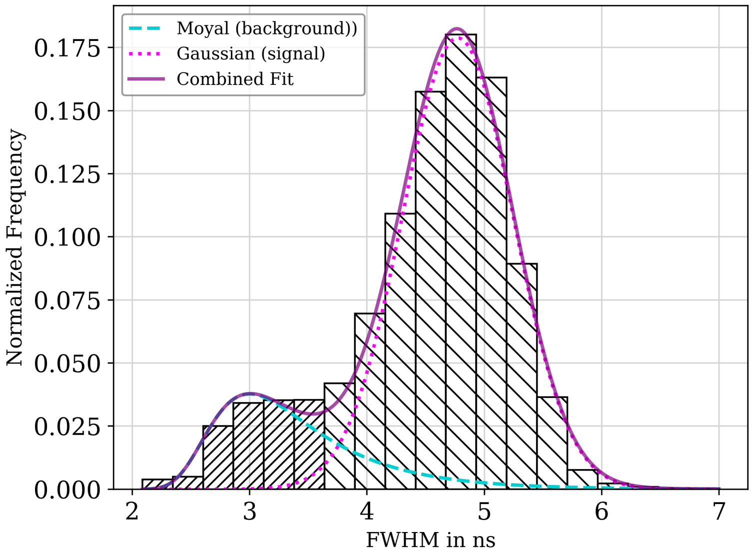

Figure 7.11: FWHM data for the measurement at 0.1 kW over 60 min.

From the combined Moyal and Gaussian fit shown in figure 7.11 several important values for the further analysis can be extracted: Firstly, the intersection value between the Moyal and the Gaussian fit, which is defined as the neutron threshold for this measurement campaign. Secondly, the ratio between the Gaussian integral and the integral of the combined fitting function is introduced as the purity. And last, the Most Probable Value (MPV), for the Moyal, and the mean value for the Gaussian fit as the estimate for the background FWHM and neutron FWHM.
The plotting of the average waveform of signals with a FWHM equal or smaller than the MPV of the background, and the average waveform of signals with a FWHM equal or bigger than the MPV of the neutron signals, shows a clear difference in the

pulse shape. The slopes of the leading and trailing edges of the neutron associated signals display a similar incline/decline while the incline of the trailing edge of the background associated signal shows a smaller slope. The difference in signal shape hints that the background signal is dominated by particles despositing energy along a track through the sensor, consequently resulting in a less steep trailing edge. The neutron signal is dominated by α-particles which deposit their whole energy in a small volume due to their high LET, resulting in a steep leading and trailing edge, as described in chapter 4, section 4.4.

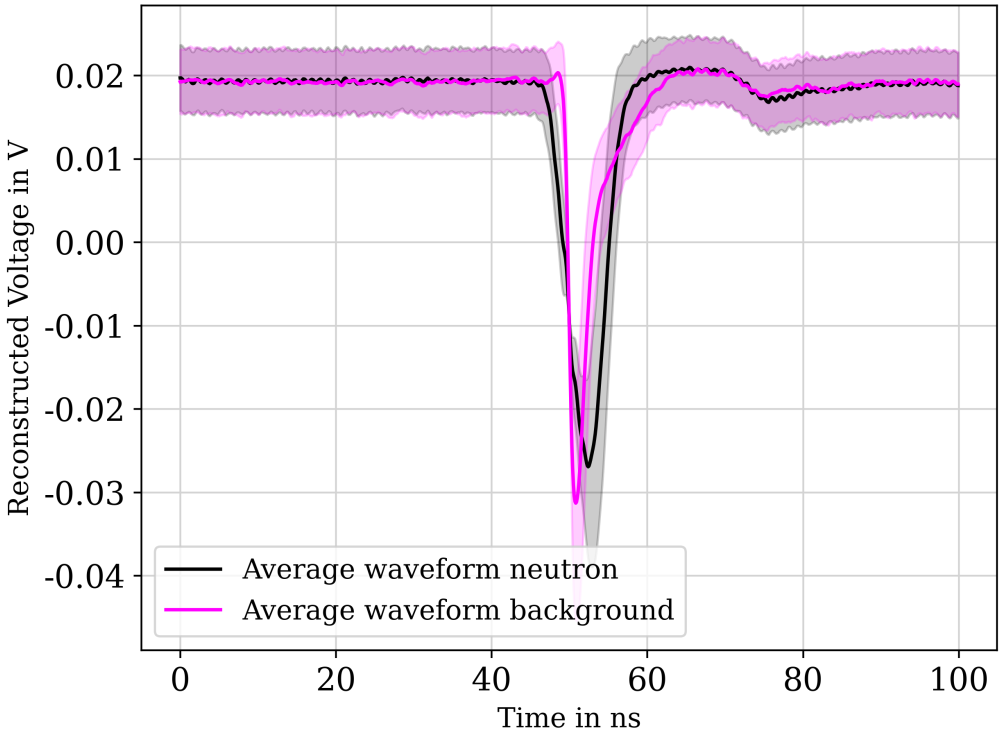

Figure 7.12: Average waveform of background (pink) and neutron (black) associated signal.

To determine a neutron threshold, the mean and standard error of the mean of the individual neutron threshold for each measurement are determined to be at 3.73 ± 0.11. Figure 7.13 displays the hit rate in intervalls of 60 s for the first measurement with a constant reactor power of 100 W. It visualizes the neutron and the background hits individually. The time when the reactor was operated critical is highlighted. The neutron hit rate is constant within the uncertainties, while the reactor was operated critical. and it decreases quickly after the reactor was turned off.

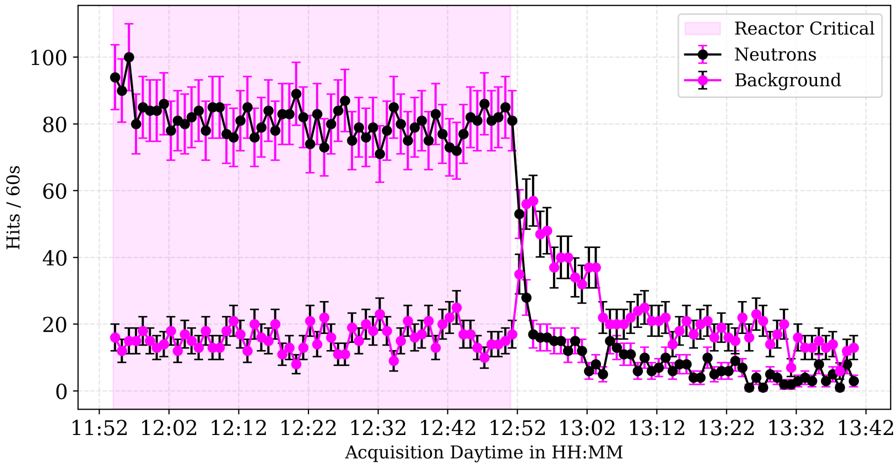

Figure 7.13: Neutron and Background hit rates in intervals of 60 seconds for a reactor power of 100 W.

The hit rate of the second measurement with a reactor power of 1 kW is displayed in figure 7.14. In comparison to the first measurement presented with a lower reactor power, the background hit rate increases as soon as the neutron hit rate decreases when the reactor is turned off. The decrease of the background and neutron associated signals after the reactor was turned off, and was cooling down after the first measurement day, is visualized in the upper plot in figure 7.17.

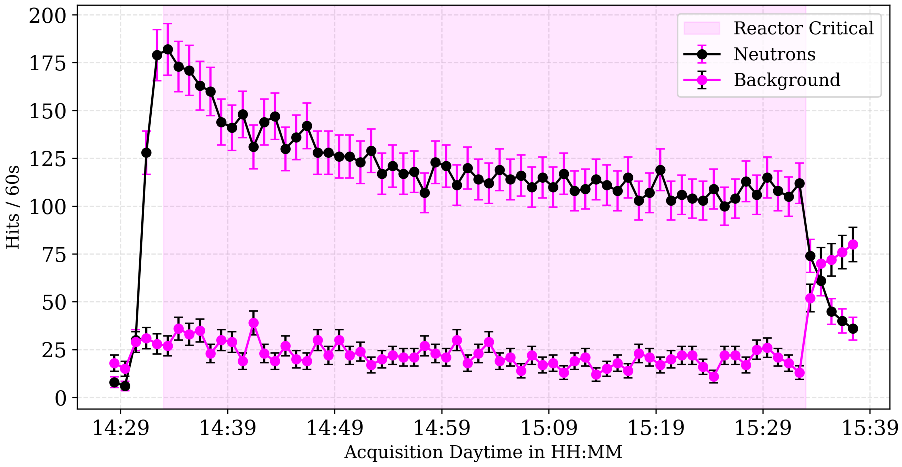

Figure 7.14: Neutron and background hit rates in intervals of 60 seconds for a reactor power of 1 kW.

The observed increase in background associated signals as soon as the reactor is turned off, cannot be explained by physical processes. Therefore, the signal to background ratio is analyzed and displayed in intervals of 60 s in figure 7.15. The signal to background ratio drops immediately after the reactor is turned off. This delivers the explanation that there is no significant increase in background radiation, but that this is an effect of a saturation of the readout system.

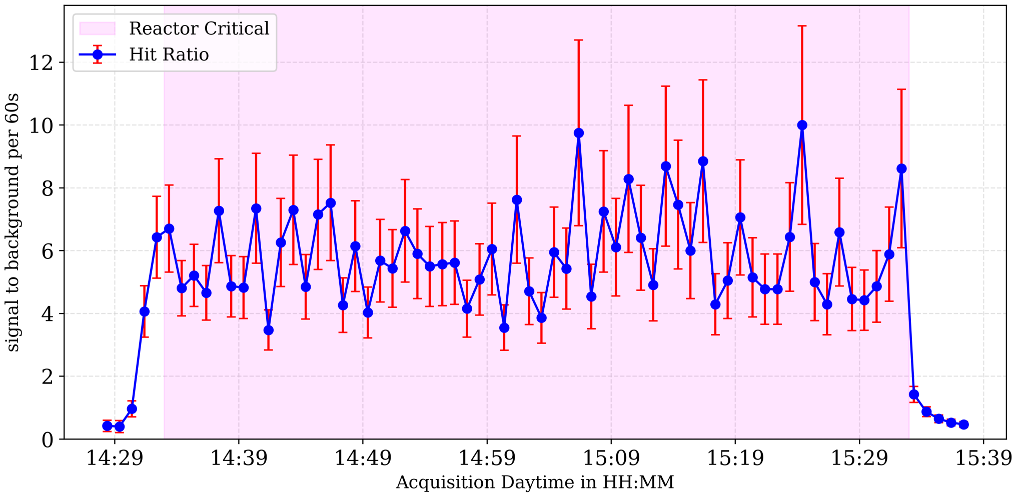

Figure 7.15: Signal to background ratio for a reactor power of 1 kW.

The measurement results for the irradiation campaign of the second day, presented in figure 7.16 show significantly higher background hit rates. Without the pulse shape analysis prior to the hit rate analysis, it would not be possible to determine the times when the reactor was operated or not. Before the reactor was operated in pulse mode, it was critical at 50 W for 23 minutes which is shown in the middle plot of figure 7.16. In contrary to that clear indication of the low reactor power, the reactor pulse which has a length of 30 ms [61] cannot be resolved. The most likely explanation is the system's data acquisition speed limit.
All three measurements performed at higher reactor powers show the subsequent increase in background signal hit rates as soon as the neutron hit rates decrease. As there is no physical explanation for that behaviour, the saturated data acquisition speed must be the explanation for that.

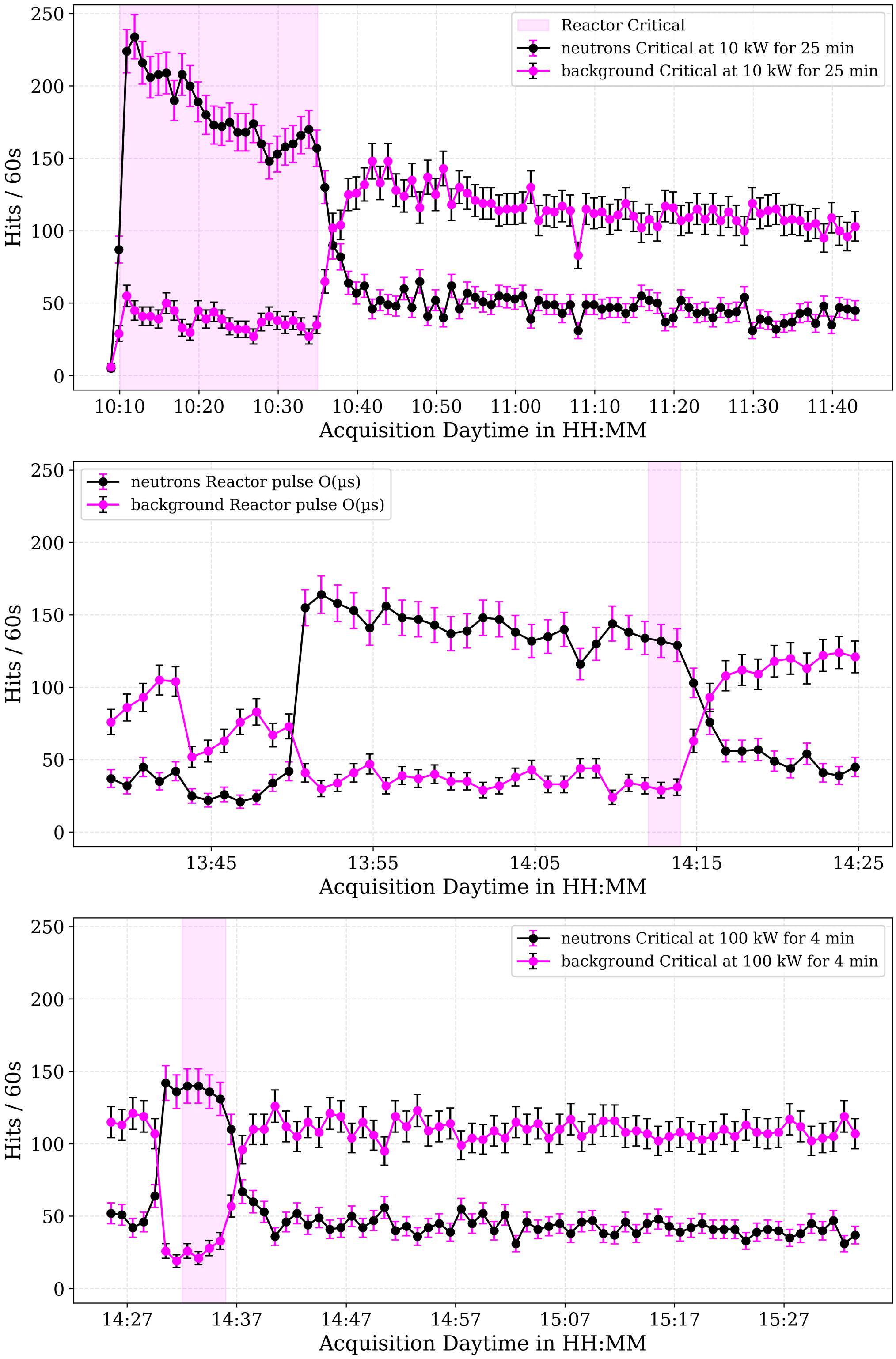

Figure 7.16: Neutron and background hit rates in intervals of 60 seconds for higher reactor powers of 10 kW (top figure), the reactor pulse (middle figure), and a reactor power of 100 kW (bottom figure).

The increase in hit rates on the second day could possibly be explained by significantly more activations of the material present in the thermal column. When the thermal column was opened after the first two measurements, the radiation safety officers would measure the dose rate right next to the opened door. For the first day, the dose rate measured at the detector position was at 0.5 µSv/h after the irradiation and the consequent cool down for 16 h. This slightly activated detector was then used for the measurements of the second day. The measurements of that day show significantly higher hit rates both in neutrons, as expected, as the reactor power was also higher, but also in background signals. One explanation is that the materials inside the thermal column were heavily activated, as a dose rate measurement after the operation of the reactor at 10 kW showed 20 µSv/h. The door was not opened until the next morning after the reactor pulse, and the measurement with 100 kW due to radiation safety concerns.

7.4 Background Decay after the Measurements

Figure 7.17 shows the result for the two measurements that were started at the end of each measurement day. They show the detected hit rates in intervals of 60 s after the reactor was turned off. The durations of both measurements were approximately 16 h.

The background hits after the reactor was turned off on day two do not drop with a similar characteristic as the hit rates after the first measurement day which follows an exponential decay, as displayed in figure 7.17.

An explanation for the slower decrease of the background signal rates can be, that significantly more long lived nuclides were activated in the irradiations on day two due to the higher reactor powers. However, figure 7.17 also shows that the neutron hit rate does not decrease to the same low level of approximately zero hits per minute as after the first day which could also be due to activation of long lived nuclides.

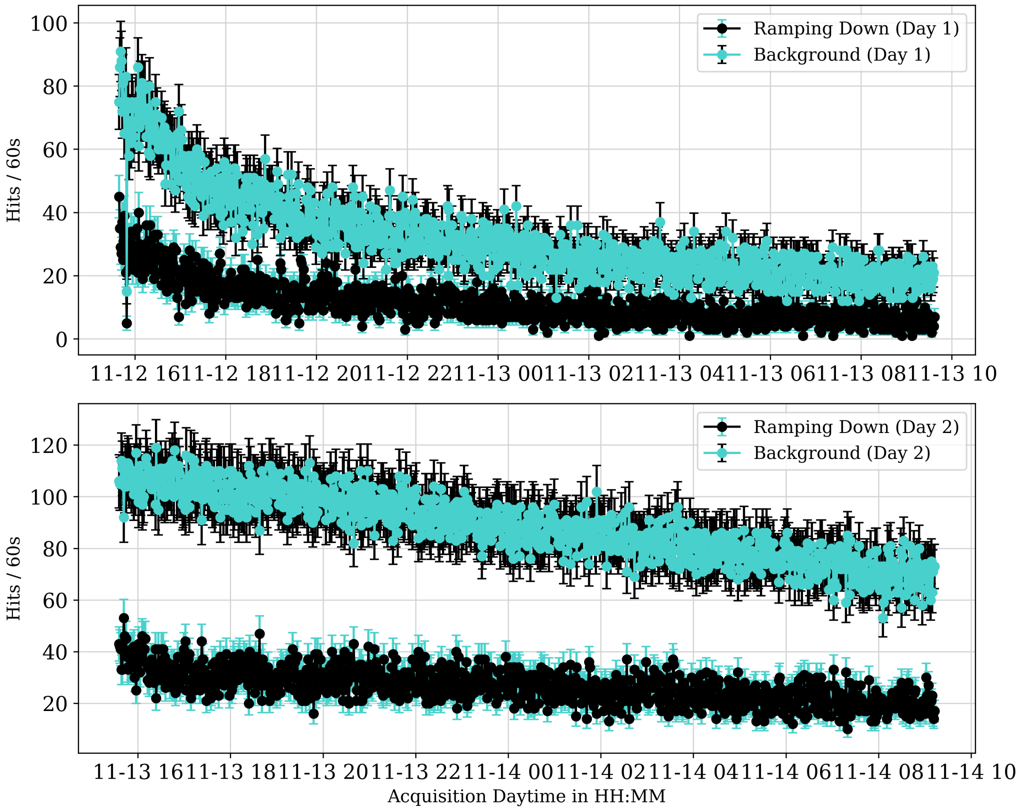

Figure 7.17: Neutron and background decay after the reactor was shut down. The upper plot shows the decay after day one, and the lower plot shows the decay after day two.

7.5 Neutron Purity

The neutron purity for the improved detector setup is investigated by determination of the ratio between the integrals of the Gaussian and the Moyal distribution for the measurements while the reactor was operated critical. The results together with the Poisson uncertainty propagation is displayed in figure 7.18. Within the uncertainties, the neutron purity remains constant. As a consequence, this means that the purity is not dependant on the reactor power.
The plot also shows the mean hit rate of hits above the determined neutron threshold per time for the different measurements. It can be seen, that the hit rates increase for the measurements up to 10 kW. However, the measurements for higher reactor powers do not follow that trend. Unfortunately the measurement at 100 kW could only be performed over the duration of four minutes on that day. Increased measurement durations at higher reactor powers would be desirable when planning for measurement campaigns performed as a follow up for this work.

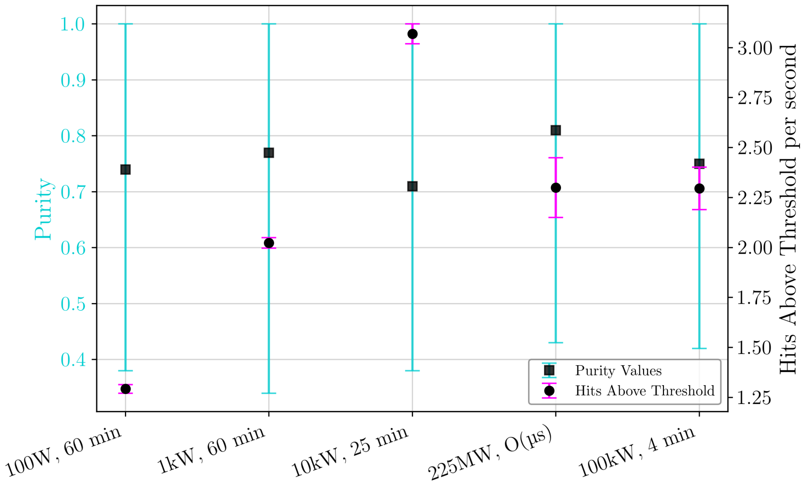

Figure 7.18: Purity and detected neutron associated hit rates per second for the investigated reactor powers.

7.6 Offset Investigations

To investigate whether the irradiation after the first day had an influence on the detector operation, the mean offset and its standard deviation is shown in figure 7.19. The figure shows that the offset decreased after the first measurement, which is the only measurement distinguishable from the following measurements within its uncertainties. However, it is not possible to detect a trend in the mean offset development over the measurements. The standard deviation of the offset values can describe the statistical noise fluctuations for of the system. However, the plot shown in figure 7.19 also shows that the standard deviation for each measurement also does not increase over the measurements. This means that the noise within the system does not increase significantly.

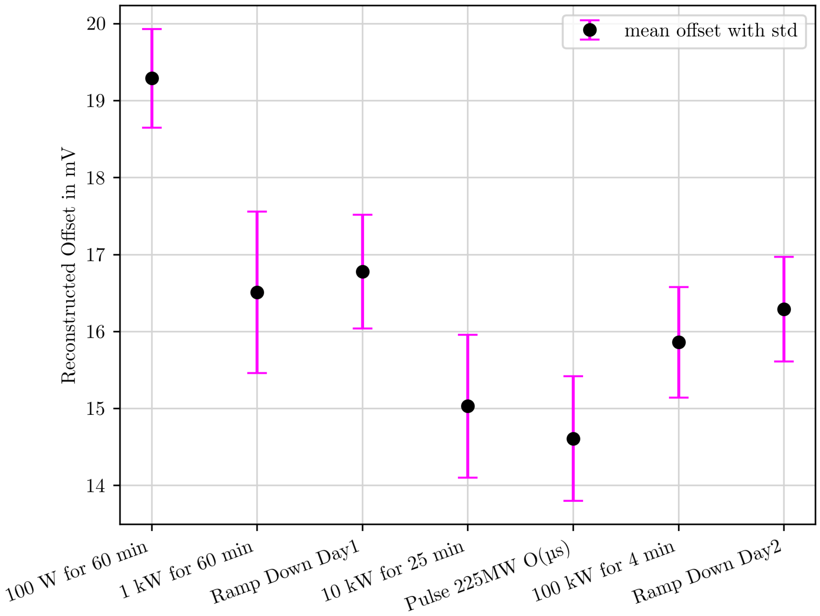

Figure 7.19: Average offset with standard deviation for the different measurement campaigns.

7.7 Conclusion of the Measurement Campaign

As a conclusion, the measurement campaign demonstrated that the new detector readout system makes neutron detection more efficient as they can be differentiated from the background with the help of the pulse shape analysis. Therefore, only one measurement is needed as in comparison to the detector readout system described in chapter 6.

For all measurements at the various reactor powers it can be clearly said that the times when the reactor was operated critical are precisely described by the increasing hit rate of neutron interaction associated hits in the detector. The measurements also show that the neutron rate drops quickly to a low constant rate within approximately 5 min after the reactor power was turned off for all different reactor powers.

However, it was not possible to distinguish between the different reactor powers, as the hit rates did not increase as expected. The most likely explanation for that behaviour is the limited data acquisition speed. The plot of the neutron to background associated signals could prove that theory, as it demonstrated that, what looked like an increase in background radiation, was actually an effect of the limited data acquisition. As the reactor was turned off, the data acquisition system was not busy by neutron associated signals anymore, which is why more background signals could be recorded. That effect caused the impression of an increasing background radiation hit rate when analyzing the data.

Nevertheless, the developed readout worked well for the detailed analysis of the signal shapes. Additionally, the slow data acquisition resulted in smaller data files, allowing measurement campaigns for over 16 hours. This made it possible to measure the characteristics of the background signal decrease over time after the reactor was turned off.

For future measurement campaigns, improving the data acquisition speed would be more beneficial in order to accurately resolve the neutron count rates for different reactor powers.

8 Summary and Outlook

In this thesis, a prototype for a silicon-based neutron detector and its readout were successfully characterized, tested, and improved. It was demonstarted that the detector can be used for neutron detection in low, and high neutron flux environments. The development of a pulse shape discrimination algorithm allows to use the detector in mixed radiation fields without the necessity of a separate reference measurement of the background.

The measurement performed at the neutron source at the TU Dortmund University, could demonstrate that the prototype with a simplified read out with a shaping amplifier and post processing utilising a pulse height discrimination, can measure neutrons in a low flux environment. The detector read out can be well used for quick, and easy to analyze detection efficiency investigations of single converter configurations, as a stack of multiple detectors or different converter materials as simulated in the BSc. thesis of R. Trimpop [45].
The low neutron flux inside the neutron source caused extensive measurement durations, ranging upt to several days for the measurement positions with the lowest neutron flux inside the neutron source. The comparison of the purity determination of the datasets reveals that the detector in single converter configuration achieves a higher purity than the detector in double converter configuration, which is in contradiction to simulation works ([7, 45]). This effect is best explained by the limited energy deposition of α-particles inside the sensor as a result of the increased distance between the front converter and the detector.
A converter that emits secondary particles with larger ranges in air could help overcome this problem. One of these converter materials is ^{6}Li enriched ^{6}LiF. It does have a smaller neutron capture cross section than ^{10}B , but as described in chapter 4, the secondary particles (α-particles and ^{3}H) have bigger ranges in air, as the ^{3}H are lighter than α-particles , and the generated α-particles from the ^{6}Li capture reaction have higher initial energies resulting in larger energy depositions in the sensor.
The investigations of the influence of a ^{6}Li converter could be realized in future works that could also investigate different efficiency enhancing detector configurations, as a stack of multiple detectors, or double converter layers as described by R, Trimpop [45].
The measurements at the TRIGA revealed that it is possible to detect precisely

when the reactor power was increasing or decreasing, and when it was operated critical. Overall, it can also be said that the pulse shape discrimination algorithm worked well to distinguish between background and neutron signals.

Regarding the count rates at the different reactor powers, it is clear that the measured count rate increases, but not linearly with reactor power. Especially the higher reactor powers do not follow that trend. The results showed that due to the saturation of the readout system, the power output of the reactor cannot be determined with the system as is.

For future measurement campaigns, the data acquisition speed should be improved to be able to resolve more accurately neutron count rates for different reactor powers. That could be realized with a Field Programmable Gate Array (FPGA) with a fast signal discrimination logic implemented to discriminate between neutrons and background radiation.

Even though the data acquisition of the developed detector system is too slow to clearly resolve the reactor power, it could resolve a trend, and the work has paved the way for further detector improvements. An interesting future outlook for a further development is the combination of an active silicon detector with a passive $\uparrow 6Li$-based TL-DOS neutron detector. The active detector would be used to detect secondary particles created in neutron interactions with the passive detector. If these interactions rise quickly due to a sudden increase in neutron flux, the active detector could generate a warning signal to help protect the user, and to trigger a timely analysis of the passive detector data even before the monthly cycle has passed. That procedure would allow the exact dose determination of the incident registered by the active neutron detector, ultimately serving as an increased radiation safety for exposed personnel.

Another interesting field of application for a detector setup with an improved neutron detection efficiency, would be inside a Bonner Sphere Spectrometer (BSS) to replace the currently used ^{3}He proportional counters. As the detector can be easily produced, multiple detectors could be used to measure the neutron flux with multiple spheres simultaneously. This would help decrease the measurement durations significantly, as currently neutron spectra are obtained with only one or two proportional counters operated at the same time. The alternative BSS system would then allow for neutron spectra to be measured more easily and faster, resulting in hopefully more frequent neutron spectra supervision in workplaces.

9 List of Abbreviations

ASTAR Alpha Stopping Power And Range table

BSS Bonner Sphere Spectrometer

e/h electron-hole

ESS European Spallation Source

EURADOS European Radiation Dosimetry Group e.V.

FFT Fast Fourier Transform

FPGA Field Programmable Gate Array

FWHM Full Width at Half Maximum

GSM Global System for Mobile Communications

iFFT inverse Fast Fourier Transform

INFN Istituto Nazionale di Fisica Nucleare

LET Linear Energy Transfer

MIPs Minimum Ionizing Particles

MPV Most Probable Value

NIST National Institute of Standard and Technologies

OpAmp Operational Amplifier

OSL Optically Stimulated Luminescence

PDF Probability Density Function

PE polyethylene

PVD Physical Vapor Deposition

RDN relative difference in normalized counts

RMS Root Mean Square

ROI	Region of Interest
SMA	SubMiniature version A
TLD	thermo luminescence detector
TL-DOS	Thermo Luminescence Dosimeter
TLDs	thermo luminescence detectors
TRIGA	Training Research Isotopes General Atomics

A Appendix

A.1 Peak Height Comparison Histograms for the Proof of Principle Measurements

The following plots show the histograms and the belonging RDN calculation results that were not shown explicitly in chapter 6

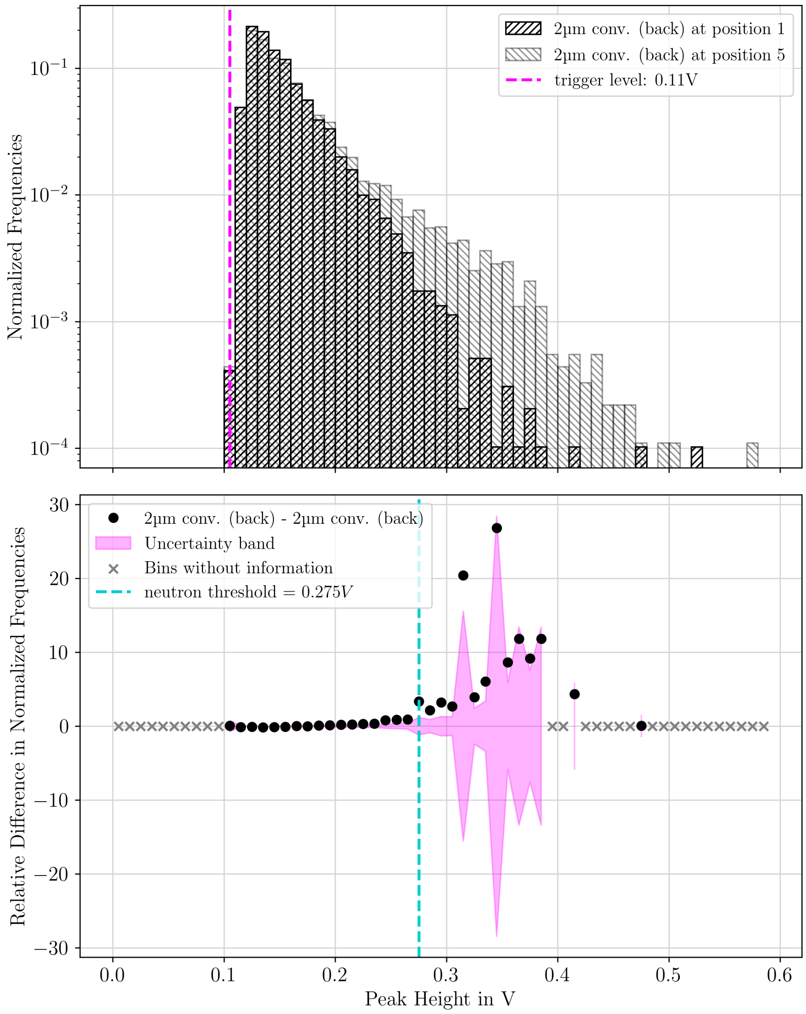

Figure A.1: Peak height histogram for measurements without and with a 2 µm ^{10}B enriched B_4C neutron converter mounted from the back of the sensor at position 5.

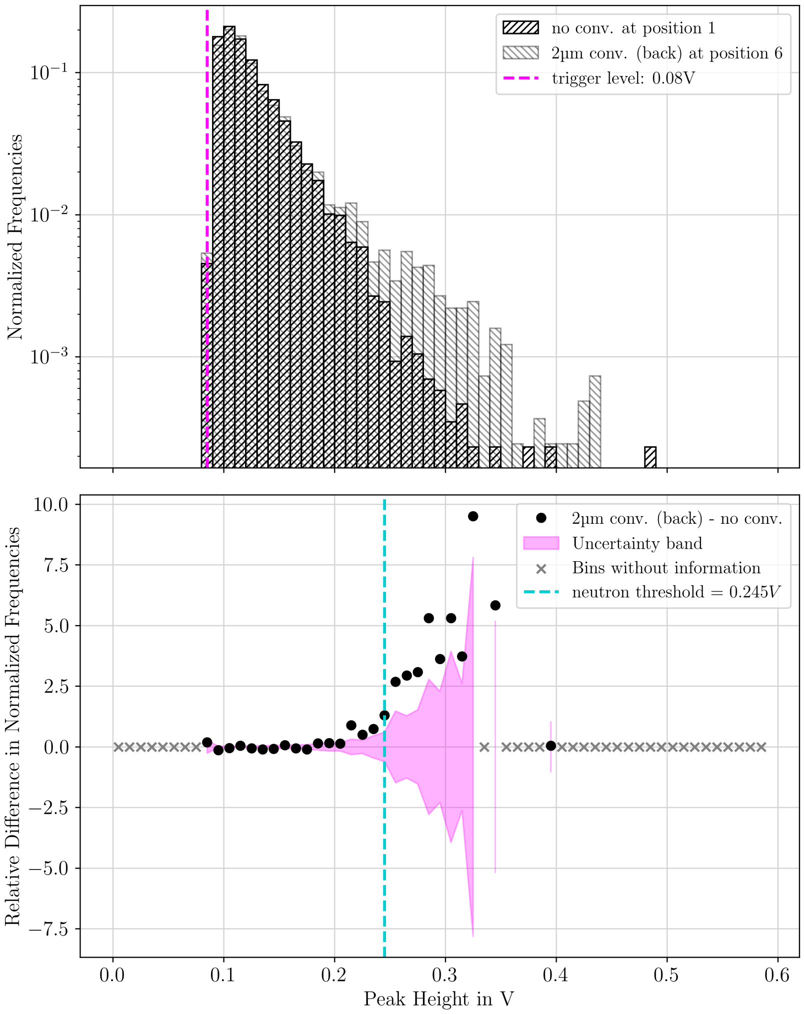

Figure A.2: Peak height histogram for measurements without and with a 2 µm ^{10}B enriched B_4C neutron converter mounted from the back of the sensor at position 6.

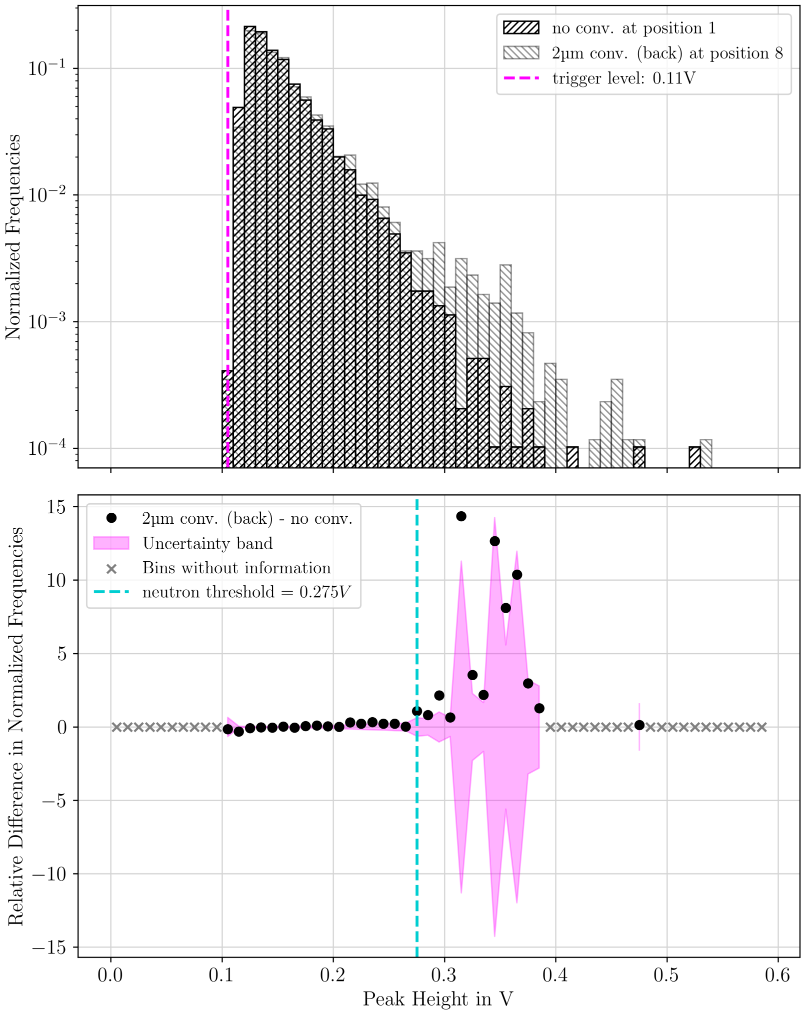

Figure A.3: Peak height histogram for measurements without and with a 2 µm ^{10}B enriched B_4C neutron converter mounted from the back of the sensor at position 8.

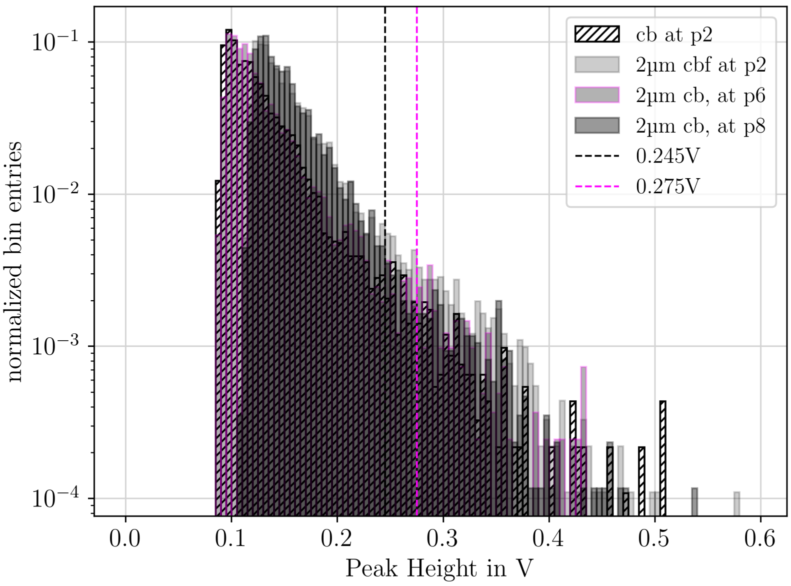

Figure A.4: Peak height histograms of the measurements performed at measurement spots with increasing distance to the centre of the neutron source. The datasets were taken with different trigger threshold, which is why the two determined neutron thresholds are displayed in the histogram.

A.2 FWHM Histograms of TRIGA Campaign

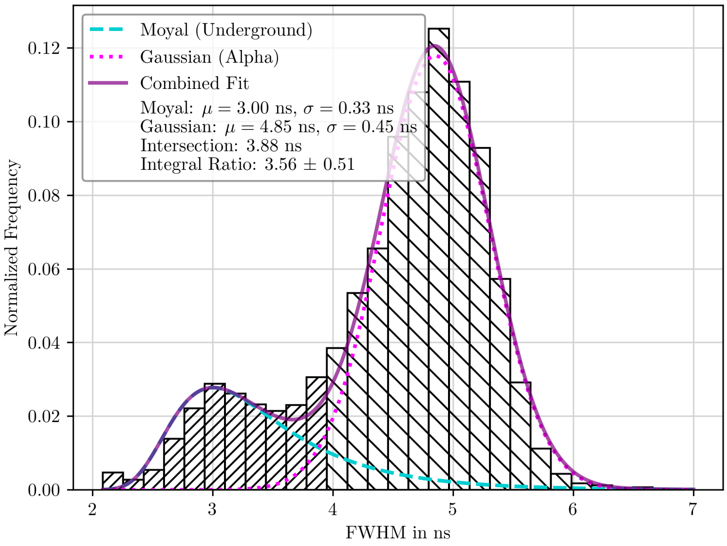

Figure A.5: FWHM histogram combined Moyal and Gaussian fit with reactor operated at 0.1 kW for 60 min.

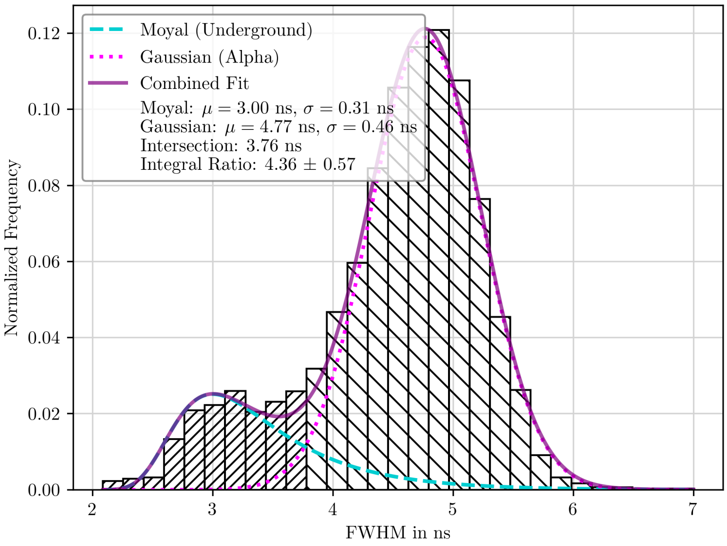

Figure A.6: FWHM histogram combined Moyal and Gaussian fit with reactor operated at 1 kW for 60 min.

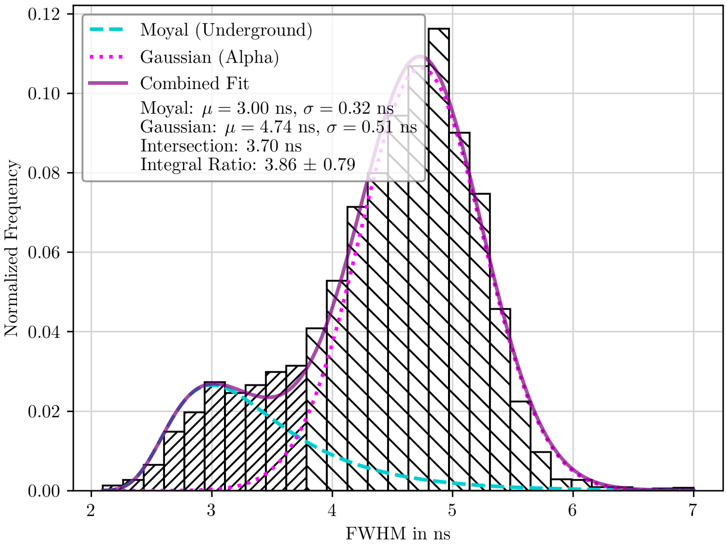

Figure A.7: FWHM histogram combined Moyal and Gaussian fit with reactor operated at 10 kW for 24 min.

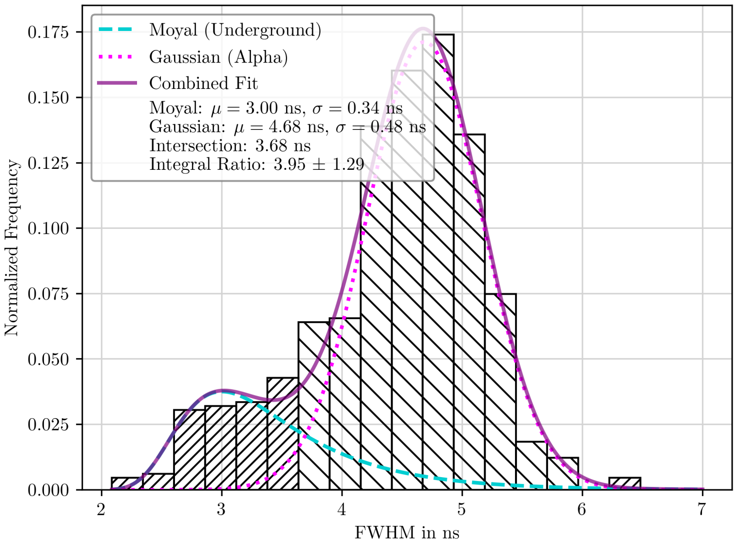

Figure A.8: FWHM histogram combined Moyal and Gaussian fit with reactor operated at 10 kW for 4 min.

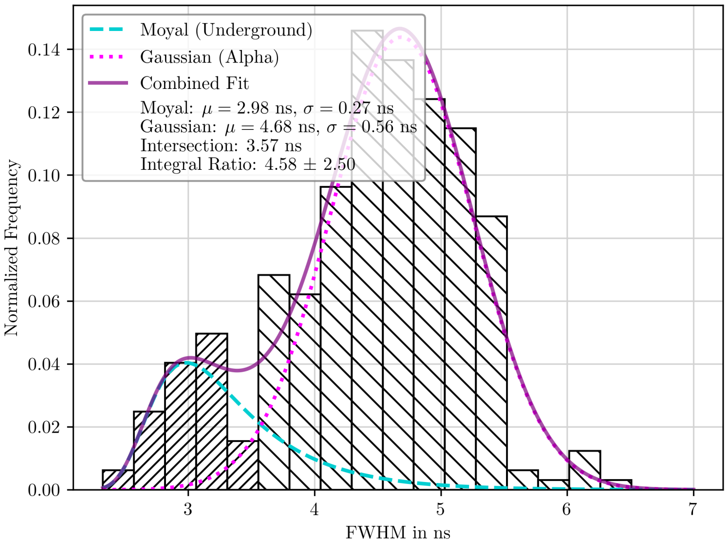

Figure A.9: FWHM histogram combined Moyal and Gaussian fit with reactor pulse.

A.3 Signal to Background Ratio for Different Reactor Powers

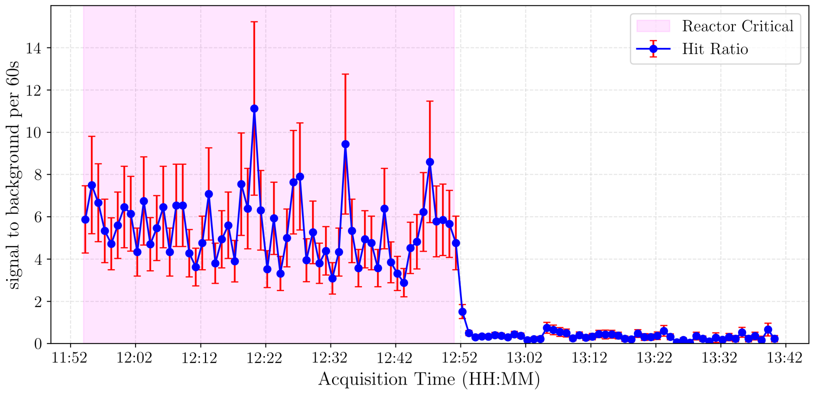

Figure A.10: Signal to background hitratio in intervals of 60 s for a reactor power of 100 W

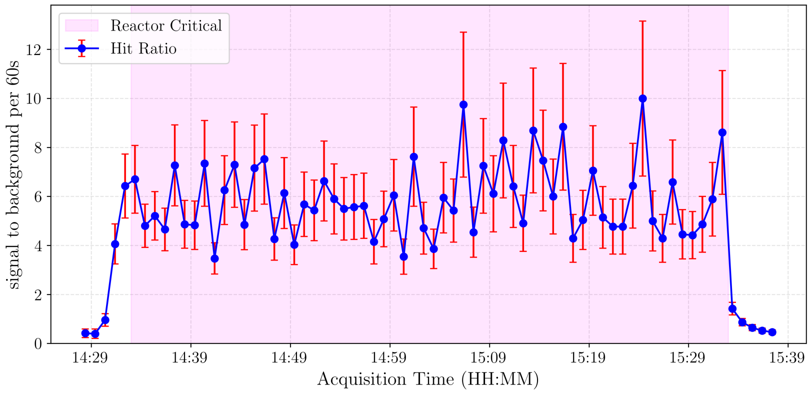

Figure A.11: Signal to background hitratio in intervals of 60 s for a reactor power of 1 kW

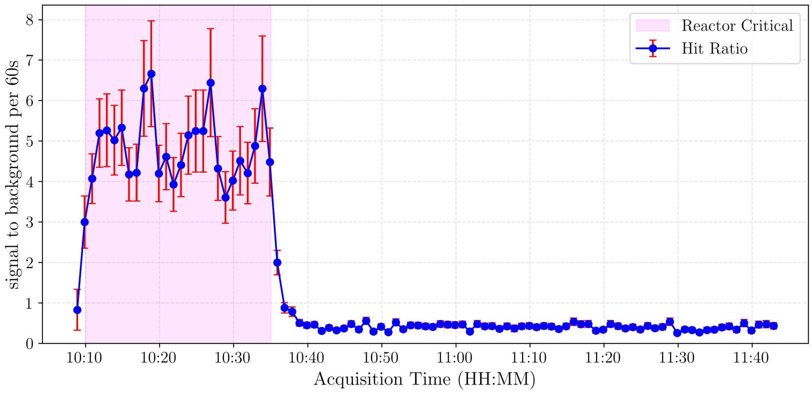

Figure A.12: Signal to background hitratio in intervals of 60 s for a reactor power of 10 kW

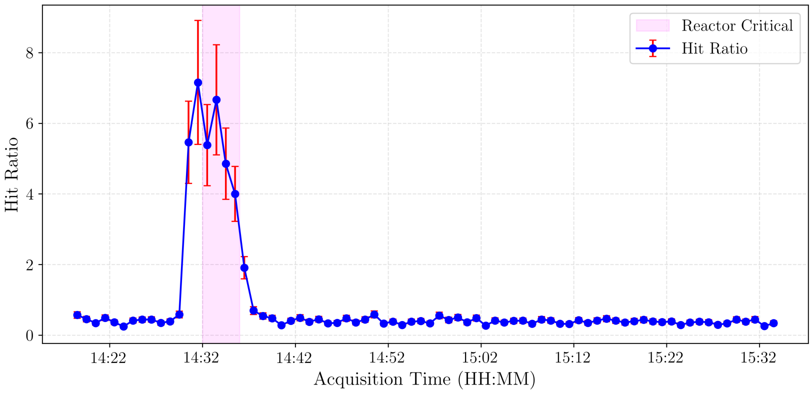

Figure A.13: Signal to background hitratio in intervals of 60 s for a reactor power of 100 kW

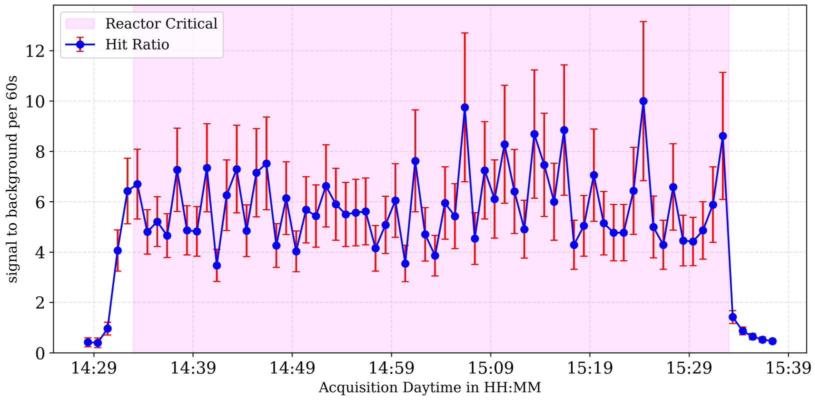

Figure A.14: Signal to background hitratio in intervals of 60 s for a reactor pulse, with the time around the pulse marked.

A.4 Offset Investigations for TRIGA Campaign

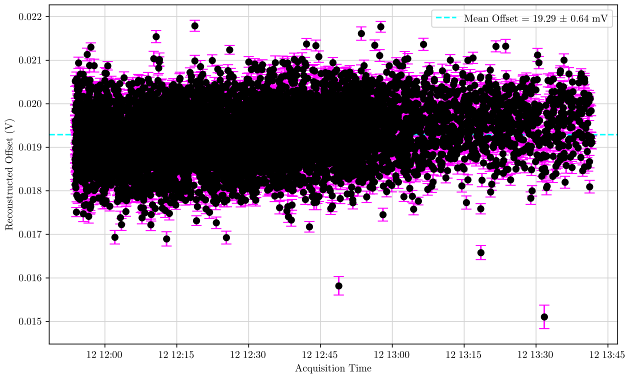

Figure A.15: Offset development over time for the measurement with reactor operated at 0.1 kW for 60 min.

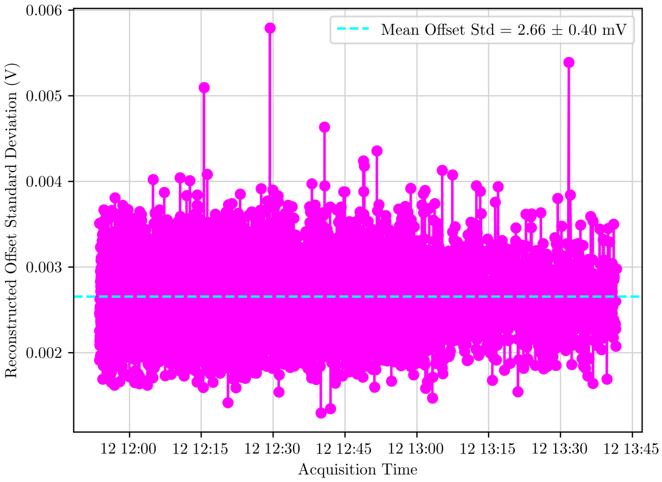

Figure A.16: Std of offset development over time for the measurement with reactor operated at 0.1 kW for 60 min.

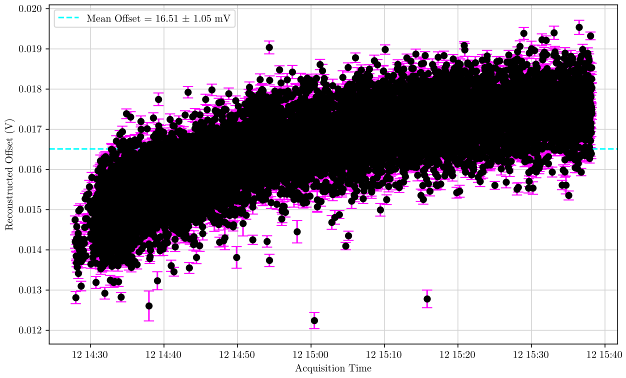

Figure A.17: Offset development over time for the measurement with reactor operated at 1 kW for 60 min.

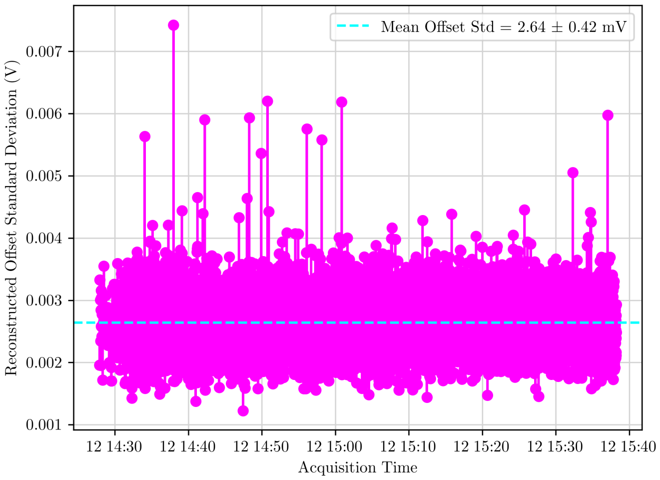

Figure A.18: Std of offset development over time for the measurement with reactor operated at 1 kW for 60 min.

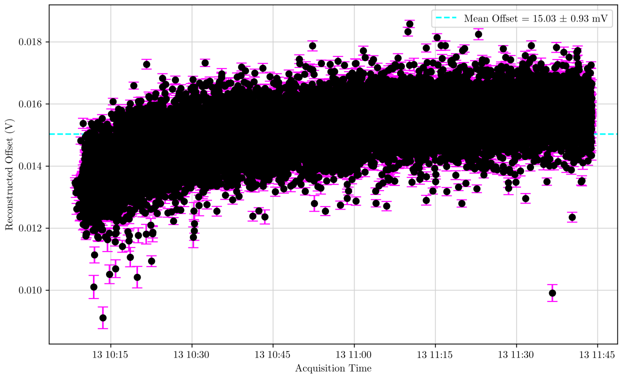

Figure A.19: Offset development over time for the measurement with reactor operated at 10 kW for 24 min.

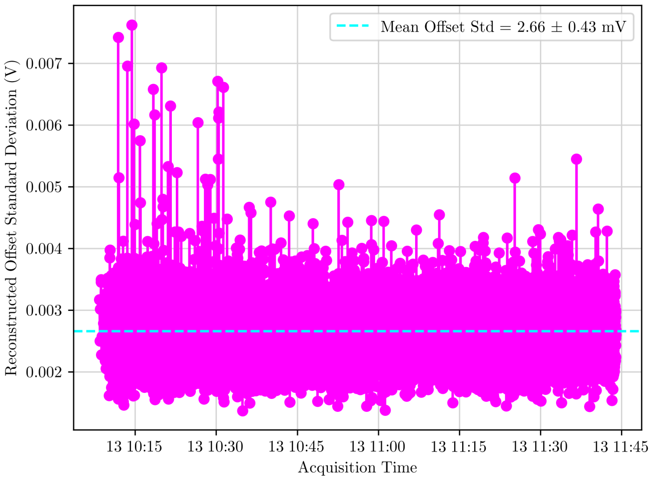

Figure A.20: Std of offset development over time for the measurement with reactor operated at 10 kW for 24 min.

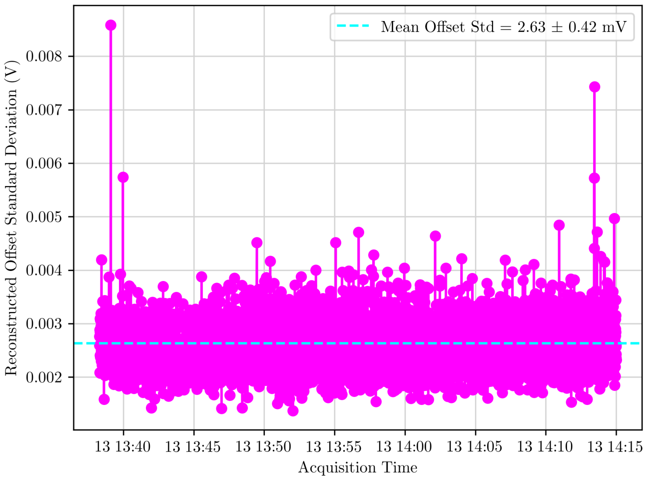

Figure A.21: Std of offset development over time for the measurement with reactor pulse.

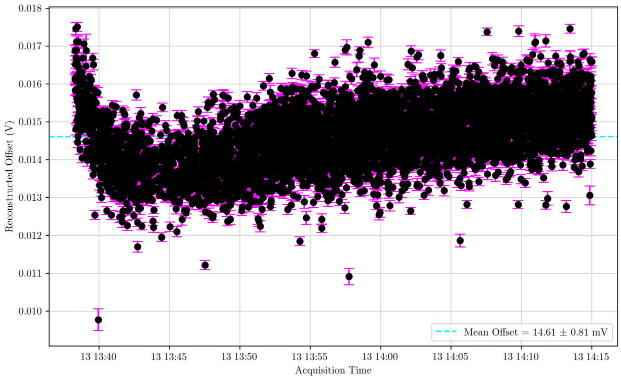

Figure A.22: Offset development over time for the measurement with reactor pulse.

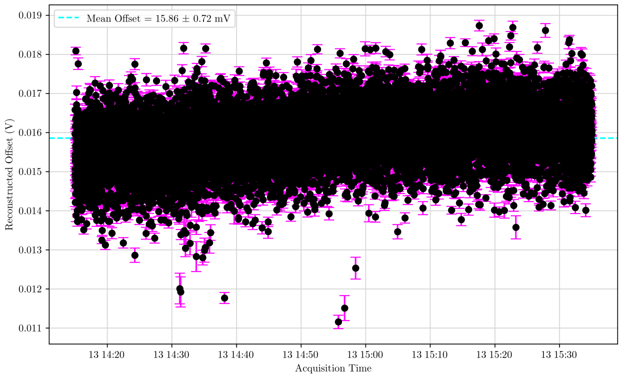

Figure A.23: Offset development over time for the measurement with reactor operated at 100 kW for 4 min.

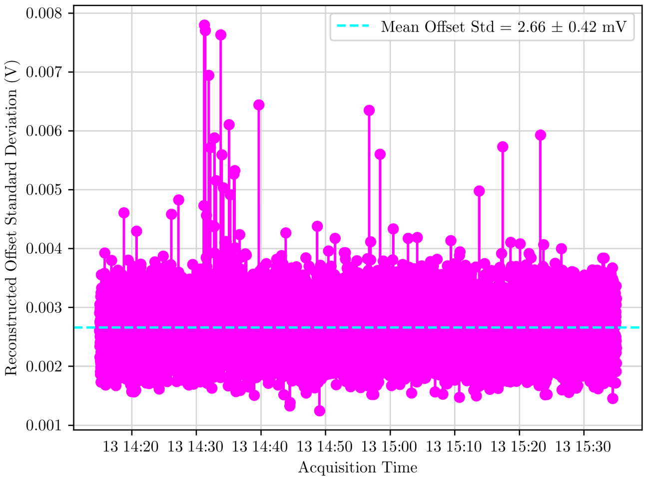

Figure A.24: Std of offset development over time for the measurement with reactor operated at 100 kW for 4 min.

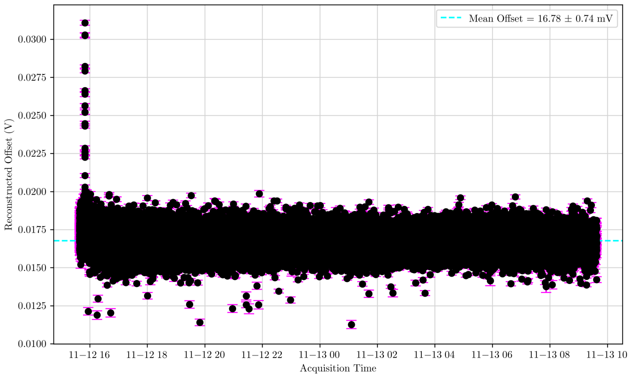

Figure A.25: Offset development over time for ramp down after day 1

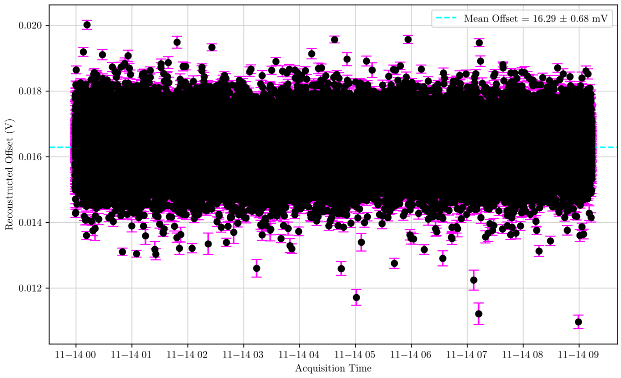

Figure A.26: Offset development over time for ramp down after day 2

Bibliography

1. ASTM Internationals, *Standard Test Methods for In-Place Density and Water Content of Soil and Soil-Aggregate by Nuclear Methods (Shallow Depth)* (2025; https://doi.org/10.1520/D6938-23).
2. R. A. Haelg, U. Schneider, *British Journal of Radiology* **93**, 20190412, ISSN: 0007-1285 (Jan. 2020).
3. D. Shea, D. Morgan, *Congressional Research Service*, R41419 (Jan. 2011).
4. R. Kouzes (May 2009).
5. Consuelo Guardiola Salmerón, Dissertation, Department of Physics Universitad Autónoma de Barcelona, 2012.
6. S. Mehendale *et al.*, *Nuclear Instruments and Methods in Physics Research Section A: Accelerators, Spectrometers, Detectors and Associated Equipment* **972**, 164124, ISSN: 0168-9002 (2020).
7. Nayak, A. and Parida, M.K. and Kumar, V. and Prasanna, G., *Journal of Instrumentation* **17**, P07012 (July 2022).
8. A. Tingsuwatit *et al.*, *Applied Physics Letters* **120**, 232103, ISSN: 0003-6951, eprint: https://pubs.aip.org/aip/apl/article-pdf/doi/10.1063/5.0093591/16447462/232103_1_online.pdf (June 2022).
9. F. Bergmeier, M. Volnhals, M. Wielunski, W. Rühm, *Radiation Protection Dosimetry* **161**, 126–129, ISSN: 0144-8420 (Dec. 2013).
10. A. Calamida *et al.*, *The European Physical Journal Plus* **138** (May 2023).
11. P. D. Group, *Neutron mean life* (2024; https://pdglive.lbl.gov/DataBlock.action?node=S017T).
12. International Commission on Radiation Units And Measurements - ICRU, *ICRU Report 63, Nuclear Data for Neutron and Proton Radiotherapy and for Radiation Protection* (2025; https://www.icru.org/report/nuclear-data-for-neutron-and-proton-radiotherapy-and-for-radiation-protection-report-63/).
13. H. Paganetti, *Proton Therapy Physics, First Edition* (CRC Press LLC, 2011), ISBN: 9781439836453.
14. S. Trinkl *et al.*, *Medical Physics* **44**, 1912–1920 (2017).
15. T. E. of Encyclopaedia, *Encyclopedia Britannica - compound-nucleus model* (2025; https://www.britannica.com/science/compound-nucleus-model).
16. In, *The Spallation Process* (John Wiley and Sons, Ltd, 2009), chap. 1, pp. 3–57.

17. P. D. Group, *Proton mass* (2024; `https://pdg.lbl.gov/2018/listings/rpp2018-list-p.pdf`).
18. F. Mezei, in *Neutrons in Soft Matter* (John Wiley and Sons, Ltd, 2011), chap. I.1, pp. 1–28.
19. A. Doumas, G. Smith, *Nuclear Instruments and Methods in Physics Research Section A: Accelerators, Spectrometers, Detectors and Associated Equipment* **675**, 8–14, ISSN: 0168-9002, (`https://www.sciencedirect.com/science/article/pii/S0168900212000757`) (2012).
20. F. Pino *et al.*, *Scientific Reports* **13**, 4799, ISSN: 2045-2322, (`https://doi.org/10.1038/s41598-023-31675-9`) (Mar. 2023).
21. I. C. Zada, A. Osovizky, I. Orion, *Scientific Reports* **14**, 31446, ISSN: 2045-2322, (`https://doi.org/10.1038/s41598-024-83129-5`) (Dec. 2024).
22. S. D. PINTO, *Modern Physics Letters A* **28**, 1340025, (`https://doi.org/10.1142/S0217732313400257`) (2013).
23. G. F. Knoll, *Radiation detection and measurement; 4th ed.* (Wiley, New York, NY, 2010).
24. International Commission on Radiological Protection - ICRP (2024; `https://www.icrp.org/publication.asp?id=ICRP%20Publication%20103`).
25. R. L. Bramblett, R. I. Ewing, T. Bonner, *Nuclear Instruments and Methods* **9**, 1–12 (1960).
26. Physikalisch Technische Bundesanstalt - PTB, *Neutron Multisphere Spectrometer* (2025; `https://www.ptb.de/cms/ptb/fachabteilungen/abt6/fb-64/643-neutronenspektrometrie/nemus/neutronen-spektrometer-nemus-neutron-multisphere-spectrometer.html`).
27. S. Rivera Vázquez, R. Méndez Villafañe, X. Campo Blanco, F. G. Sánchez, *Radiation Physics and Chemistry* **224**, 112081, ISSN: 0969-806X (2024).
28. A. Esposito, M. Nandy, *Radiation Protection Dosimetry* **110**, 555–558, ISSN: 0144-8420, eprint: `https://academic.oup.com/rpd/article-pdf/110/1-4/555/4531427/nch385.pdf` (Aug. 2004).
29. M. Reginatto, P. Goldhagen, S. Neumann, *Nuclear Instruments and Methods in Physics Research Section A: Accelerators, Spectrometers, Detectors and Associated Equipment* **476**, Int. Workshop on Neutron Field Spectrometry in Science, Technolog y and Radiation Protection, 242–246, ISSN: 0168-9002 (2002).
30. *MPA-Albedo GD02*, Materialprüfungsamt (MPA) NRW.
31. S. Mayer, M-A. Chevallier, E. Fantuzzi, M. Hajek, M. Luszik-Bhadra, R. Tanner, D.J. Thomas, F. Vanhavere, *EURADOS Intercomparison IC2017n for Neutron Dosemeters* (2024; `https://eurados.sckcen.be/sites/eurados/files/uploads/Report-Publications/Reports/2021/EURADOS%20Report%202021-06.pdf`).

32. E. Yukihara *et al.*, *Journal of Luminescence* **183**, 525–532, ISSN: 0022-2313 (2017).
33. *Personendosimeter MPA TL-DOS GD 01*, Materialprüfungsamt (MPA) NRW.
34. K. Inozemtsev *et al.*, *Radiation Measurements* **140**, 106505, ISSN: 1350-4487 (2021).
35. M. Bolzonella *et al.*, *Physics Open* **12**, 100114, ISSN: 2666-0326 (2022).
36. L. Hager, R. Tanner, P. Gilvin, J. Eakins, S. Baker, *Radiation Measurements* **106**, Proceedings of the 18th International Conference on Solid State Dosimetry (SSD18), Munich, Germany, 3 – 8 July 2016, 303–311, ISSN: 1350-4487 (2017).
37. J. Gómez-Ros, R. Bedogni, C. Domingo, *Radiation Measurements* **161**, 106908, ISSN: 1350-4487 (2023).
38. Isotopes Tracers Project, *Resources on Isotopes* (2025; https://wwwrcamnl.wr.usgs.gov/isoig/period/si_iig.html#:~:text=Silicon%20has%20nine%20isotopes%2C%20with%20mass%20numbers%20from%2025%2D33.&text=Si%20(the%20most%20abundant%20isotope,isotope%20produced%20by%20argon%20decay.).
39. Nuclear Data Section, IAEA, *Experimental Nuclear Reaction Data (EXFOR)* (2025; https://www-nds.iaea.org/exfor/).
40. NIST, *Neutron scattering lengths and cross sections* (2025; https://www.ncnr.nist.gov/resources/n-lengths/elements/b.html).
41. International Atomic Energy Agency - IAEA, *Fusion Evaluated Nuclear Data Library (FENDL)* (2025; https://www-nds.iaea.org/fendl/).
42. G. Nowak *et al.*, *Journal of Applied Physics* **117**, 034901 (2015).
43. Alina Landmann, MSc, TU Dortmund Univeristy Faculty of Physics, 2021.
44. S. Agostinelli *et al.*, *Nuclear Instruments and Methods in Physics Research Section A: Accelerators, Spectrometers, Detectors and Associated Equipment* **506**, 250–303, ISSN: 0168-9002 (2003).
45. Ruben D. Trimpop, BSc, TU Dortmund Univeristy Faculty of Physics, 2022.
46. Julissa Green (Stanford Advanced Materials), *An Overview of Magnetron Sputtering* (2025; https://www.sputtertargets.net/blog/an-overview-of-magnetron-sputtering.html).
47. European Spallation Source - ESS, *European Spallation Source* (2025; https://ess.eu/).
48. H. Kolanoski, N. Wermes, *Teilchendetektoren - Grundlagen und Anwendungen* (Springer-Verlag Berlin Heidelberg, 1st, 2016).
49. CIVIDEC, *Cx SPECTROSCOPIC SHAPING AMPLIFIER* (2025; https://cividec.at/electronics-Cx.html).
50. CIVIDEC, *TCT AMPLIFIER, 10 kHz - 2 GHz, 40 dB* (2025; https://cividec.at/electronics-C2-TCT.html).
51. Tobias Bisanz, Ingrid-Maria Gregor, Fabian Hügging, Jens Weingarten, *Elektronik im Physikstudium* (Springer Spektrum Berlin, Heidelberg, 2024).

52. L. Diehl *et al.*, *Nuclear Instruments and Methods in Physics Research Section A: Accelerators, Spectrometers, Detectors and Associated Equipment* **1033**, 166671, ISSN: 0168-9002 (2022).
53. M. Baselga *et al.*, *Journal of Instrumentation* **20**, C01027 (Jan. 2025).
54. Gorshkov, G. V., Gretchenko, Z. G., Il'inskaya, T. A., Kuznetsov, B. S., Shimanskaya, N. S., *The Soviet Journal of Atomic Energy* **7**, 912–920, ISSN: 1573-8205 (Mar. 1961).
55. TEKTRONIX, *5 Series B MSO Mixed Signal Oscilloscope* (2025; https://www.tek.com/en/products/oscilloscopes/5-series-mso).
56. *Python* (2024; https://docs.scipy.org/doc/scipy/reference/generated/scipy.signal.find_peaks.html).
57. NIST, *Stopping Power and Range Tables for Helium Ions* (2025; https://physics.nist.gov/PhysRefData/Star/Text/ASTAR-t.html).
58. General Atomics, *TRIGA Nuclear Reactors* (2025; https://www.ga.com/triga/).
59. Nuclear Power, *Uranium 235 Fission* (2025; https://www.nuclear-power.com/nuclear-power-plant/nuclear-fuel/uranium/uranium-235/uranium-235-fission/).
60. Brookhaven National Laboratory, *Evaluated Nuclear Data File (ENDF)* (2025; https://www.nndc.bnl.gov/endf/).
61. Johannes Gutenberg Universität Mainz, *Forschungsreaktor TRIGA Mainz* (2025; https://www.triga.uni-mainz.de/informationen/).
62. *Python* (2024; https://www.python.org/).
63. *Python* (2024; https://docs.scipy.org/doc/scipy/tutorial/fft.html).
64. Bundesamt für Strahlenschutz, *GSM standard* (2025; https://www.bfs.de/EN/topics/emf/mobile-communication/basics/gsm/gsm_node.html#:~:text=These%20networks%2C%20which%20are%20still,900%20MHz%20and%201800%20MHz.).
65. L. D. Landau, *J. Phys. (USSR)* **8**, 201–205 (1944).
66. J. Moyal, *The London, Edinburgh, and Dublin Philosophical Magazine and Journal of Science* **46**, 263–280 (1955).

Danke!

Ich hoffe, dass sich alle, denen ich ich mich von ganzem Herzen zu Dank verpflichtet fühle, dessen bewusst sind und sie sollen sich an dieser Stelle ehrlich wertgeschätzt fühlen. Einen Namen möchte ich jedoch gerne als erstes nennen:

Danke Jens!

Ich danke selbstverständlich Herrn Prof. Dr. Kevin Kröninger dafür, dass ich seit meiner Bachelorarbeit Teil Ihrer Arbeitsgruppe war und schlussendlich diese Arbeit bei Ihnen schreiben durfte. Auch möchte ich mich gerne bei Prof. Dr. Armin Lühr, für das Erstellen des Zweitgutachtens für diese Arbeit bedanken.

Für das Probelesen, eure aufmunternden Worte, Anfeuerungen und eure Unterstützung möchte ich gerne Marta, Mike, Andrea (die erste), Anja und auch Andrea Knue danken. Zumindest ich freue mich, dass ich ab jetzt wieder mehr Zeit für das ein oder andere Pläuschchen haben werde. Looking at you, Mike!